Spectroscopy and External Control of Optical Dynamics in Single Semiconductor Nanocrystals

by

Kentaro Shimizu

B.Sc. Mathematics/Chemistry
University of British Columbia, Vancouver, Canada, 1997

Submitted to the Department of Chemistry
in partial fulfillment of the requirements for the degree of

DOCTOR OF PHILOSOPHY

at the

MASSACHUSETTS INSTITUTE OF TECHNOLOGY

September 2002

Signature of Author _____
Department of Chemistry
August 7, 2002

Certified by _____
Moungi G. Bawendi
Professor of Chemistry
Thesis Supervisor

Accepted by _____
Robert W. Field
Professor of Chemistry
Chairman, Departmental Committee on Graduate Students

This doctoral thesis has been examined by a committee of the Department of Chemistry as follows:

Professor Robert W. Field _____
Chairman

Professor Moungi G. Bawendi _____
Thesis Supervisor

Professor Jianshu Cao _____

Spectroscopy and External Control of
Optical Dynamics in Single Semiconductor Nanocrystals

by

Kentaro Shimizu

Submitted to the Department of Chemistry on August 7, 2002, in partial fulfillment
of the requirements for the degree of Doctor of Philosophy in Chemistry

Abstract

Single molecule spectroscopy has progressed substantially in the past ten years and the accompanying progress in the optical study of single semiconductor nanocrystals has opened a new dimension in our understanding of the photophysical properties of these quantum-confined materials. In this thesis, I describe experimental advances that investigate and manipulate optical dynamics – *blinking* and *spectral diffusion* – in single CdSe and CdTe nanocrystals caused by complex interactions of electric fields and charge migration between a nanocrystal and its nearby environment. With the aid of a simple yet powerful fluorescence far-field microscope, we examine the blinking phenomenon using statistical analysis to determine a temperature-independent physical mechanism (charge tunneling) that is universal to every nanocrystal. Furthermore, we uncover a strong correlation between the blinking and spectral diffusion processes. This correlation proves to be critical in connecting the power-law statistics observed from blinking in isolated nanocrystals with the binary spectral shifts in surface plasmon coupled nanocrystals. Moreover, we identify charged nanocrystal emission signatures and create charged nanocrystals on command. This level of control, whether to turn the nanocrystals off or to eliminate the blinking behavior, also improves the prospects for nanocrystal device applications. Finally, we explore the impact of external magnetic fields on single nanocrystal optical properties and reveal behavior that is dependent on nanocrystal orientations relative to the applied field. In addition, we observe evidence of zero-field splitting in a subset of nanocrystals. This corroborates theoretical models that propose paramagnetic interactions as an explanation for the fundamental physics of CdSe nanocrystal emission.

Thesis Supervisor: Moungi G. Bawendi, Ph. D.
Title: Professor of Chemistry

For my family and friends

Table of Contents

Title Page 1
Signature Page 3
Abstract 5
Dedication 7
Table of Contents 9
List of Figures 11

Chapter 1: Introduction
1.1 Motivation 13
1.2 Quantum Dots 14
1.3 Single Molecule Spectroscopy 19
1.4 Thesis Overview 24
1.5 References 25

Chapter 2: Single Nanocrystal Blinking
2.1 Introduction 29
2.2 Experimental 30
2.3 Results 32
2.3.1 Off-time Results 34
2.3.2 On-time Results 38
2.4 Discussion 43
2.4.1 Charged Dots Are Dark 43
2.4.2 Random Walk, First Passage Return Time 45
2.4.3 Other Models 48
2.4.4 Intensity Saturation 49
2.5 Conclusion 50
2.6 References 51

Chapter 3: Spectral Diffusion and Blinking
3.1 Introduction 53
3.2 Experimental 54
3.3 Results 54
3.4 Discussion 59
3.4.1 The Statistics 59
3.4.2 The Model 62
3.4.3 DC Stark Spectroscopy 66
3.5 Conclusion 68
3.6 References 68

Chapter 4: Surface Enhanced Fluorescence
4.1 Introduction 71
4.2 Experimental 72
4.3 Results 74
4.3.1 Power-Law Spectral Jumps 74

4.3.2 Emission Polarization 76
4.3.3 Excited State Lifetimes 78
4.3.4 Hot Band Emission 78
4.4 Discussion 81
4.4.1 Charged Exciton Emission 81
4.4.2 The Electromagnetic Model 82
4.4.3 Beating the Auger Rate 84
4.5 Conclusion 85
4.6 Acknowledgements 85
4.7 References 85

Chapter 5: Charging Nanocrystal Quantum Dots
5.1 Introduction 87
5.2 Experimental 88
5.3 Results and Discussion 90
5.3.1 Fluorescence Quenching 90
5.3.2 Charge Injection 92
5.3.3 ZnS Overcoated NCs 93
5.3.4 Positive Bias 95
5.3.5 Device Stability 95
5.3.6 Polymer vs. ZnS Insulating Layer 98
5.3.7 Absorption Changes 99
5.4 Future Studies 101
5.5 Conclusion 102
5.6 References 102

Chapter 6: Single Nanocrystal Zeeman Spectroscopy
6.1 Introduction 105
6.2 Experimental 106
6.3 Results 108
6.4 Discussion 117
6.4.1 The Exciton Fine Structure 117
6.4.2 Molecular Zeeman Effect 119
6.4.3 Correlation between Orientation and Magnetic Field 120
6.4.4 Zero-Field Splitting 121
6.5 Conclusion and Future Studies 122
6.6 References 123

List of Publications 125
Acknowledgements 127

List of Figures

Fig. 1.1	Cartoon and TEM images of CdSe NCs	16
Fig. 1.2	Absorption and emission spectra for various NC sizes	18
Fig. 1.3	Diagram and photo of single molecule far-field microscope	22
Fig. 2.1	Data cube of single NC fluorescence images	31
Fig. 2.2	Intensity time traces at RT and 10 K	33
Fig. 2.3	*Off*-time probability distribution at RT	35
Fig. 2.4	Time trace and blinking statistics for CdTe NCs	36
Fig. 2.5a	Temperature-dependent *off*-time probability distribution	37
Fig. 2.5b	Size and surface composition dependent *off*-time statistics	39
Fig. 2.6	*On*-time probability distribution	40
Fig. 2.7	Average emission intensity vs. *on*-time saturation	42
Fig. 2.8	Physical model of the blinking dynamics	44
Fig. 2.9	Random-walk simulation of blinking behavior	46
Fig. 3.1	Single NC image and corresponding emission spectrum	55
Fig. 3.2	Spectral time traces at 10 K and RT	56
Fig. 3.3	Observation of blink-and-shift correlated behavior at 10 K	58
Fig. 3.4	Distribution of net spectral shifts for *on* and *off* durations	60
Fig. 3.5	Possible changes of the electric field environment around a NC	63
Fig. 3.6	Stark spectra of single NCs	65
Fig. 3.7	Electric field effects on spectral diffusion	67
Fig. 4.1	AFM image of the roughened gold substrate	73
Fig. 4.2	Surface-enhanced fluorescence behavior	75
Fig. 4.3	Polarization data for surface plasmon coupled NCs	77
Fig. 4.4	Time-resolved measurements for NCs on gold substrate	79
Fig. 4.5	Hot-band emission in CdSe NCs	80
Fig. 5.1	NC Capacitor charging device structure	89
Fig. 5.2	Charging and fluorescence quenching of bare NCs	91
Fig. 5.3	Charging and fluorescence quenching of overcoated NCs	94
Fig. 5.4	Hole injection into bare NCs	96
Fig. 5.5	Device stability and rapid response	97
Fig. 5.6	Absorption changes for charged NCs	100
Fig. 6.1	Magnetic field experimental layout	107
Fig. 6.2	Polarization-resolved images in the presence of a magnetic field	110
Fig. 6.3	Magnetic field dependent polarization time trace	111
Fig. 6.4	NC orientation vs. polarization changes due to Zeeman splitting	113
Fig. 6.5	Singe NC spectra with Zeeman spectral splitting at 10 T	115
Fig. 6.6	Polarization-resolved spectra showing zero-field splitting	116
Fig. 6.7	Energy level diagram for the band-edge states	118

Chapter 1 Introduction

1.1 Motivation

Continuing research and development of well-controlled nanometer sized macromolecules promise unprecedented chemical control over optical, electrical, and thermal properties of inorganic semiconductor[1-4], metallic[5, 6] and organic solids[7, 8]. With physical properties no longer determined solely by their atomic numbers, the physics of semiconductor nanomaterials depends on their potential energy boundary conditions and the effective masses of the exciton that leads to quantization of electronic energy levels. This control is expected to bring advances in various applications including biological fluorescence and absorbance tagging[9, 10], low-threshold, tunable solid-state lasers[11], light guiding photonic bandgap crystals[12], photovoltaic devices, and cheap and compact imaging displays[13, 14]. However, in order to reach these goals and to discover additional possibilities, a better understanding of the nanomaterial physical properties is necessary.

The work in this thesis describes stepwise efforts to comprehend the full complexity of single II-VI semiconductor (CdSe and CdTe) nanocrystal (NC) quantum dots* interacting with their immediate electrostatic and magnetic environment. The first sign of intricate mechanisms underlying the light emitted from CdSe nanocrystals was revealed in NC photobleaching in CdSe-doped glasses[15]. This has progressed to the observation of binary fluorescence intensity fluctuations[16] and recently to measurements of ultra-fast population inversion (bi-exciton) lifetimes, limiting nanocrystal lasing[17, 18]. Presently, theory suggests that Auger relaxation processes, a

* The terms nanocrystal, nanoparticle, and (colloidal) quantum dot (QD) are synonyms in this field. However, self-assembled QDs also known as Stranski-Krastanow QDs are significantly different from colloidal QDs.

form of exciton-electron (or exciton-hole) energy transfer, dominate in all of the aforementioned semiconductor nanocrystal experimental results and connect results attained in single NC studies to ensemble studies and technological applications.

The discovery of blinking NCs in 1996 marked the beginning of a unique and interesting research topic. Unfortunately, during our pursuits to measure intrinsic NC physical properties such as structural dipole moments, excited state lifetimes, and band gap electron energy levels, the blinking optical behavior always showed a greater impact on the data. Therefore, learning about and altering the behavior of blinking NCs is paramount to all areas of single NC studies.

1.2 Quantum Dots

Quantum confinement of the electron (and hole) in one dimension, taught in freshman quantum chemistry as a particle in a small box, initially explains the quantum size effects in structures ranging from quantum wells (1-D confinement)[19], quantum wires (2-D confinement)[20], and quantum dots (3-D confinement)[21]. Commonly, quantum wells and quantum wires will also emulate a quantum dot when surface defects produce small potential wells to localize the exciton[22]. For a spherical quantum "box", the resulting dispersion curve behaves as follows:

$$E = E_g + \frac{\hbar^2 \alpha^2_{n_e,l_e}}{2m_e a^2} + \frac{\hbar^2 \alpha^2_{n_h,l_h}}{2m_h a^2} \qquad (1)$$

where E_g is the bulk bandgap (CdSe values are 1.74 ~ 1.84 eV for temperatures between

300 K down to 10 K[**]) and m_e and m_h are the effective masses of the electron and hole, respectively, in the semiconductor dielectric. $\hbar$ is Planck's constant divided by 2π, a is the sphere's radius, and α_{n_e,l_e} and α_{n_h,l_h} are the n^{th} zero of the l^{th} order spherical Bessel function for the electron and hole, respectively.

In CdSe NCs, the confining box is nearly spherical with a slightly prolate shape as shown in figure 1.1(a) and 1.1(b). The mesoscale size of this sphere begins with a handful of atoms[23] and extends towards crystals of ~10,000 atoms with sizes approaching the Bohr exciton diameter of 110 Å (a measure of the characteristic length scale). For CdSe nanocrystals, this characteristic length scale is larger than the confining length scale, a. In this strong confinement regime, the exciton energy primarily follows the confinement potential ($\sim \frac{1}{a^2}$) and the coulombic interaction ($\sim \frac{1}{a}$) is treated as a perturbation[24, 25]. In the case of weak confinement, where the exciton-confining box is much larger than the characteristic length scale of the semiconductor material, the coulombic interaction is used in the Hamiltonian leaving the confinement term as a perturbation. Both wet chemical synthesis and molecular beam vapor phase deposition methods can produce various colloidal nanocrystals (CdSe[26], CdTe[27], PbSe[28], PbS[29], InP[30], Au[31], Ag[32], etc) and self-assembled quantum dots (InGaAs\GaAs[33], InGaP\InP[34], CdSe\ZnSe[35], etc), respectively. Indeed, many research groups have succeeded in producing particles with a high level of control over the size, shape, and surface passivation. Furthermore, the use of band-gap engineering by

[**] The bandgap is temperature dependent because the average lattice spacing of the crystal nuclei will become smaller as the temperature decreases and the vibrational energy in the crystal decreases. Accordingly, the energy of the electron in a more closely spaced lattice increases.

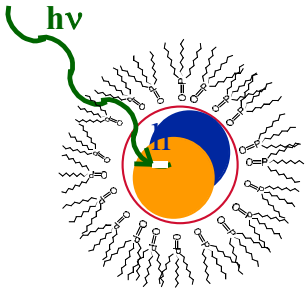

a.

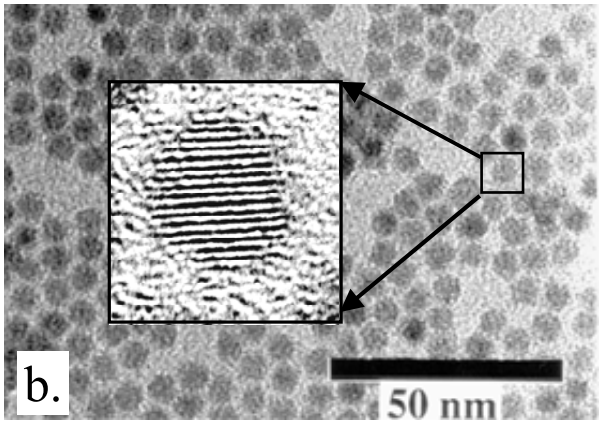

TEM images taken by F.V. Mikulec and C.B. Murray

Figure 1.1: (a) A cartoon drawing of a single CdSe nanocrystal excited by a photon of energy E= hν. The surrounding brush-like structures represent organic ligands such as tri-octylphosphine oxide. (b) A transmission electron microscope image of many NCs. The organic ligands keep the NCs from aggregating and the monodisperse size distribution allows for hexagonal close packing of the NC film. The inset shows a high-resolution image with clear lattice fringes of the single crystalline core.

overcoating the core NCs with a higher band gap semiconductor material[36, 37] has shown improvement in photoluminescence efficiency, stability, and shows longer emissive durations during single NC blinking sequences compared to the native core nanocrystal. In self-assembled quantum dots, the wetting/capping layer is deposited epitaxially to passivate the surface; the rare occurrence of optical dynamics in self-assembled QDs is attributed to the nearly defect free semiconductor passivation[38].

The 3-dimensional confinement for quantum dots leads to comparisons of the electronic levels to atomic energy levels due to the spectrally discrete absorption and emission features shown in figure 1.2(a) and 1.2(b). The question is, "Where do the similarities end and the differences begin in the fundamental physical properties of these NCs?" Various experiments over the last 10 years have shown examples where clear differences exist between the artificial atom picture and the physics of colloidal CdSe NCs. First, the band gap optical transitions are distributed into eight fine structure states, split into five energy levels, that relax to the ground state[39]. Consequently, transitions from the lowest of the band gap states to the ground state are predicted to be optically forbidden (dark exciton state). This is the primary explanation for the surprisingly long excited state lifetimes at cryogenic temperatures (~100 ns to ~μs)[40]. By applying magnetic fields across a film of NCs, the total angular momentum eigenstates of the NCs aligned perpendicular to the field are mixed, resulting in shorter lifetimes[41]. Size selective methods such as fluorescence line narrowing can better resolve spectral features[42]; however, the earlier ensemble experimental data used to form and verify the theoretical models have reached their limits. To further develop these models, we require spectroscopic data from truly homogeneous sizes and crystal orientations to unravel the

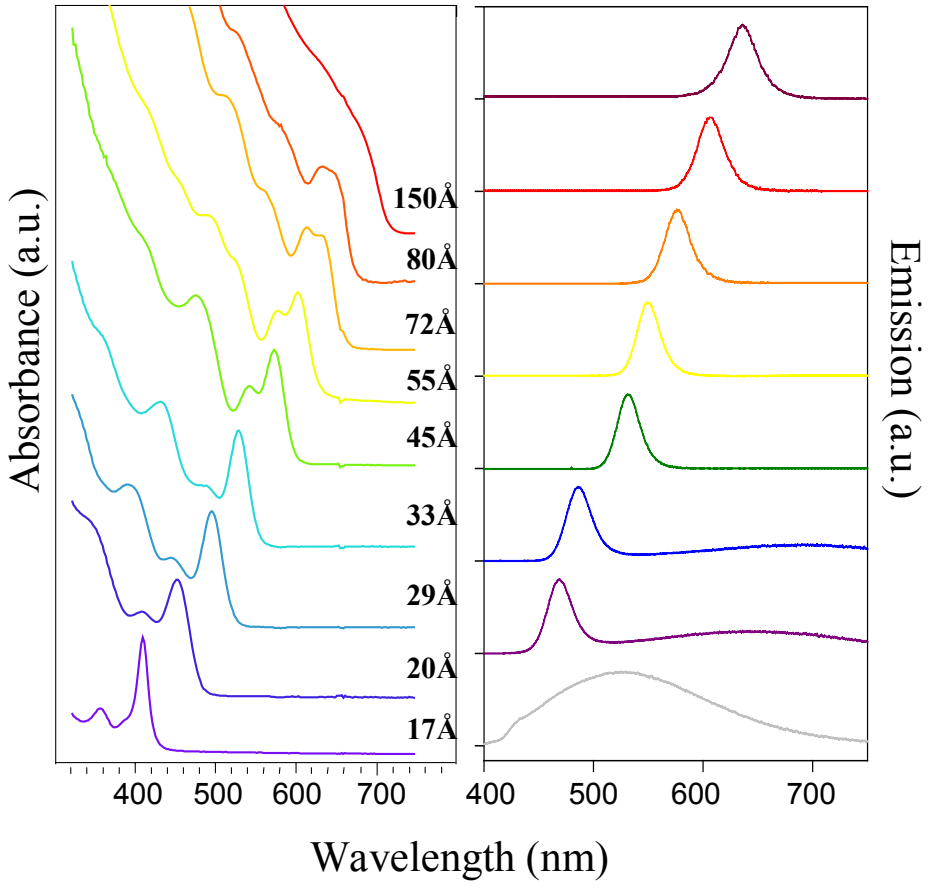

Figure 1.2: (a) Absorption and (b) emission spectra from a size series of CdSe nanocrystals in solution. Typically, the first, second, and third absorption features can be identified for narrow size distributions as shown above. Corresponding fluorescence peak characterized by a Gaussian profile and 25nm full width half maximum.

intrinsic properties of each nanocrystal.

1.3 Single Molecule Microscopy

The history of single molecule optical microscopy is rather short and the road to achieving this high sensitivity has been paved by technological advances in photodiodes and charge-coupled device (CCD) cameras[43, 44]. Twelve years after the first single molecule fluorescence experiments[45], commercial confocal microscopes are now readily available and achieve high signal-to-noise for real-time monitoring of single chromophores in a variety of applications. The original techniques employed attaching samples directly to one end of a fiber optic and immersing the sample in a dewar of liquid helium[46]. Single molecule features observed on the wings of the ensemble were the first indicators of single chromophore optical isolation[47]. Most experiments were conducted at low temperatures since cryogenic temperatures increase the oscillator strength of the molecule[43] or quantum dot and make the analysis of spectral information much cleaner after "freezing" out vibrational and other thermal contributions to the spectra. The highlights of single chromophore research include absorption[48], linear[45] and non-linear photoluminescence[49], photoluminescence excitation[50], excitation[51, 52] and emission polarization[53], and excited state lifetime measurements[54] to analyze the electronic energy landscape. In addition, Stark[55], magneto-optic[56], and surface enhanced Raman spectroscopy[57, 58] showed interesting perturbation effects on the single molecule level. As proof that this field continues to mature, single molecule spectroscopy can now be used as a nanometer probe to examine the molecule's host environment for determining molecular orientations and

3-dimensional matrix conformations[59].

Further variations in the single molecule spectroscopic setup have revealed additional insight into the sample topography using near field scanning microscopy to get both nanometer spatial resolution and single chromophore photon detection[54]. However, these measurements are limited to serial data acquisition, prone to sample perturbation by the near field tip, and are more difficult due to lower light throughput. For samples without the flexibility to change the concentration of chromophores on the substrate, metal masks with ~50 nanometer-sized holes can also yield single QD spectra[60]. This form of near-field microscopy removes the excess chromophores by screening them out of the excitation field.

The optical studies of NCs go hand in hand with single molecule spectroscopy. Regardless of how the quantum dots are fashioned, the inherent distribution in particle size directly impacts the measured NC ensemble electronic structure. Even a difference of a few atoms on the surface of NCs can change the size distribution by 4%[26]. To understand the full potential of nanoparticles and their interaction with the environment, we use the high throughput, non-invasive technique of far-field fluorescence microscopy. By illuminating NCs spatially separated by distances greater than the diffraction limit of light, we can analyze optical data from individual nanoparticles as opposed to the average optical behavior of many particles. This becomes critical not only when the different size of each particle determines the spectral character under study but also when differences in the nanoparticle electric, magnetic, and electromagnetic environment, crystalline orientation and the nanoparticle's dynamic (charged) state affect the optical measurement.

We follow a number of criteria to determine whether we are observing single NCs.

Although one must rely on experience to apply these criteria properly, the following provides evidence that behavior from individual NCs is under study. First, we start with a dilute concentration of the NCs; the nanomolar concentrations should provide approximately 1~2 μm separation between adjacent NCs. Second, the intensity and spectral fluctuations, discussed in detail in chapters II and III, should not be synchronized between different NCs. If two or more NCs were imaged close together, the intensity fluctuations would appear quantized in steps depending on the number of NCs aggregated in the same spot. Also, in spectral measurements, two or more NCs would appear as multiple peaks that "diffuse" incoherently from each other. This spectral signature is clearly pronounced at cryogenic temperatures because the linewidths are much narrower. The spectral features also identify NCs apart from organic dye molecules and other impurity chromophores due to the size-dependent emission energy and phonon-progression features spaced 25 meV apart. Finally, the polarization of the NC emission can help to determine whether single NCs are present. Although there is a small percentage of NC that should have no polarization, most NCs would show either elliptical or linear polarization in the emission. If multiple NCs were imaged in the same diffraction-limited spot, then they would most likely have no polarization assuming that these NCs would have random orientations relative to each other.

The basic configuration of the far field fluorescence microscope is outlined in figure 1.3. Although we have employed variations in the excitation light source, primary light collection objective, sample temperature, electric and magnetic field environment, and in the detector equipment, the overall geometry of the optical layout remains unchanged in all four of our custom optical microscopes. The list of excitation sources

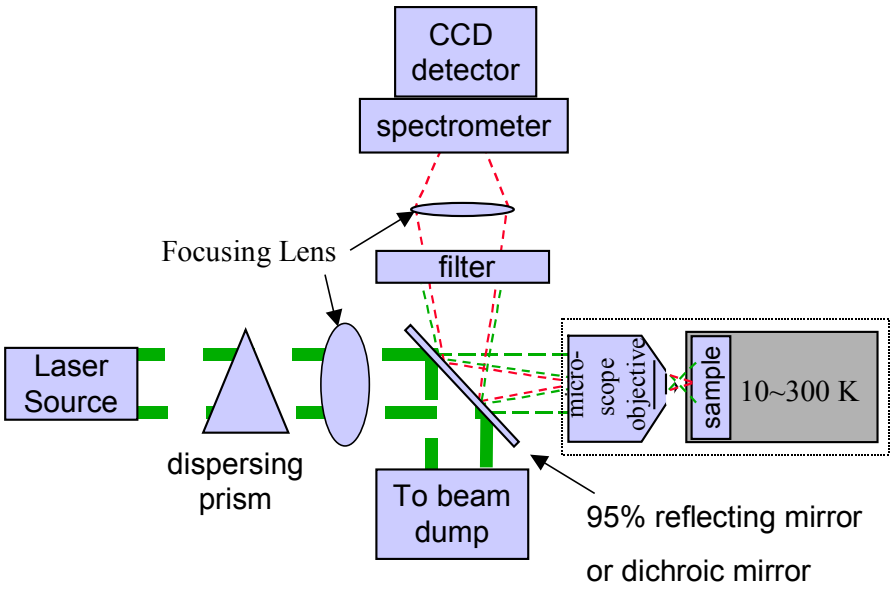

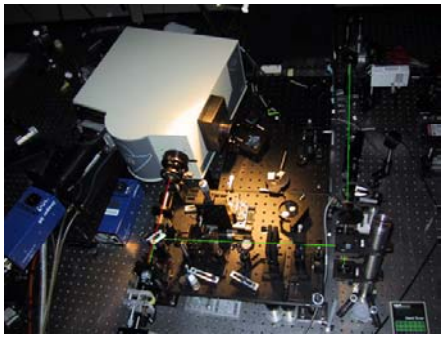

Figure 1.3: Schematic Diagram for an optical far-field fluorescence microscope. The inset shows a physical photo of the ultra-fast optical microscope. The dispersing prism removes any stray lines of the laser. The laser is then focused into the microscope objective such that the laser spot is defocused onto the sample plane. Emission is collected through the same objective and reflected into the spectrometer. A holographic or band pass filter combination removes the excess laser light. Either a CCD or photodiode detector is used to capture the emitted image or spectrum. The photo below is a working setup for taking time-resolved single NC measurements.

Table 1.1: Comparison of Various Microscope Light Sources and Detection Instrumentation.

Excitation Source	**Detection Source**	**Typical Time Resolution:** Integration time and Readout time	**Advantages**	**Disadvantages**
Ar+ Ion CW laser (514.5nm, 488nm, 457 nm)	PentaMax Intensified CCD	100ms to 1s, within integration time	- Easy to focus images. - Fast and near continuous time resolution.	- Not adept for long integration times. - Maximum frames limited to 320000. - Low threshold for intensifier damage.
	MicroMax Thermal-electrically cooled CCD	500ms to 60s, ~500ms (100x100) to ~2s (1024x1024)	- Robust - Large CCD area. - High quantum efficiency for general-purpose use.	- Slow readout time. - Dark counts limit max integration time to 1 min.
	LN2 cooled CCD	1s to 10min, ~10ms (512x1) to ~500ms (512x512)	- Robust. - Ultra-low dark counts for long exposure measurements.	- Slow readout time. - Outdated software. - Requires liquid nitrogen and 30 min cool down time.
	EG&G Avalanche Photodiode (APD)	~200μs to 10ms	- Single photon counting. - Low dark counts.	- Vulnerable to damage by stray light. - No imaging capability without scanning.
	Human eye	< 60ms	- Auto-focus - Color detection	- Laser damage permanent. - Data storage is limited.
CW Dye laser (530~620nm)	All of the above		Tunable within ~20nm range of dye emission maximum.	- Dye Photostability. - Excitation power not constant throughout wavelength range.
Mira/OPO picosecond (3ps) or femtosecond (100fs) pulsed laser (400~1200nm)	LaVision Picostar Intensified, Gated CCD	200ps to 5ns at rep. rates of 76 Mhz to 1Mhz	- Ultrafast resolved images.	- Limited to 200ps. - Gated data acquisition results in long sample illumination during entire scan.
	APD	30~200ps	- Time correlated single photon counting (with counting electronics)	- No imaging
400 nm diode laser	All of the above	~ns	- Turn key operation. - Portable.	- Limited to 400nm wavelength. - Maximum power is 5mw.

and detectors are listed in table 1.1 with a comparison of their advantages and disadvantages. All experiments dealing with low temperature or temperature dependence were conducted using a high numerical aperture (N.A. = 0.7, 60X) air objective, while room temperature investigations used liquid immersion objectives (N.A. = 1.25, 100X) that achieve numerical apertures greater than 1 by refracting a greater amount of light into the objective collection angle.

1.4 Thesis Overview

In this thesis, I describe a number of experiments that showcase the involved interactions of electric fields and charge migration between the nanoparticle core and its nearby environment. The simple far field microscope is incorporated in different aspects to retrieve the relevant information and reveal the wide applicability of laser-induced fluorescence microscopy. Chapter II deals with the primary issue of blinking as a starting point for investigating single nanocrystal emission dynamics. Chapter III takes advantage of rich spectral data that can be simultaneously taken to understand the correlation between blinking and spectral diffusion. Chapters IV and V take the next steps in harnessing the possible technology presented by nanometer-sized blinking particles. In particular, chapter IV explains how blinking can be removed or drastically reduced by coupling of the nanocrystal to electromagnetic fields through surface plasmon resonance from nearby metallic surfaces. In chapter V, we apply the charged NC model to develop a working device that makes NCs blink in unison. This fluorescence quenching is controlled by charge injection into the NC core. Finally, chapter VI touches on the impact of applied magnetic fields on single NC optical properties. By examining

individual NCs, behavior that is dependent not only on optical orientations, but also properties specific to a subset of NCs can be uncovered. In particular, evidence for zero-field splitting in NCs is observed, corroborating suggestions of a magnetic impurity in a subset of NCs to explain the fluorescence lifetime behavior.

1.5 References

1. C.B. Murray, C.R. Kagan, and M.G. Bawendi, Annual Review of Materials Science, 2000. **30**: p. 545.
2. A.P. Alivisatos, Science, 1996. **271**(5251): p. 933.
3. A.J. Nozik, Annual Review of Physical Chemistry, 2001. **52**: p. 193.
4. A.D. Yoffe, Advances in Physics, 2001. **50**(1): p. 1.
5. G. Markovich, C.P. Collier, S.E. Henrichs, F. Remacle, R.D. Levine, and J.R. Heath, Accounts of Chemical Research, 1999. **32**(5): p. 415.
6. M.D. Musick, C.D. Keating, L.A. Lyon, S.L. Botsko, D.J. Pena, W.D. Holliway, T.M. McEvoy, J.N. Richardson, and M.J. Natan, Chemistry of Materials, 2000. **12**(10): p. 2869.
7. H.J. Dai, Surface Science, 2002. **500**(1-3): p. 218.
8. E.T. Thostenson, Z.F. Ren, and T.W. Chou, Composites Science and Technology, 2001. **61**(13): p. 1899.
9. M. Bruchez, M. Moronne, P. Gin, S. Weiss, and A.P. Alivisatos, Science, 1998. **281**(5385): p. 2013.
10. H. Mattoussi, J.M. Mauro, E.R. Goldman, G.P. Anderson, V.C. Sundar, F.V. Mikulec, and M.G. Bawendi, Journal of the American Chemical Society, 2000. **122**(49): p. 12142.
11. M. Grundmann, Physica E, 1999. **5**(3): p. 167.
12. Y.A. Vlasov, X.Z. Bo, J.C. Sturm, and D.J. Norris, Nature, 2001. **414**(6861): p. 289.
13. P. Gomez-Romero, Advanced Materials, 2001. **13**(3): p. 163.
14. K. Rajeshwar, N.R. de Tacconi, and C.R. Chenthamarakshan, Chemistry of Materials, 2001. **13**(9): p. 2765.
15. A.I. Ekimov, I.A. Kudryavtsev, M.G. Ivanov, and A.L. Efros, Journal of Luminescence, 1990. **46**(2): p. 83.
16. M. Nirmal, B.O. Dabbousi, M.G. Bawendi, J.J. Macklin, J.K. Trautman, T.D. Harris, and L.E. Brus, Nature, 1996. **383**(6603): p. 802.
17. V.I. Klimov, A.A. Mikhailovsky, S. Xu, A. Malko, J.A. Hollingsworth, C.A. Leatherdale, H.J. Eisler, and M.G. Bawendi, Science, 2000. **290**(5490): p. 314.
18. V.I. Klimov, A.A. Mikhailovsky, D.W. McBranch, C.A. Leatherdale, and M.G. Bawendi, Science, 2000. **287**(5455): p. 1011.
19. S. Schmittrink, D.S. Chemla, and D.A.B. Miller, Advances in Physics, 1989. **38**(2): p. 89.

20. J.T. Hu, T.W. Odom, and C.M. Lieber, Accounts of Chemical Research, 1999. **32**(5): p. 435.
21. L.E. Brus, Journal of Chemical Physics, 1984. **80**(9): p. 4403.
22. N.H. Bonadeo, J. Erland, D. Gammon, D. Park, D.S. Katzer, and D.G. Steel, Science, 1998. **282**(5393): p. 1473.
23. N.V. Soloviev, A. Eichhofer, D. Fenske, and U. Banin, Journal of the American Chemical Society, 2001. **123**(10): p. 2354.
24. L. Brus, Applied Physics a-Materials Science & Processing, 1991. **53**(6): p. 465.
25. A.L. Efros, Soviet Physics Semiconductors-Ussr, 1982. **16**(7): p. 772.
26. C.B. Murray, D.J. Norris, and M.G. Bawendi, Journal of the American Chemical Society, 1993. **115**(19): p. 8706.
27. M.Y. Gao, S. Kirstein, H. Mohwald, A.L. Rogach, A. Kornowski, A. Eychmuller, and H. Weller, Journal of Physical Chemistry B, 1998. **102**(43): p. 8360.
28. C.B. Murray, S.H. Sun, W. Gaschler, H. Doyle, T.A. Betley, and C.R. Kagan, Ibm Journal of Research and Development, 2001. **45**(1): p. 47.
29. T.D. Krauss, F.W. Wise, and D.B. Tanner, Physical Review Letters, 1996. **76**(8): p. 1376.
30. A.A. Guzelian, J.E.B. Katari, A.V. Kadavanich, U. Banin, K. Hamad, A.P. Alivisatos, R.H. Walters, H.S. Chung, and J.R. Heath, Abstracts of Papers of the American Chemical Society, 1995. **210**: p. 707.
31. R.L. Whetten, J.T. Khoury, M.M. Alvarez, S. Murthy, I. Vezmar, Z.L. Wang, P.W. Stephens, C.L. Cleveland, W.D. Luedtke, and U. Landman, Advanced Materials, 1996. **8**(5): p. 428.
32. G. Markovich, C.P. Collier, and J.R. Heath, Physical Review Letters, 1998. **80**(17): p. 3807.
33. G. Wang, S. Fafard, D. Leonard, J.E. Bowers, J.L. Merz, and P.M. Petroff, Applied Physics Letters, 1994. **64**(21): p. 2815.
34. N. Carlsson, W. Seifert, A. Petersson, P. Castrillo, M.E. Pistol, and L. Samuelson, Applied Physics Letters, 1994. **65**(24): p. 3093.
35. S.H. Xin, P.D. Wang, A. Yin, C. Kim, M. Dobrowolska, J.L. Merz, and J.K. Furdyna, Applied Physics Letters, 1996. **69**(25): p. 3884.
36. M.A. Hines and P. Guyot-Sionnest, Journal of Physical Chemistry, 1996. **100**(2): p. 468.
37. B.O. Dabbousi, J. RodriguezViejo, F.V. Mikulec, J.R. Heine, H. Mattoussi, R. Ober, K.F. Jensen, and M.G. Bawendi, Journal of Physical Chemistry B, 1997. **101**(46): p. 9463.
38. M. Sugisaki, H.W. Ren, K. Nishi, and Y. Masumoto, Physical Review Letters, 2001. **86**(21): p. 4883.
39. A.L. Efros, M. Rosen, M. Kuno, M. Nirmal, D.J. Norris, and M. Bawendi, Physical Review B-Condensed Matter, 1996. **54**(7): p. 4843.
40. M.G. Bawendi, P.J. Carroll, W.L. Wilson, and L.E. Brus, Journal of Chemical Physics, 1992. **96**(2): p. 946.
41. M. Nirmal, D.J. Norris, M. Kuno, M.G. Bawendi, A.L. Efros, and M. Rosen, Physical Review Letters, 1995. **75**(20): p. 3728.
42. M. Nirmal, C.B. Murray, and M.G. Bawendi, Physical Review B-Condensed Matter, 1994. **50**(4): p. 2293.

43. T. Plakhotnik, E.A. Donley, and U.P. Wild, Annual Review of Physical Chemistry, 1997. **48**: p. 181.
44. P. Tamarat, A. Maali, B. Lounis, and M. Orrit, Journal of Physical Chemistry A, 2000. **104**(1): p. 1.
45. M. Orrit and J. Bernard, Journal of Luminescence, 1992. **53**(1-6): p. 165.
46. M. Orrit and J. Bernard, Physical Review Letters, 1990. **65**(21): p. 2716.
47. W.E. Moerner, Science, 1994. **265**(5168): p. 46.
48. W.E. Moerner and L. Kador, Physical Review Letters, 1989. **62**(21): p. 2535.
49. J. Mertz, C. Xu, and W.W. Webb, Optics Letters, 1995. **20**(24): p. 2532.
50. W.P. Ambrose, T. Basche, and W.E. Moerner, Journal of Chemical Physics, 1991. **95**(10): p. 7150.
51. E. Betzig, Science, 1994. **263**(5144): p. 159.
52. T. Ha, T. Enderle, D.S. Chemla, P.R. Selvin, and S. Weiss, Physical Review Letters, 1996. **77**(19): p. 3979.
53. A.P. Bartko and R.M. Dickson, Journal of Physical Chemistry B, 1999. **103**(51): p. 11237.
54. X.S. Xie, Accounts of Chemical Research, 1996. **29**(12): p. 598.
55. U.P. Wild, F. Guttler, M. Pirotta, and A. Renn, Chemical Physics Letters, 1992. **193**(6): p. 451.
56. J. Kohler, J. Disselhorst, M. Donckers, E.J.J. Groenen, J. Schmidt, and W.E. Moerner, Nature, 1993. **363**(6426): p. 242.
57. K. Kneipp, Y. Wang, H. Kneipp, L.T. Perelman, I. Itzkan, R. Dasari, and M.S. Feld, Physical Review Letters, 1997. **78**(9): p. 1667.
58. A.M. Michaels, M. Nirmal, and L.E. Brus, Journal of the American Chemical Society, 1999. **121**(43): p. 9932.
59. A.P. Bartko, K.W. Xu, and R.M. Dickson, Physical Review Letters, 2002. **89**(2): p. art. 026101.
60. T. Kummell, R. Weigand, G. Bacher, A. Forchel, K. Leonardi, D. Hommel, and H. Selke, Applied Physics Letters, 1998. **73**(21): p. 3105.

Chapter 2. Single Nanocrystal Blinking [*]

2.1 Introduction

Analyzing the light-matter interactions in a vial filled with billions of NCs, one would never imagine that every single NC was turning *on* and *off* independent from each other. As the solute concentration is decreased to its final dilution of one chromophore, such dynamic and intricate information about its unique environment and quantum state is revealed. This fluorescence intermittency or blinking has become a signature of single chromophore studies due to the ubiquitous and almost self-serving nature of this phenomenon. The list includes conjugated polymers[1], Green Fluorescent Proteins (GFP) [2], organic dye molecules, silicon nanoparticles [3], SERS of single dye molecules [4], CdSe and InP self-assembled quantum dots[5], and CdSe, CdTe, InP[6] colloidal nanocrystals and this list continues to grow. By definition, fluorescence intermittency or blinking refers to binary intensity fluctuations (*on* and *off*) that occur as a function of time (on the order of μs to minutes and longer) under continuous wave (CW) light excitation. This differs from the Poisson statistics for single photon arrival times. As such, the minimum duration of the integration time needs to be sufficient to acquire a steady flux of photons for the NC excitation-relaxation cycle. Hence, the blinking-*off* refers to the extended interruption of photon flux for this minimum duration or longer. Although the blinking behavior is observed under similar conditions, the blinking statistics are distinct for different chromophores. Accordingly, the explicit mechanism that controls the blinking kinetics differs. For example, blinking in single dye molecules follows an exponential distribution of *on* and *off*-times – the time duration of each

[*] Much of this chapter has appeared in print (K. T. Shimizu *et al.* Phys. Rev. B. **63**, art. 205316, 2001)

emissive or non-emissive sequence. This indicates transitions between the singlet (bright) and triplet (dark) state[7]. The statistical distribution of *on* and *off* times is then dictated by the forward, k_f, and backward, k_b, transition rate. In GFP, two protein confirmations exist that absorb and emit at different wavelengths where first order rate kinetics between the two confirmations governs the switch from one confirmation to the other[2]. In the case of semiconductor nanocrystals, recent room temperature (RT) studies [8] show a power-law histogram of the *off*-times indicative of a distribution in kinetic rates between the bright and dark NC state(s). In this chapter, we examine the CdSe blinking behavior for various physical parameters – temperature, intensity, and surface passivation – in the context of power-law statistics.

2.2 Experimental

We study over 200 individual NCs simultaneously using a home-built, epi-fluorescence microscope apparatus. Under photo-excitation of the 457 nm or the 514 nm line of an Ar ion laser, the emission intensity fluctuations are measured with a time resolution of 100 ms for durations of an hour. Single dot fluorescence was acquired through an oil immersion lens for room temperature studies while temperature dependent studies were performed in a liquid helium cold finger cryostat adapted to an x-z translation stage. All single NC samples are highly diluted (500X dilution from a 0.1 absorbance solution) and spin-cast in a 0.2~0.5 micron thin film of low molecular weight polymethylmethacrylate (PMMA) matrix. A Roper Scientific Pentamax intensified CCD detector was used to collect data from *all* of the dots that emit light during the observation period to ensure a complete statistical treatment of blinking. The raw data,

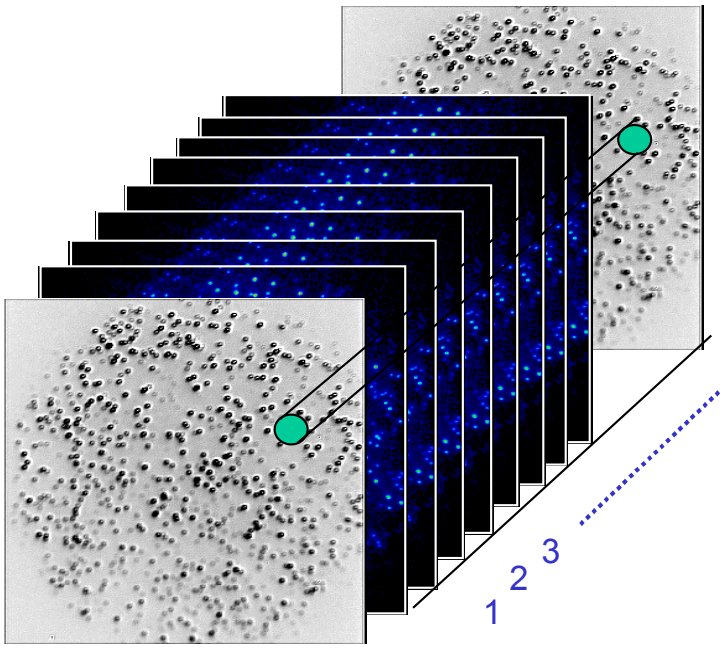

Figure 2.1: Data cube of *x*-axis–*y*-axis–*t*ime dimensions. Each dark spot represents emission from a single nanocrystal. Each frame consists of a 100 ms time-integrated image with roughly 200 NCs in view. Movies with 30000 frames are collected typically with 100x100 pixel area producing a 650 MB data file.

shown in figure 2.1, consists of consecutive images that form nearly continuous[**] 3-dimensional (*x-y-time*) data sets. The dark spots represent emission from individual NCs spaced approximately 1~2 μm apart. This highly parallel form of data acquisition is vital for a proper statistical sampling of the entire population. The raw image files were processed through Visual Basic macros to facilitate quantitative analysis of each data set.

2.3 Results

An illustrative 3000 s time-trace of fluorescence intermittency is shown for a CdSe/ZnS NC at RT and at 10 K in figure 2.2(a) and 2.2(b), respectively. A small section of the time trace is expanded to show the self-similarity and complexity of the traces on different time scales. We define the *on* time (or *off* time) as the interval of time when no signal falls below (or surpasses) a chosen threshold intensity value as labeled in figure 2.2(c). The probability distribution is given by the histogram of *on* or *off* events:

$$P(t) = \sum \text{ [events of length } t\text{]} \qquad (1)$$

where t refers to the duration of the blink *off* or blink *on* event. The choice of threshold can make a large difference in the resulting probability distribution. Ideally, the time trace is taken with sufficient signal and time resolution to attain binary blinking behavior. As a counter example, RT data taken with high excitation intensity (1 kW/cm^2) with 100 ms integration times often led to "grass-like" traces even for overcoated samples. These results should be analyzed with the caveat that events shorter than the integration time now dominate the observed time trace. In all of the experiments described below, the

[**] The intensified CCD camera can integrate the signal on the multiple channel plate (intensifier) while the charges are read out from the CCD silicon chip. The dead time between consecutive scans is negligible as long as the integration time is slightly longer than the readout time.

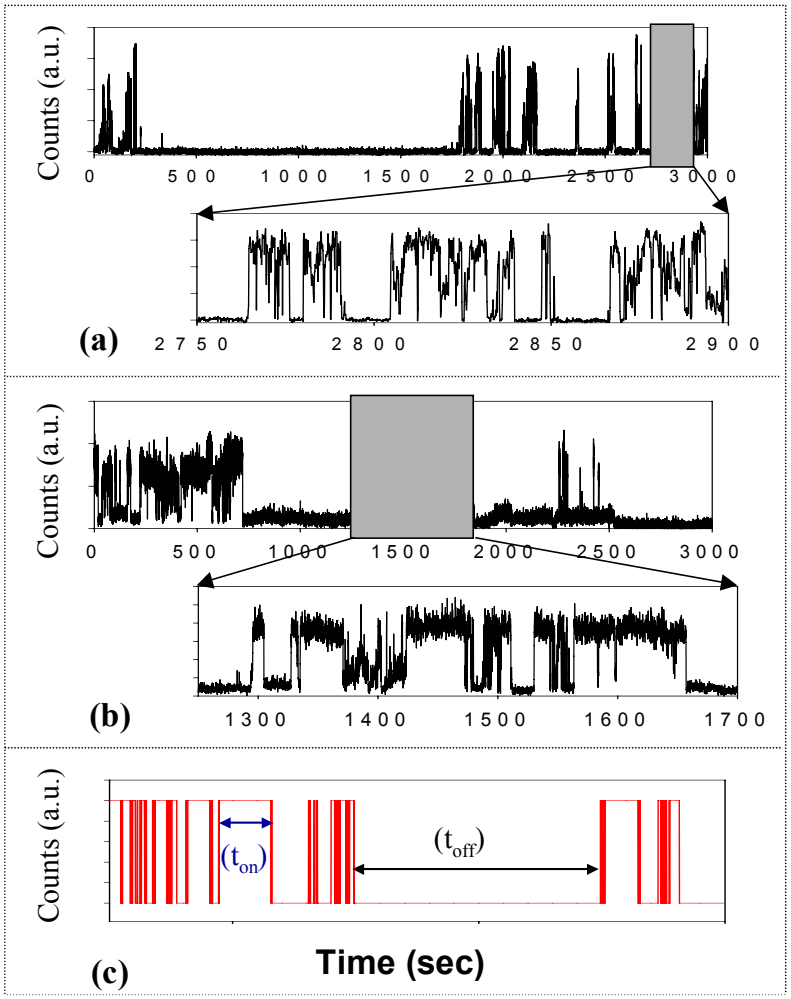

Figure 2.2: Typical intensity time trace of CdSe/ZnS NC fluorescence intermittency at (a) Room Temperature and (b) 10 K. Expanded view illustrates the similar nature of the blinking behavior at RT and 10 K but with different time scales. Data taken with 100 ms time resolution. (c) Theoretical time-trace describing t_{on} and t_{off} as it pertains to the statistical treatment of the blinking kinetics.

threshold was chosen as twice the root mean square value of the baseline intensity, when the NC was deemed *off*.

2.3.1 *Off*-time Results

The *off*-time probability distribution for a single CdSe/ZnS NC at room temperature is shown in figure 2.3(a). The distribution follows a pure power law for the time regime of our experiments (~10^3 s):

$$P(t) = A\,t^{-\alpha} \qquad (2)$$

Moreover, most individual NCs also follow a power-law probability distribution with the same value in the power-law exponents ($\alpha \approx 1.5 \pm 0.1$). A histogram of α values for individual NCs is shown in figure 2.3(b). The universality of this statistical behavior indicates that the blinking statistics for the *off*-times are insensitive to the different environments of each NC. Kuno *et al.*[8] first observed this behavior at room temperature using conventional confocal microscopy. Due to higher signal-to-noise, confocal microscopy provides time resolution as high as 200 μs; however, the same probability distribution is also observed with 100 ms integration times. Initial experiments at RT (figure 2.4) show that the same blinking statistics are also observed in CdTe NCs demonstrating that this power-law phenomenon is not restricted to CdSe NCs.

To develop a physical model from this phenomenological power-law behavior, we probe the temperature dependence of the blinking statistics; this dependence should provide insight into the type and the energy scales of the blinking mechanism (tunneling vs. hopping). Qualitatively, the data in figure 2.2(a) and 2.2(b) suggests that at low temperature the NCs blink less and stay in the *on* state for a larger portion of the time

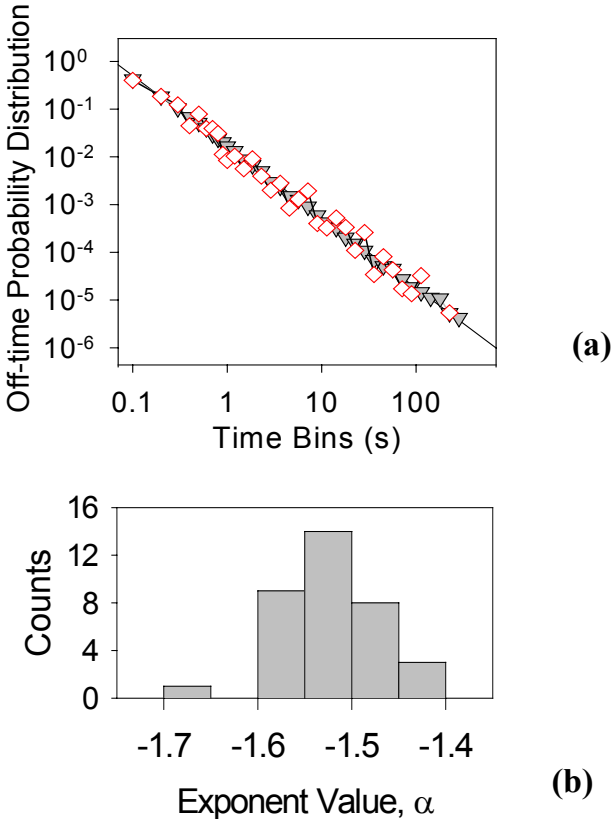

Figure 2.3:(a) Normalized *off*-time probability distribution for one CdSe NC (open diamond) and average of 39 CdSe NCs (filled triangle). Straight line is a best fit to the the average distribution with exponent ~ –1.5. (b) Histogram of fitting values for the power-law exponent in the 39 CdSe NCs.

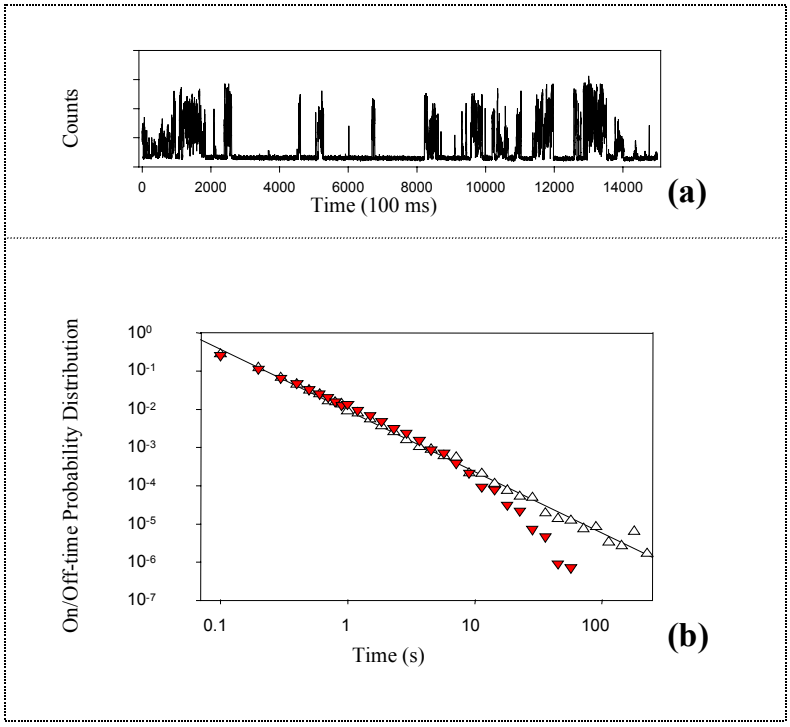

Figure 2.4: (a) Time trace of a single CdTe NC at room temperature with 125 W/cm^2 excitation power. (b) Normalized probability distribution of the *on*-time(filled triangle) and *off*-time (empty triangle) for CdTe NCs at RT plotted on a log-log scale. The best-fit line shows a power-law behavior with exponent ~ – 1.6. The CdTe NCs were packaged in a TiO_2 matrix to prevent premature oxidation and photobleaching.

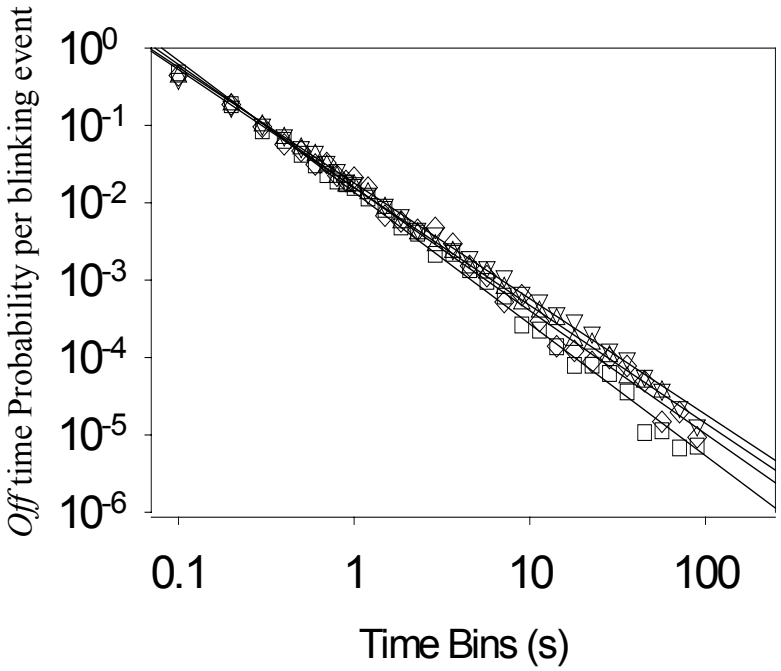

Figure 2.5(a): Average *off*-time probability distribution for 25 Å radius CdSe(ZnS) NC at 300 K (▽), 10 K (△), 30 K (◇), and 70 K (□). The α values are 1.41, 1.51, 1.37, and 1.45, respectively.

observed. However, when we plot the *off*-time probability distributions at temperatures ranging from 10 K to 300 K, as shown in figure. 2.5(a), the statistics still show power-law behavior regardless of temperature. Moreover, the average exponents in the power law distributions are statistically identical for different temperatures (10 K: -1.51 ± 0.1, 30 K: -1.37 ± 0.1, 70 K: -1.45 ± 0.1, RT: -1.41 ± 0.1). Such a seemingly contradictory conclusion is, however, resolved by plotting the *on*-time probability distribution at 10 K and RT as shown in figure 2.6. Unlike the *off*-time distribution, the *on*-times have a temperature dependence that is then reflected in the raw data of figure 2.2.

Previous studies have shown intensity independent *off*-time behavior [9, 10]. Intensity independent *off*-time statistics are also observed here. Varying the CW average excitation power in the range of 100W/cm^2 to 3 kW/cm^2 at 300 K and 10 K showed power-law, *off*-time probability distributions with no changes in the exponent value. We also compared the *off*-time statistics for NCs differing in size (15 Å vs. 25 Å core radius) and NCs with and without a 6 monolayer shell of ZnS overcoating shown in figure 2.5(b). Again, the results showed no difference in the statistical nature of the blinking-*on* process.

2.3.2 *On*-time Results

The *on*-time statistics yield a power law distribution with the same exponent [11] as for the *off*-times, but with a temperature dependent "saturation effect" that alters the long time tail of the distribution. This saturation reflects a secondary mechanism that limits the maximum *on*-time of the NC. The saturation effect can be seen in the *on*-time distribution of a single NC in figure 2.6(a) and 2.6(b) as a "truncation", and in the average distribution of many single NCs (figure 2.6 (c) and (d)) as a downward deviation

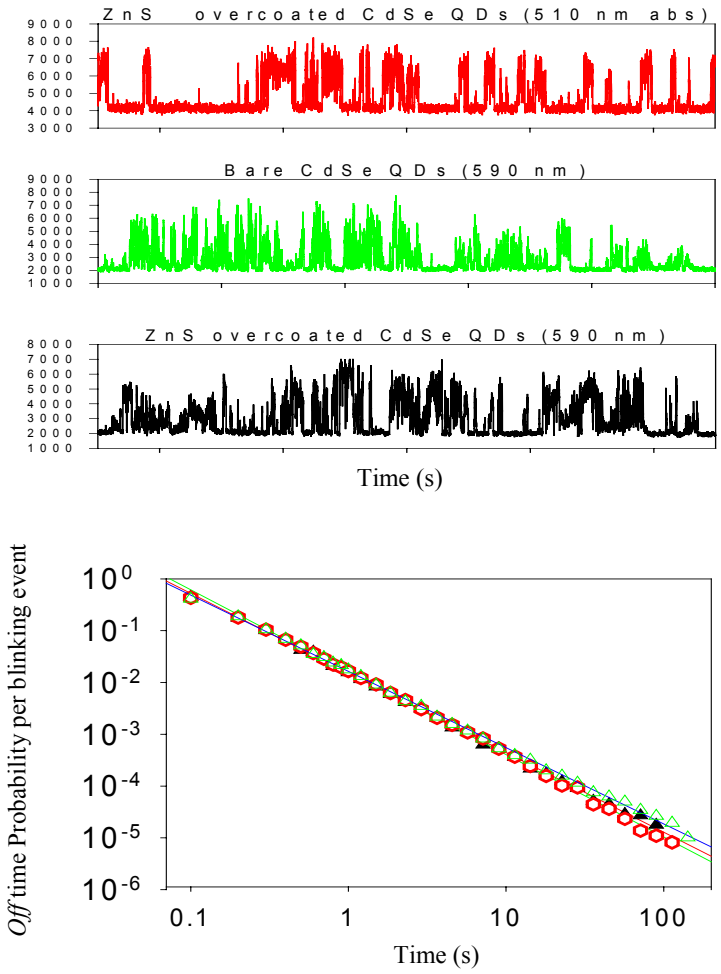

Figure 2.5(b): Intensity time traces from CdSe/ZnS NCs of radius 15 Å (red) and 25 Å radius (black) and 25 Å radius CdSe bare NCs (green). Below are the average *off*-time probability distributions for 39 NCs with corresponding NC size and surface overcoating. The exponent values are –1.54, –1.59 and –1.47, respectively.

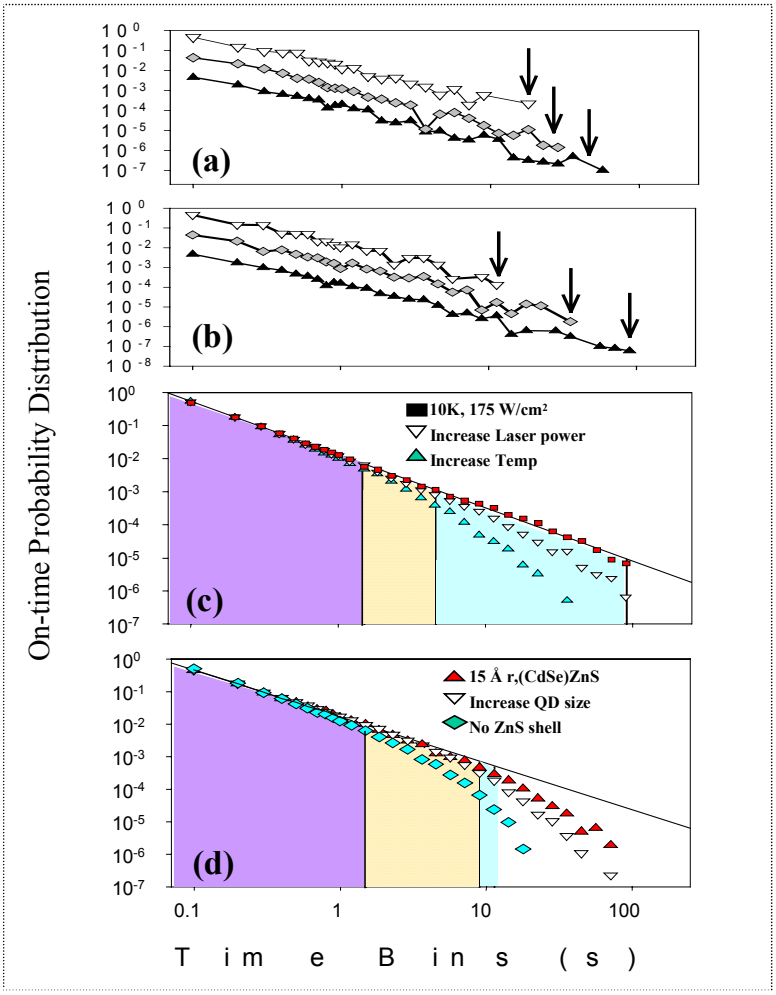

Figure 2.6: (a) Three single NC on time probability distributions at 10K, 700 W/cm^2. The arrows indicate the truncation point for the probability distribution for each NC. (b) Three single NC *on*-time probability distributions for CdSe(ZnS) NCs at RT, 100 W/cm^2. (c) Average *on*-time probability distribution for 25 Å radius CdSe(ZnS) NC at 300 K and 175 W/cm^2 (▲), 10 K and 700 W/cm^2 (▽), and 10 K and 175 W/cm^2 (■). The straight line is a best-fit line with exponent ~ –1.6. (d) Average *on*-time probability distribution for 15 Å radius CdSe(ZnS) NC (▲) and 25 Å radius CdSe(ZnS) NC (▽) and 25 Å radius CdSe NC (◆) at RT, 100 W/cm^2. The straight line here is a guide for the eye. The vertical lines correspond to truncation points where the power law behavior is estimated to end.

from the pure power law [12]. At low temperatures, the saturation effect sets in at longer times and the resulting time trace shows 'long' *on*-times. The extension of the power law behavior for low temperatures on this logarithmic time scale drastically changes the time trace as seen in Fig. 2.2; i.e. fewer *on-off* events are observed and the *on*-times are longer.

Given that the exponent for the *on*-time power law distribution is nearly the same for all of our samples, then a measure of the average truncation point (or maximum *on*-time) is possible by comparing 'average *on*-times' for different samples while keeping the same overall experimental time. We calculate average *on* time of 312 ms, 283 ms, and 256 ms for the same CdSe/ZnS sample under 10 K and 175 W/cm^2, 10 K and 700 W/cm^2, and RT and 175 W/cm^2 excitation intensity, respectively. The effective truncation times (1.5 s, 4.6 s, and 71 s, respectively) can be extrapolated by determining the end point within the power-law distribution that corresponds to the measured average *on*-time. In figure 2.6(c) and (d), the vertical lines correspond to this calculated average truncation point indicating the crossover in time domain from one blinking mechanism to the other.

Furthermore, we can understand the consequence of this secondary mechanism in terms of single NC quantum efficiency. For ensemble systems, quantum efficiency is defined as the rate of photons emitted versus the photons absorbed. Figure 2.7(a) shows the changes to the single NC time trace with increasing excitation intensity: the intensity values at peak heights increase linearly with excitation power, but the frequency of the *on-off* transitions also increases. Moreover, the measured time-averaged single NC emission photon flux at different excitation intensities, marked by empty triangles in figure 2.7(b), clearly shows a saturation effect. We suggest that this saturation behavior

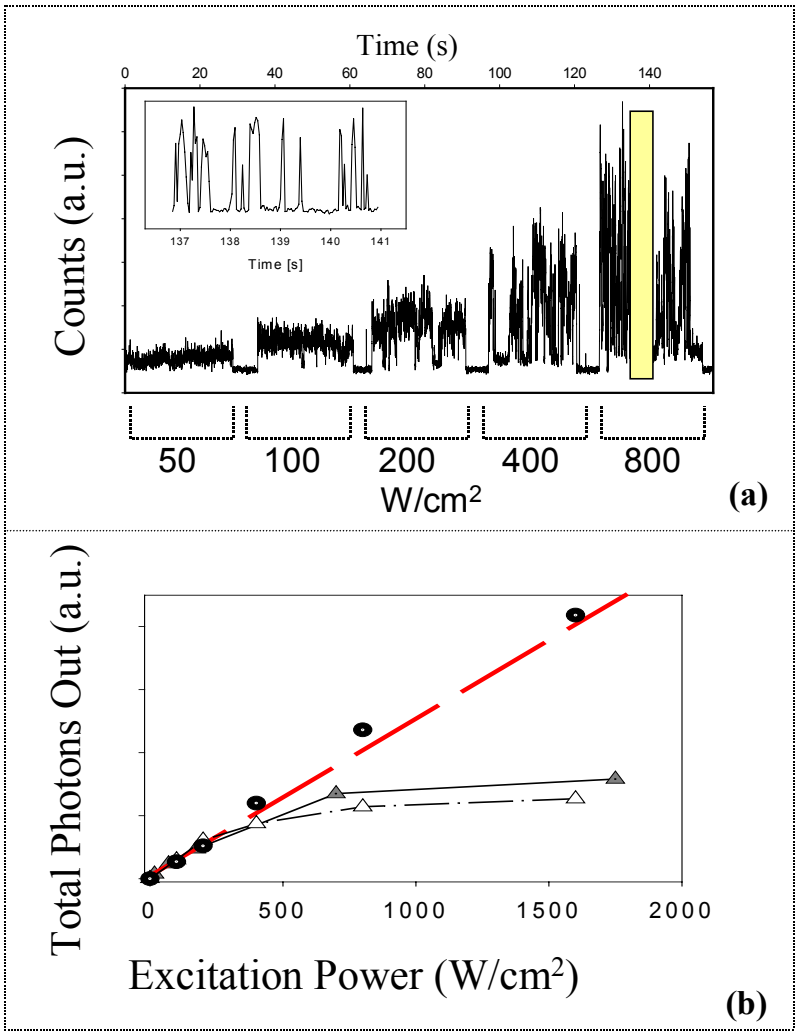

Figure 2.7(a): Time trace of a CdSe(ZnS) NC with increasing excitation intensity in 30 second stages. Inset shows the on-off nature still holds at high excitation intensity. (b): The photon flux at the peak emission intensity (●) and average emission intensity (△) from the time-trace in (a). The average photon flux calculated from an intensity independent power-law distribution of on-times and the intensity dependent truncation values in figure 2.6 are shown by the shaded triangles (▲).

is due to the secondary blinking-*off* process mentioned above. The filled triangles in figure 2.7(b) plot the expected time-averaged emitted photon flux at different excitation intensities calculated from a power-law blinking distribution and truncation values similar to those in figure 2.6. The similarity of the two saturation plots (triangles) in figure 2.7(b) demonstrates the significance of the secondary mechanism to the overall fluorescence of the NC system. The filled circles represent the peak intensity of the single NC at each of the excitation intensities.

Modification of the surface morphology or excitation intensity showed no difference in the statistical nature of the *off*-times or blinking *on* process. The statistical data is consistent with previous work[9, 10]; however, the separation of the power-law statistics from the truncation effects demonstrates that two separate mechanisms govern the blinking of CdSe NCs: (1) a temperature independent tunneling process and (2) a temperature-dependent photo-ionization process. The truncation effect is not observed in the *off*-time statistics on the time scale of our experiments. Since the power law of the *off*-time statistics extends well beyond the truncation point of the power law distribution of the *on*-time statistics, the *on*-time truncation/deviation is not an artifact of the experimental time

2.5 Discussion

2.5.1 Charged Dots Are Dark

The initial model for CdSe NC fluorescence intermittency [9, 13] correlated a theoretical model for photodarkening observed in CdSe doped glasses [14] with the blinking phenomenon under the high excitation intensity used for single NC spectroscopy.

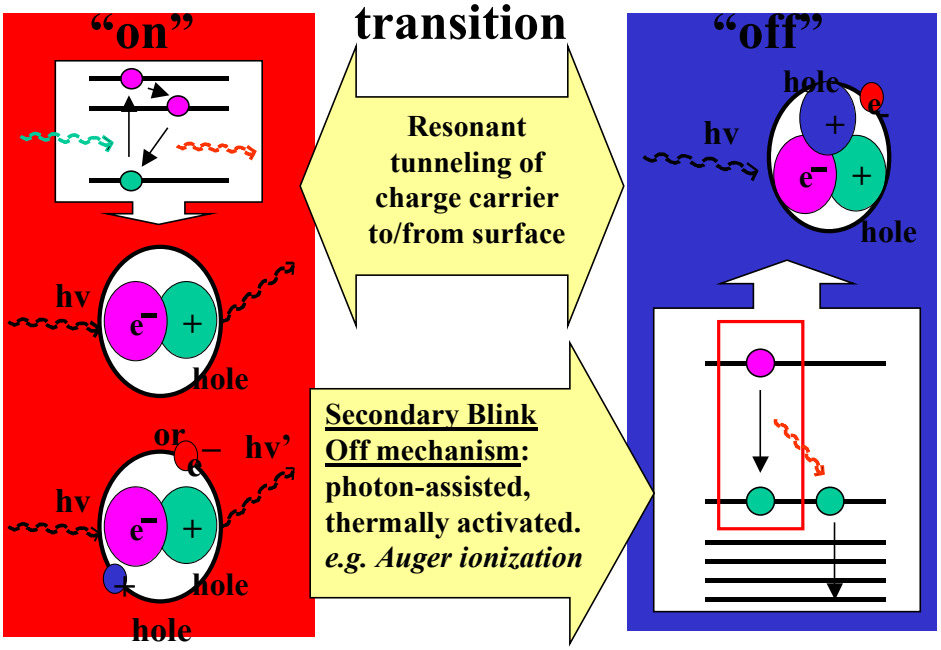

Figure 2.8: Cartoon drawing of the physical mechanism distinguishing a bright NC from a dark NC. (a) An emitting NC is either neutral or net neutral such that the exciton recombines with quantum efficiency, q, to emit the photon with the size-dependent energy, hν. (b) A charged NC still absorbs a photon but a fast (~ ps) non-radiative relaxation pathway is opened by the close proximity of the third charge. This energy transfer from the exciton to the third charge (not necessarily a hole as drawn here) is referred to as Auger relaxation. The temperature independent power-law behavior in the *off*-time and *on*-time statistics identifies the transition as a charge tunneling mechanism. However, the saturation or limited maximum *on*-time indicates a secondary blink-*off* mechanism that is influenced by laser intensity, temperature and NC surface composition.

In the photodarkening experiments, Chepic *et al.* [15] described a NC with a single delocalized charge carrier (hole or electron) as a dark NC. When a charged NC absorbs a photon and creates an exciton, it becomes a quasi three-particle system. The energy transfer from the exciton to the lone charge carrier and non–radiative Auger relaxation of the charge carrier (~ 100 ps) [16] is predicted to be faster than the radiative recombination rate of the exciton (100 ns ~ 1 μs). Therefore, within this model outlined in figure 2.8, a charged NC is a dark NC. This describes the state of a dark NC, but does not explain the transition mechanism between a dark and bright NC.

The universality of the *off*-time statistics for all the NCs indicates an intrinsic physical parameter driving the power-law blinking behavior. Furthermore, since the power law statistics are temperature and excitation intensity independent, the process that couples the dark to bright states is a tunneling process and not photon-assisted. As expanded on in the next chapter, spectrally resolved emission measurements showed a correlation between blinking and spectral shifting at cryogenic temperatures. Considering the large variations in the transition energy (as large as 60 meV [17]) of the bright state, we propose a theoretical framework using a random walk-first passage time model [18] of a dark trap state that shifts into resonance with the excited state to explain the transition from *on* to *off* and vice versa.

2.5.2 Random Walk, First Passage Return Time

In this random walk model, the "*on-off*" blinking takes place as the electrostatic environment around each individual NC undergoes a random walk oscillation. When the electric field changes, the total energy for a localized charged NC also fluctuates and only

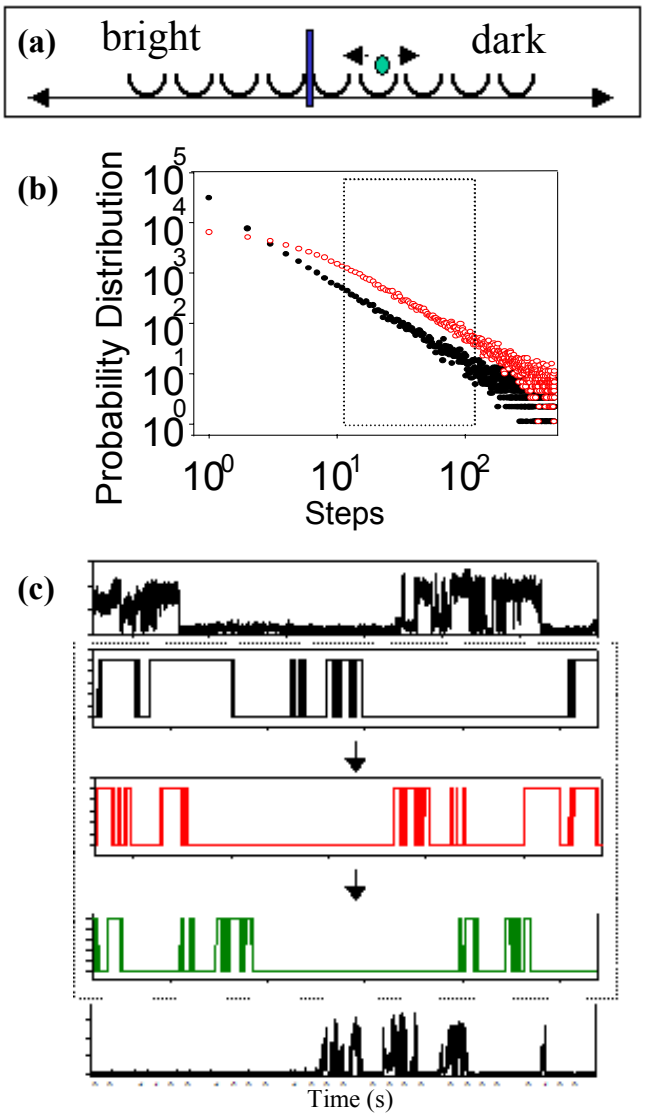

Figure 2.9(a) simple 1-D random walk phase space with a single transition point to go from *on* to *off* or vice versa. (b): Histogram of return times to the origin in a 1-D discrete-step random walk simulation. The boxed region of the histogram represents the accessible time regime (>100ms and <1hr) in relation to our experiments. The filled circles represent room temperature statistics while the unfilled circles represent the low temperature behavior. The change from the RT to the low temperature simulation is modeled by allowing for a probability for the random walker to remain stationary, analogous to insufficient thermal energy at the low temperatures. (c) Simulations of time traces produced from power-law distributions of on and off-times. The maximum *on*-times were decreased to illustrate the changes in the experimental time traces as temperature is increased, excitation intensity is increased, and/or surface passivation is decreased. Top and bottom traces are illustrative experimental traces to show the similarities between the simulation and data.

when the total energy of the localized charge (*off*) state and neutral (*on*) state is in resonance, the change between the two occurs. An analogy can be pictured as a skyscraper with two elevators and a single passenger: Whenever the bright elevator and dark elevator doors open on the same floor, the person can switch from one to the other. Otherwise, the person remains inside the bright (or dark) elevator from floor to floor assuming that the elevator stops at each floor and the elevator's direction is random. Obviously, the shift from the dark to bright state (vice versa) is the critical step when the charge becomes delocalized (localized) and the NC turns *on* (*off*). The observed power law time-dependence can be understood as follows: If the system has been *off* for a long time, the system is deep within the charged state (*off*-region) of the dynamic phase space and is unlikely to enter the neutral state (*on*-region) of the phase space. On the other hand, close to the transition point, the system would interchange between the charged and neutral states rapidly. As the simplest random walk model, we propose an illustrative example of a one-dimensional phase space (figure 2.9a) with a single trap state that is wandering up and down in energy. At each crossing of the trap and intrinsic excited state energies, the NC changes from dark to bright or bright to dark. Since the transition from *on* to *off* is a temperature independent tunneling process, it can only occur when the trap state and excited state of the NC are in resonance. In addition, a temperature-dependent hopping process, related to the movement and creation/annihilation of trapped charges surrounding the NC core [17, 19] drives the trap and excited NC core states to fluctuate in a random walk. The minimum hopping time of the surrounding charge environment gives the minimum time-scale for each step of the random walk to occur. This simple 1-dimensional discrete-time random walk model for blinking immediately gives the

characteristic power law probability distribution of *off*-times with a power law exponent of −1.5 [20]. The intrinsic hopping time is likely to be much faster than our experimental binning resolution (100 msec). Although the hopping mechanism is probably temperature-dependent, this temperature dependence would only be reflected in experiments that could probe timescales on the order of the hopping times, before power-law statistics set in and beyond the reach of our experimental time resolution.

Although this simple random walk model may require further development, it nevertheless explains the general properties observed. The *off*-time statistics are temperature and intensity independent because although the hopping rate of the random walker changes, the statistics of returning to resonance between the trap and excited state does not. In addition, size and surface morphology do not play a significant role in this model as long as a trap state is energetically accessible to the intrinsic excited state. Further experimental and theoretical work is needed to complete this model. For example, temperature and state dependent hopping rates as well as a higher dimension random walk phase space and multiple transition states may be necessary.

2.5.3 Other Models

The random walk model is by no means the only possible explanation for the extraordinary power-law behavior in the *on*-time and *off*-time statistics. Another model is based on a set distribution of trap states surrounding the NC. In ref[21, 22], the authors describe the probability density for charge tunneling rates to be:

$$\beta(r) \sim \exp(-k\,r).$$

This can be argued from the spatial decay of the exciton wavefunction outside the NC boundary. The next step relies on the time in the trap (charged) state. If one assumes a first-order kinetics rate to return, this neutralization rate to the uncharged state will follow

$$P(\tau) \sim \exp(-\beta \tau).$$

When all the possible trap states are accounted for, the probability to return back to the NC core will follow a power law for long times, τ. In addition, an emitting, charged state is described where the extra charge is localized on the surface such that Auger non-radiative relaxation does not occur but coulombic repulsion prevents any charges from also tunneling out near the surface. This model is proposed to explain the power-law behavior for the *on*-time distribution.

2.5.4 Intensity Saturation

The magnitude of truncation of the *on*-time power law distribution depends on which NC is observed as shown in figure 2.6(a) and 2.6(b). In figure 2.6(b), the arrows indicate the *on*-time truncation point for three different NCs under the same excitation intensity at RT. Qualitatively, we can describe and understand the changes as a result of the interaction between the dynamic dark and bright states modeled earlier. As the excitation intensity or thermal energy is reduced, the hopping rate of the random walker slows down and the time constant for the truncation is extended within our experimental time. Surface modification in the form of ZnS overcoating also extends the power law distribution for the *on*-times. This surface modification should not change the hopping rate of the random walker but rather changes the Auger scattering rate. Hence, a mechanism such as photo-assisted ejection of a charge due to Auger ionization[9, 13]

may be responsible for the *on*-time truncation effect. Recently, reversible quenching of CdSe NCs was shown due to interactions with oxygen molecules in the presence of light[23]. Although the single NC blinking data was not interpreted using the power-law statistics, the kinetic behavior is consistent with our description above: the *off*-times are independent of the oxygen molecules introduced; however, the *on*-times show a dramatic decrease in the maximum duration. The simulated time traces in figure 2.9(c), taking into account shorter termination points for the maximum *on*-time relative to the maximum *off*-time, elucidates the difference in blinking at higher temperatures, higher excitation intensity, and poorer surface passivation. The change in the time traces is comparable between the simulation in figure 2.9 and data in figure 2.2.

Recent results on CdTe NCs, displayed in figure 2.4, show that the power law behavior, its exponent, and the *on*-time phenomenology is reproduced, indicating that the effects observed are not unique to the particulars of CdSe NCs, but rather reflect more universal underlying physics of nanocrystal NCs.

2.6 Conclusion

We have used a highly parallel imaging microscope setup to study fluorescence intermittency in single CdSe, CdSe/ZnS core-shell, and CdTe semiconductor nanocrystals, providing insight into the mechanism of single NC blinking dynamics. The statistics of both *on* and *off* time distributions are obtained under varying temperature, excitation intensity, size and surface morphology conditions. Although similar experiments have been conducted earlier, the analysis of the data did not include the framework of power-law statistics, and the data sets were limited to small numbers of

single NCs and relatively short observation times [9, 10]. Here we show an unexpected temperature independence in the observed power-law probability distribution of *off* times. Furthermore, we report that the *on*-time behavior also shows a power law component to the probability distribution. However, a secondary, thermally activated and photo-induced process causes the probability distribution of the *on*-time statistics to be truncated at the 'tail' of the power law distribution. The temperature independent, power law statistics observed for all the CdSe NCs studied suggest a complex, yet universal, tunneling mechanism for the blinking *on* and *off* process.

2.7 References:

1. W.T. Yip, D.H. Hu, J. Yu, D.A. Vanden Bout, and P.F. Barbara, Journal of Physical Chemistry a, 1998. **102**(39): p. 7564.
2. R.M. Dickson, A.B. Cubitt, R.Y. Tsien, and W.E. Moerner, Nature, 1997. **388**(6640): p. 355.
3. M.D. Mason, G.M. Credo, K.D. Weston, and S.K. Buratto, Physical Review Letters, 1998. **80**(24): p. 5405.
4. A.M. Michaels, M. Nirmal, and L.E. Brus, Journal of the American Chemical Society, 1999. **121**(43): p. 9932.
5. M. Sugisaki, H.W. Ren, K. Nishi, and Y. Masumoto, Physical Review Letters, 2001. **86**(21): p. 4883.
6. M. Kuno, D.P. Fromm, A. Gallagher, D.J. Nesbitt, O.I. Micic, and A.J. Nozik, Nano Letters, 2001. **1**(10): p. 557.
7. T. Ha, T. Enderle, D.S. Chemla, P.R. Selvin, and S. Weiss, Chemical Physics Letters, 1997. **271**(1-3): p. 1.
8. M. Kuno, D.P. Fromm, H.F. Hamann, A. Gallagher, and D.J. Nesbitt, Journal of Chemical Physics, 2000. **112**(7): p. 3117.
9. M. Nirmal, B.O. Dabbousi, M.G. Bawendi, J.J. Macklin, J.K. Trautman, T.D. Harris, and L.E. Brus, Nature, 1996. **383**(6603): p. 802.
10. U. Banin, M. Bruchez, A.P. Alivisatos, T. Ha, S. Weiss, and D.S. Chemla, Journal of Chemical Physics, 1999. **110**(2): p. 1195.
11. The power-law distribution for the on times are difficult to fit due to the deviation from power law at the tail end of the distribution. The power-law exponent with the best fit for the on times is observed for low excitation intensity and low temperatures.

12. The ensemble data can differ from the single-dot data because a sum over truncated power laws with different end points leads to a net deviation of the power law distribution.
13. A.L. Efros and M. Rosen, Physical Review Letters, 1997. **78**(6): p. 1110.
14. A.I. Ekimov, I.A. Kudryavtsev, M.G. Ivanov, and A.L. Efros, Journal of Luminescence, 1990. **46**(2): p. 83.
15. D.I. Chepic, A.L. Efros, A.I. Ekimov, M.G. Vanov, V.A. Kharchenko, I.A. Kudriavtsev, and T.V. Yazeva, Journal of Luminescence, 1990. **47**(3): p. 113.
16. P. Roussignol, D. Ricard, J. Lukasik, and C. Flytzanis, Journal of the Optical Society of America B-Optical Physics, 1987. **4**(1): p. 5.
17. S.A. Empedocles and M.G. Bawendi, Science, 1997. **278**(5346): p. 2114.
18. E. Schrodinger, Phys. Z., 1915. **16**: p. 289.
19. R.G. Neuhauser, K.T. Shimizu, W. Woo, S.A. Empedocles, and M.G. Bawendi, Physical Review Letters, 2000. **85**(15): p. 3301.
20. J.P. Bouchaud and A. Georges, Physics Reports-Review Section of Physics Letters, 1990. **195**(4-5): p. 127.
21. M. Kuno, D.P. Fromm, H.F. Hamann, A. Gallagher, and D.J. Nesbitt, Journal of Chemical Physics, 2001. **115**(2): p. 1028.
22. R. Verberk, A.M. Oijen, and M. Orrit, Submitted, 2002.
23. F. Koberling, A. Mews, and T. Basche, Advanced Materials, 2001. **13**(9): p. 672.

Chapter 3 Spectral Diffusion and Blinking [*]

3.1 Introduction

Now that we have examined the blinking statistics in great detail, we can also examine the spectral information for clues to understand the strange kinetics that have besieged single nanocrystal (NC) optical measurements. The spectral identification of single NCs is particularly clear due to (i) the quantum-confined size effect that determines the peak position, (ii) relatively narrow emission peak widths at room temperature (> 14 nm) and cryogenic temperatures (< 0.5 nm), (iii) the optical phonon modes spaced ~25 meV apart, and (iv) the dynamic spectral changes that occur as a function of time at room temperature down to 10 K. This dynamic behavior was termed *spectral diffusion* and includes both the discrete and continuous shifts in the emitting wavelength as a function of time. Since there appears to be no correlation in the magnitude or the direction of the spectral shifts between nearby NCs, we can discriminate whether two or more NCs are aggregated within the resolution of our image detection by monitoring if a single emission peak will split into two or more peaks when the spectrum diffuses. Similar to the blinking behavior described in the previous chapter, spectral diffusion has also been observed in a myriad of single chromophore studies[1-3]. This behavior in NCs was first observed by Empedocles [4] but the data was taken with long integration times (> 10 s) and there was no connection made with the blinking behavior.

In this chapter, we report experimental results that probe both of the optical dynamics in single NCs – spectral diffusion and blinking – simultaneously. The results suggest that the two separate long time dynamical processes that have been observed,

[*] Much of this chapter has appeared in print (Neuhuaser R. G. and K. T. Shimizu *et al.* Phys. Rev. Lett. **85**, 15. p 3301, 2000)

fluorescence intermittency and spectral diffusion, are correlated through redistribution of charged species in and around each individual NC.

3.2 Experimental

The experimental setup is similar to the apparatus described in the previous chapter. The key difference lies in observing single NC emission spectra with fast time resolution (~100 ms). Instead of collecting data in a series of consecutive images, we take all of the NCs imaged on the entrance slit (175 μm) of the monochromator and spectrally resolve their emission as shown in figure 3.1. An advantage of CCD detection over avalanche photodiode or photomultiplier tube detection is that spectral data of single NCs can be obtained in one frame. Moreover, all of the NCs imaged on the entrance slit of the monochromator are observed in parallel. If only relative frequency changes need to be addressed, then the entrance slit can be removed entirely because each NC spot size forms its own spatial point source. This allows for parallel tracking of emission frequencies and intensities of up to 50 nanocrystals. The data analysis software program then retrieves the time-frequency-intensity emission trajectories for all of these NCs.

3.3 Results

The spectrally resolved time-traces shown in figure 3.2(b) and (c) summarize the typical phenomenology of spectral shifting and blinking for different quantum NCs at low temperature (10 K) and room temperature, respectively. Both RT and the 10 K data show blinking dynamics along with changes in the emission energy. The differences,

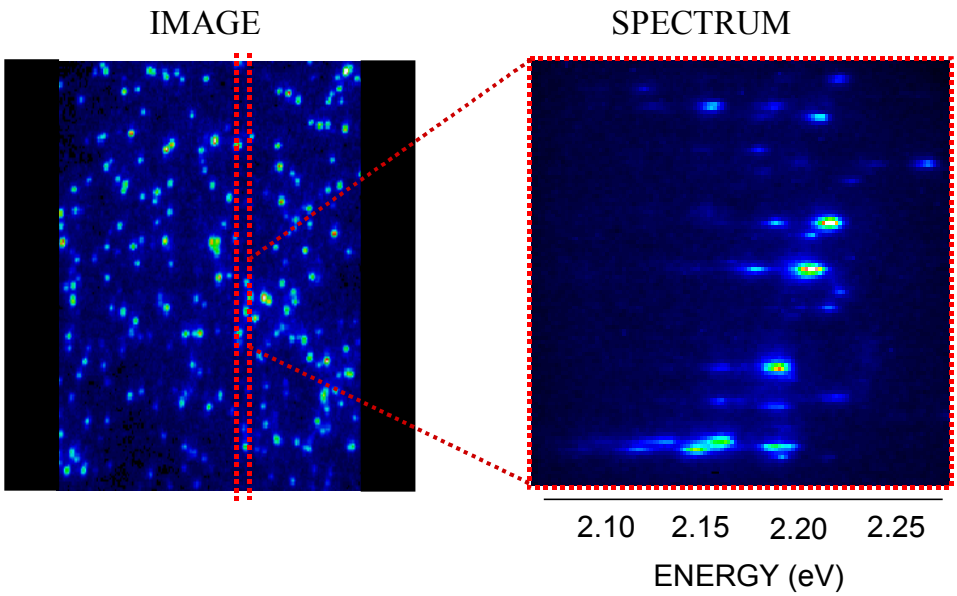

Figure 3.1: Single CdSe NC images and corresponding spectra. The entrance slit is closed to filter out all but one NC at each vertical position. If the entrance slit is left wide open, then the laser line will produce a broad background centered about the laser position. However, far from the laser line (and higher order harmonics), the single NC image spots can form its own slit and relative spectral behavior can be analyzed with higher sample throughput.

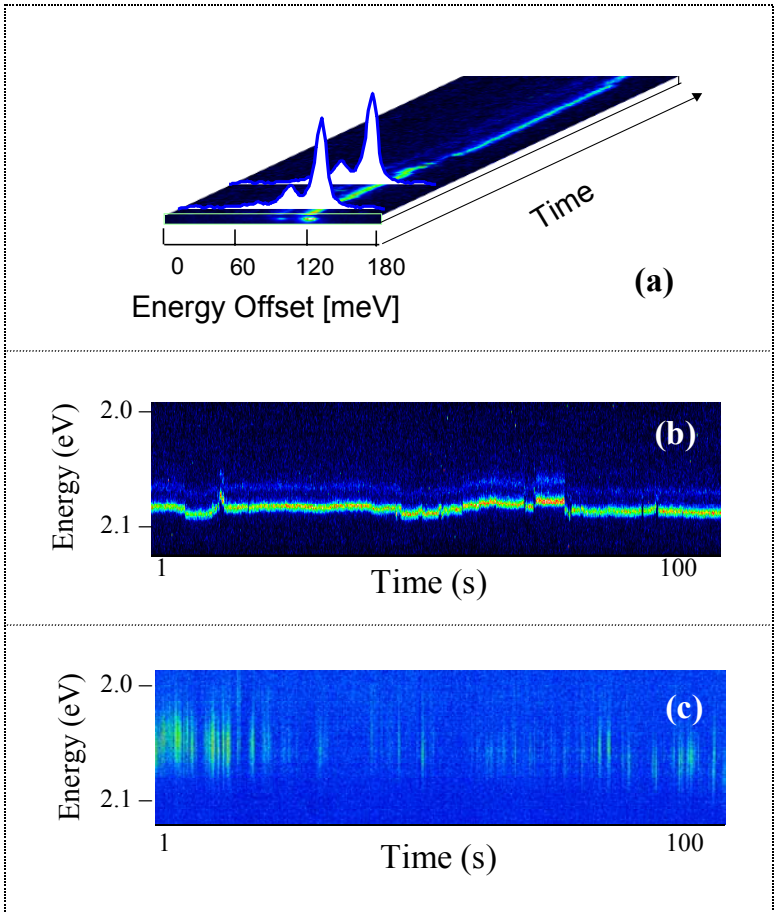

Figure 3.2: Spectral time trace of a single CdSe/ZnS QD at 10K. The phonon progression (~25meV) can be seen to the red of the strongest zero-phonon peak. A comparison between spectral time traces for **(b)** 10K and **(c)** room temperature shows that spectral diffusion is present at both temperatures.

however, are quite clear. At RT, thermal contributions to the homogenous linewidth conceal any phonon-assisted emission profile. Furthermore, the signal-to-noise is diminished for RT data since the NC has lower quantum yield and the photons are spread over several more pixels on the CCD detector. As the temperature falls below ~30 K, the spectral linewidth decreases and phonon progression features, the zero and first phonon lines, are observable as shown in figure 3.2(a). We can see the variable nature of spectral diffusion for different dots and short observation times in figure 3.3(a-c). Time-traces of these three NCs were observed simultaneously. The spectrum in figure 3.3(a) shows sharp emission lines with nearly constant frequency and intensity, the spectrum in figure 3.3(b) shows some pronounced spectral shifts and a few blinking events, and the spectrum in figure 3.3(c) is fluctuating in frequency and shows a number of blinking events on a much faster time-scale. The spectral information clearly shows that, for a single quantum NC under the perturbations of its environment, there are many possible transition energies (i.e. a dynamically changing emitting state). Net shifts as large as 14 nm were observed in our experiments. The organic dye molecule system described in chapter I applies a static three (or four) level model to describe the emission dynamics; however, in light of our spectral data, a similar model would not describe our single NC system. Rather, these emission dynamics suggest a NC intimately coupled to and reacting to a fluctuating environment. We expect from this observation that physical properties like fluorescence lifetimes or quantum efficiency, even when measured on a single NC basis, will provide average values over a large number of different states of the NC/environment system. Recently, fluctuations in room temperature single NC lifetimes (as we had predicted) have been reported by Schelgel *et al*[5]. Zooming into the time

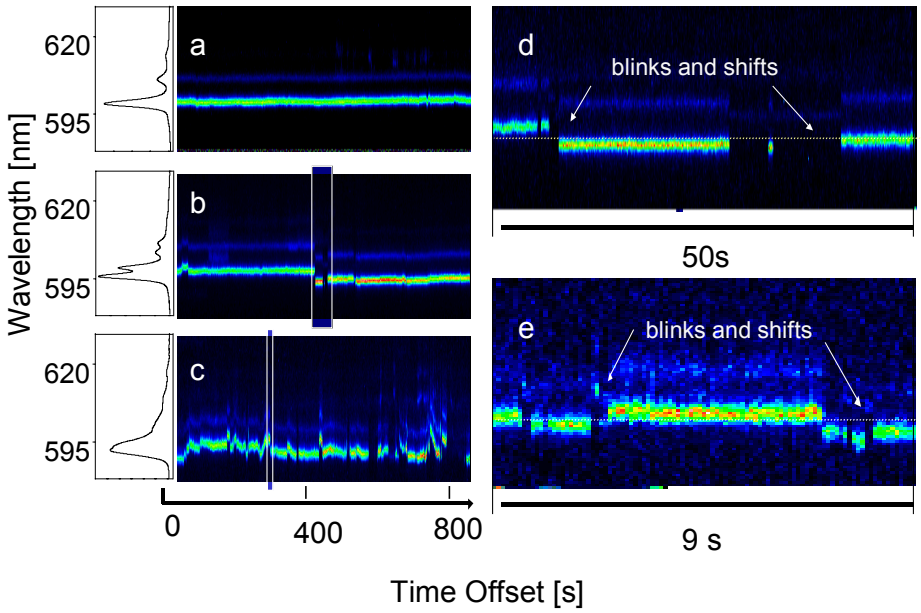

Figure 3.3: Low temperature spectral time trace of three CdSe/ZnS NCs demonstrating the different dynamics observed simultaneously on short time scales. The resulting averaged spectrum is plotted for each NC. The boxed areas in **(b)** and **(c)** are magnified and shown in **(d)** and **(e)**. The blinking back "on" after a dark period is accompanied by a large spectral shift. The white dotted line is drawn in **(d)** and **(e)** as a guide to the eye.

traces of figure 3.3(b) and 3.3(c) reveals that blinking and hopping between these multiple emitting states is *correlated*. As shown in figure 3.3(d), magnifying the marked region in the time-trace of figure 3.3(b) reveals a pronounced correlation between individual spectral jumps and blinking: following a blink-*off*/blink-*on* event, the energy of the emitted photons is changed. At first glance, this does not seem to hold for the NC shown in figure 3.3(c). However, as shown in figure 3.3(e), zooming into the time-trace of figure 3.3(c) reveals a similar correlation. As in figure 3.3(d), the trace shows dark periods that are accompanied by discontinuous jumps in the emission frequency. The periods between shifts in figure 3.3(d) and 3.3(e), however, differ by nearly an order of magnitude in timescales. Due to our limited time resolution, no blinking events shorter than 100 ms can be detected. Any fluorescence change that is faster than the 'blink-and-shift' event shown in figure 3.3(e) is not resolved by our apparatus and appears in a statistical analysis as a large frequency shift during an apparent on-time period. This limitation weakens the experimentally observed correlation between blinking and frequency shifts. Nevertheless, a statistically measurable difference between shifts following on and off-times can be extracted from our results.

3.4 Discussion

3.4.1 Statistical Analysis

Since changes in the emitting state cannot be observed when the NC is *off*, we compare the net shifts in the spectral positions between the initial and final emission frequency of each *on* and *off* event. The histogram of net spectral shifts during the on times, shown in figure 3.4(a), reveals a nearly Gaussian distribution (dark line) with 3.8

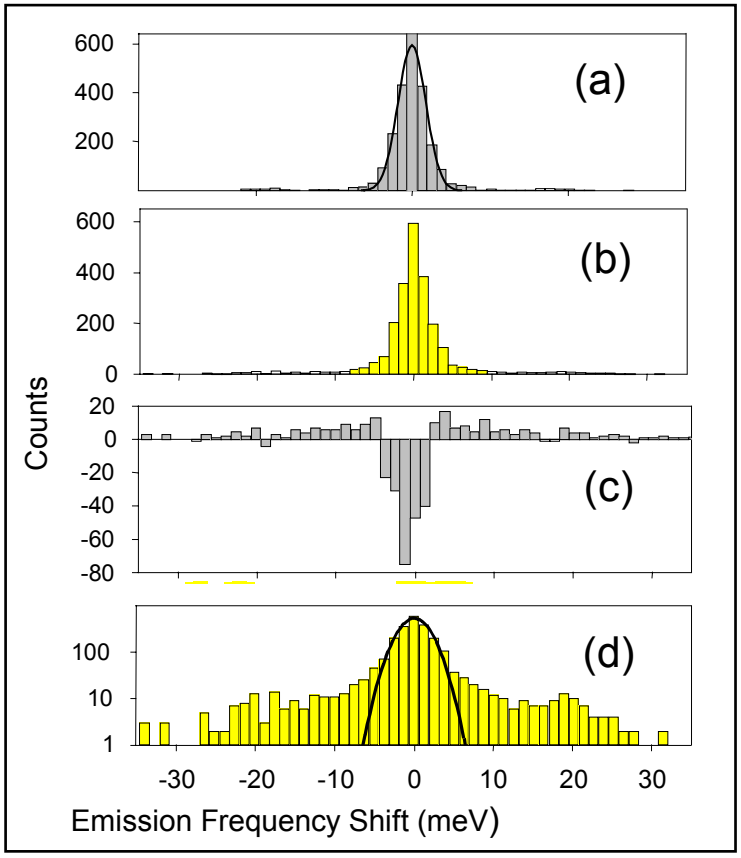

Figure 3.4: Distribution of net spectral shifts between the initial and final emission frequency for 2400 on and off periods of 9 CdSe/ZnS NCs at 10K. (a) Histogram of net spectral shifts for the on period shows a Gaussian distribution of shifts. The dark line is a best fit to Gaussian profile. (b) Histogram for off periods displays large counts in the wings of a similar Gaussian distribution. (c) Subtracting the on-period distribution from the off period distribution magnifies the large counts in the wings of the Gaussian distribution. This quantifies the correlation that the large spectral shifts accompany an off event (longer than 100ms) more than an on event. (d) A logarithmic plot of the histogram shows a clearer indication of the non-Gaussian distribution in the net spectral shifts during the off-times. The dark line is a best fit to a Gaussian profile.

meV full width at half maximum. However, the histogram for the off-time spectral shifts in figure 3.4(b) shows a distribution better described as a sum of two distributions: a Gaussian distribution of small shifts and a distribution of large spectral shifts located in the tails of the Gaussian profile that do not fit a simple Gaussian distribution. To illustrate the difference between the distributions of on and off-time spectral shifts, the on-time spectral distribution is subtracted from the off-time spectral distribution shown in figure 3.4(c). Even though our measurements have a time resolution of 100 ms, this difference histogram shows that large spectral shifts occur significantly more often during *off*-times (longer than 100 ms) than during *on*-times; hence, large spectral shifts are more likely to accompany a blink-*off* event than during the time the NC is *on*. This statistical treatment does not try to assess the distribution of NCs that show this correlation but rather confirms the strong correlation between spectral shifting and blinking events in the NCs observed. The *off*-time histogram, plotted on a logarithmic scale in figure 3.4(d), shows that a Gaussian distribution (dark line) does not describe the distribution of *off*-time spectral shifts [6].

The correlation observed between blinking and spectral shifting events elucidates the possible mechanisms behind these dynamical processes. The two behaviors have been described as a consequence of the interaction between the NC and the local environment, but a correlation between blinking and spectral shifting events had not been predicted. This correlation differs from blinking *caused* by spectral shifting observed in single molecules such as pentacene in a p-terphenyl matrix [7],[8]. In single molecule experiments, the chromophore is resonantly excited into a single absorbing state and a spectral shift of the absorbing state results in a dark period since the excitation is no

longer in resonance. In our experiments, we excite non-resonantly into a large density of states above the band-edge[9].

3.4.2 The Model: charges in (and out of the) nanoenvironment

An early model [10] described the fluorescence intermittency results based on a photo-ionization process. The transition from a bright to a dark NC occurs through the trapping of an electron or hole leaving a single delocalized hole or electron. Upon further excitation of the NC, fast non-radiative relaxation follows due to energy transfer from the exciton to the delocalized charge carrier through the Auger mechanism [11]. The switch from a dark to a bright NC then occurs through recapture of the initially localized electron (hole) back into the NC core or through capture of another electron (hole) from nearby traps. When the electron-hole pair recombines, the NC core is no longer a site for exciton-electron (exciton-hole) energy transfer. Concomitantly, *Empedocles et al*. [12] showed evidence that spectral diffusion shifts are caused by a changing local electric field around the NC. The magnitude of the changing local electric field was consistent with a single electron and hole trapped near the surface of the NC.

We can now combine both models to explain the correlation as shown in Figure 3.3(d) with the arrows between large spectral jumps and blinking. Using the assumption that a charged NC is a dark NC [13], there are four possible mechanisms for the transition back to a bright NC. Cartoon drawings depicting the four different mechanisms are shown in figure 3.5. EFM studies on single CdSe NCs recently showed positive charges present on some of the NCs [14] even after exposure to only room light. In our model, after CW laser excitation and exciton formation, the NC turns "off" when an electron or

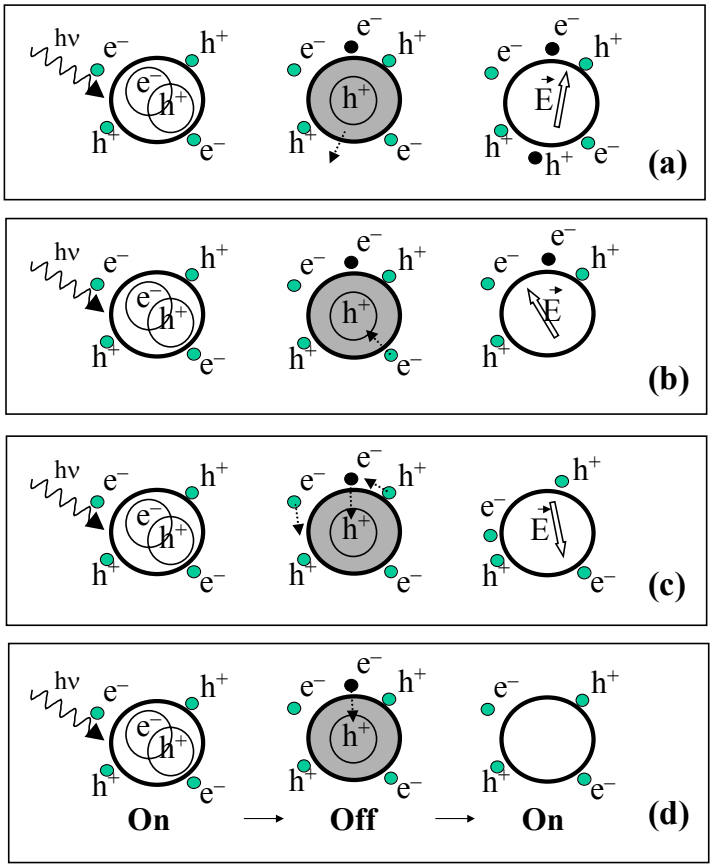

Figure 3.5: Four possible mechanisms for the correlation between spectral shifting and blinking. **(a)** An electron and hole become localized independent of the other charges surrounding the QD leading to a change in the electric field environment. **(b)** An electron from the core localizes to the surface, but a surrounding charge is recaptured into the core. After recombination with the delocalized hole, the net electric field has changed. **(c)** Although the same electron that was initially localized returns to the core to recombine with the delocalized hole, due to coulomb interaction, the charge distribution surrounding the QD has changed. **(d)** The same electron initially localized returns to the core to recombine with the delocalized hole and there is no change in the local electric field around the QD.

hole from the exciton localizes near the surface of the NC leaving a delocalized charge carrier inside the NC core. Following this initial charge localization or ionization, the NC turns back "on" as a result of the following possible mechanisms: (a) the delocalized charge carrier can also become localized near the surface leading to a net neutral NC. This localization may be thermally driven, or more likely driven through the Auger process itself. (b) If the NC environment is decorated by charges following process (a), then after subsequent ionization, a charge localized in the NC's nearby environment can relax back into the NC core recombining with the delocalized charge carrier, or (c) the initial localized charge relaxes back into the core and recombines with the delocalized carrier. This last mechanism can be accompanied by a permanent reorganization of the localized charges present in the NC environment due to coulombic interactions as the photogenerated carrier traps and detraps. Mechanisms (a), (b), and (c) would create, if not alter, a surface dipole and lead to a net change in the local electric field. The single NC spectra express this change as a large Stark shift in the emission frequency. However, the model does not necessarily require that a blinking event be followed always by a shift in emission frequency. If the dark period is produced and removed by a localization and recapture of the same charge without a permanent reorganization of charges in the environment (mechanism d), the emission frequency does not change. Any changes in the emission frequency during this mechanism would be entirely thermally induced and such small spectral shifts are observed. Indeed, this pathway for recombination dominates very strongly, as most dark periods are not accompanied by large frequency shifts. The processes described under mechanism (a), (b), and (c) appear much less likely to occur. Nevertheless, these processes can introduce an increased

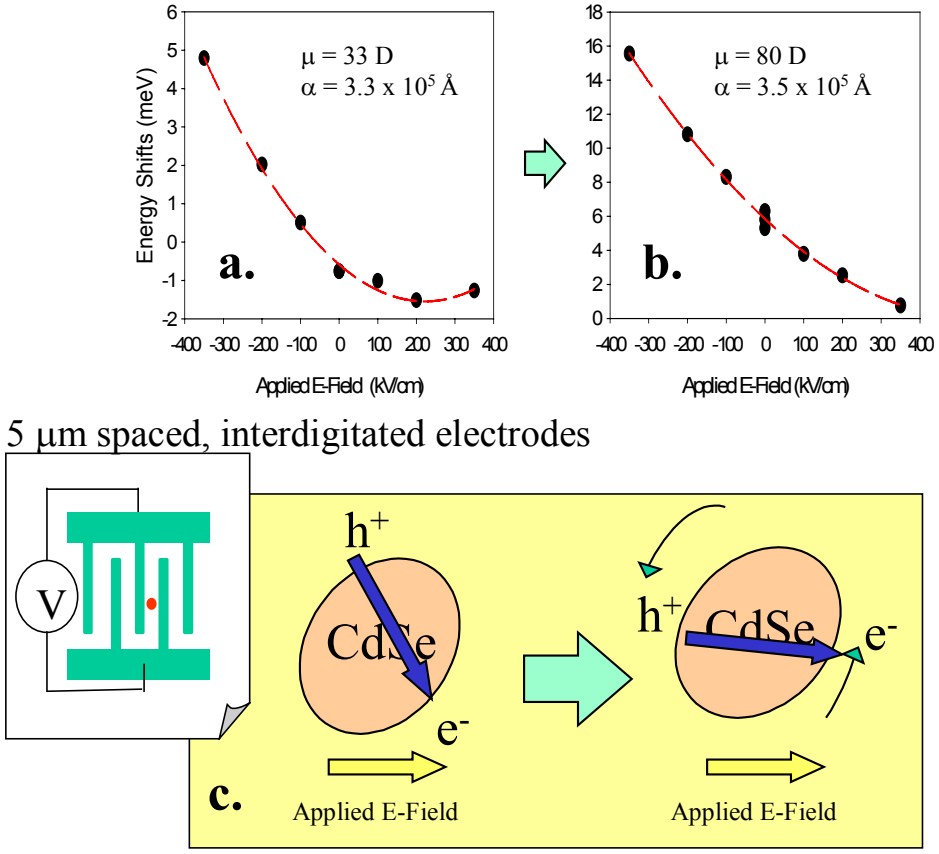

Figure 3.6: Typical single CdSe NC Stark spectrum (a) before and (b) after a spectral diffusion shift has occurred. The schematic of the spectral diffusion mechanism is drawn in (c). The inset shows the microfabricated electrode substrate used where the red dot exemplifies a single NC.

complexity to the observed dynamics.

3.5 DC Stark Spectroscopy Experiments

We performed Stark spectroscopy on the NCs to test whether the charges described above may be perturbed by an externally applied DC electric field. For this purpose, we used lithographically deposited, interdigitated gold electrodes to apply fields up to 4 x 10^5 V/cm across the NCs. Earlier work showed that spectral diffusion jumps occurred independent of the applied field[12]. As an example, figure 3.6(a) shows a typical Stark spectrum of a single NC. The Stark energy shift can be described by

$$\Delta E = \mu_z \mathrm{E}_z + \alpha_{zz} \mathrm{E}_z^{\,2} \qquad (1)$$

where μ_z is the dipole moment of the NC, E_z is the electric field, and α_{zz} is the NC polarizability. Local electric fields from surface charges can contribute to the total E_z field:

$$\mathrm{E}_{z,\,\mathrm{total}} = \mathrm{E}_{z,\,\mathrm{local}} + \mathrm{E}_{z,\,\mathrm{applied}} \qquad (2)$$

Then inserting equation (2) back into equation (1), the total linear contribution is a sum of the intrinsic dipole moment and the local field multiplied to the NC polarizability. This can be observed by comparing figure 3.6(a) and (b), where the same NC shows drastic changes to the magnitude of the stark linear response before and after a spectral diffusion shift has occurred. Figure 3.6 (c) describes how the spectator charges may have changed leading to a change in the linear Stark spectrum. However, the quadratic term does not change as the charge environment of the NC changes. In figure 3.7, we show preliminary attempts to change the blinking-spectral diffusion behavior by applying electric fields at fixed intervals at 10 K. The electric field (4 x 10^5 V/cm) is toggled back and forth

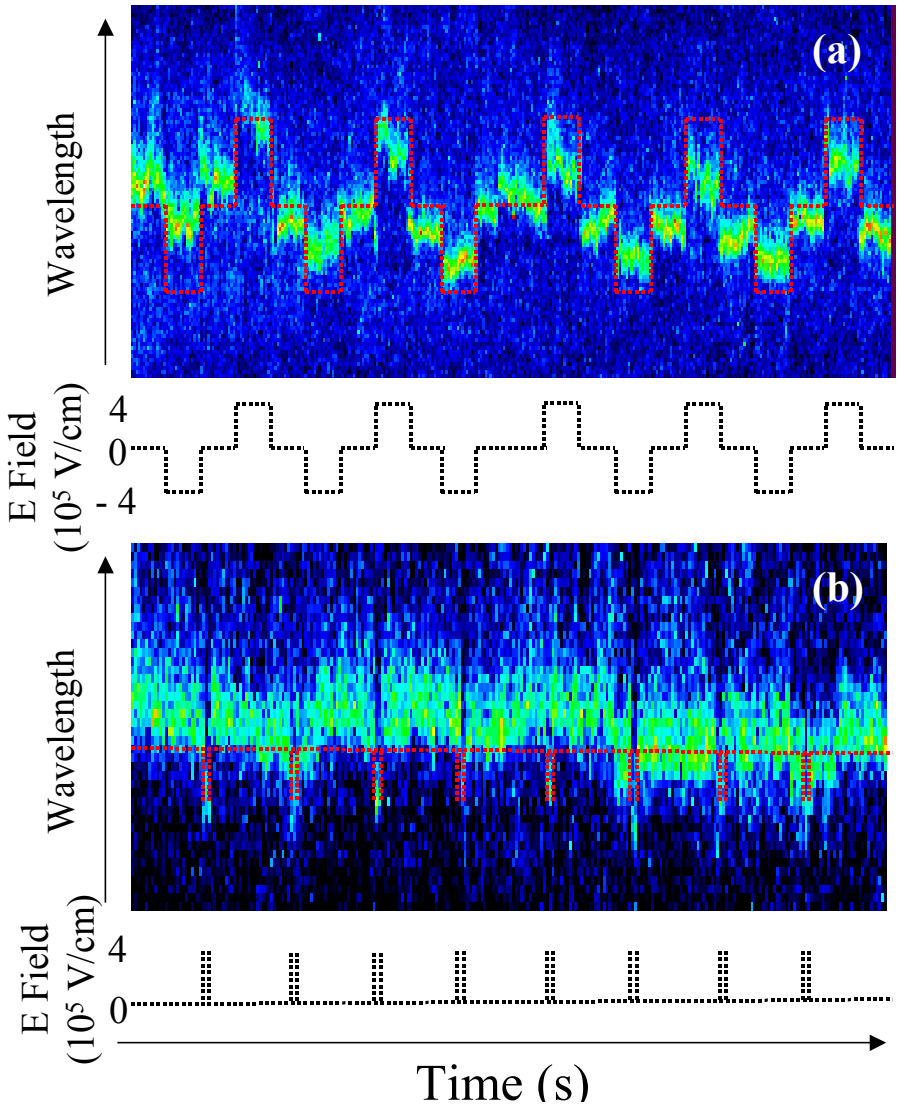

Figure 3.7: Stark spectra time trace. (a) The field is toggled from 4 x 10^5 V/cm to 0 V/cm to –4 x 10^5 V/cm in 30 s intervals. (b) The field is held at 0 V/cm for most of the time and switched on momentarily (2 s) to 4 x 10^5 V/cm. In both cases, the spectra respond to the applied field but there is no residual change (memory) in the local electric field that should be reflected in the emission position after the external field has turned back off. Data taken with 1s integration times.

between positive, zero, and negative bias or simply turned on for 2 s at 30 sec intervals. If the applied fields were large enough, we expect the spectator charges described in figure 3.5 to adjust. However, in this case, no spectral residual effects are observed after applying the large electric field bursts.

3.5 Conclusion

In conclusion, we have shown a strong correlation between large spectral shifting events and blinking of single nanocrystals by measuring simultaneously fluorescence intensity and fluorescence frequency of single NCs. This dynamic behavior can be explained by extending the photo-ionization model that describes blinking in semiconductor nanocrystals as a result of a NC ionization and Auger electron-exciton (hole-exciton) energy transfer, a mechanism that differs from the process known to cause blinking in single molecules.

3.6 References

1. W.E. Moerner, T. Plakhotnik, T. Irngartinger, M. Croci, V. Palm, and U.P. Wild, Journal of Physical Chemistry, 1994. **98**(30): p. 7382.
2. L. Fleury, A. Zumbusch, M. Orrit, R. Brown, and J. Bernard, Journal of Luminescence, 1993. **56**(1-6): p. 15.
3. J. Wrachtrup, C. Vonborczyskowski, J. Bernard, M. Orrit, and R. Brown, Nature, 1993. **363**(6426): p. 244.
4. S.A. Empedocles, D.J. Norris, and M.G. Bawendi, Physical Review Letters, 1996. **77**(18): p. 3873.
5. G. Schlegel, J. Bohnenberger, I. Potapova, and A. Mews, Physical Review Letters, 2002. **88**(13): p. art. 137401.
6. The *on*-time histogram also has weak tails on top of the Gaussian distribution because of apparent *on*-time spectral shifts that may have occurred during an *off*-time faster than the time resolution (100 ms) allowed by our present setup.
7. W.P. Ambrose and W.E. Moerner, Nature, 1991. **349**(6306): p. 225.
8. T. Basche, Journal of Luminescence, 1998. **76-7**: p. 263.

9. D.J. Norris and M.G. Bawendi, Physical Review B-Condensed Matter, 1996. **53**(24): p. 16338.
10. M. Nirmal, B.O. Dabbousi, M.G. Bawendi, J.J. Macklin, J.K. Trautman, T.D. Harris, and L.E. Brus, Nature, 1996. **383**(6603): p. 802.
11. D.I. Chepic, A.L. Efros, A.I. Ekimov, M.G. Vanov, V.A. Kharchenko, I.A. Kudriavtsev, and T.V. Yazeva, Journal of Luminescence, 1990. **47**(3): p. 113.
12. S.A. Empedocles and M.G. Bawendi, Science, 1997. **278**(5346): p. 2114.
13. Note: we make a distinction between a charged NC where the charge is delocalized in the core of the NC (a dark NC) and a charged NC where the charge refers to trapped charges localized on the surface or in the organic shell surrounding the NC (not necessarily a dark NC).
14. T.D. Krauss and L.E. Brus, Physical Review Letters, 1999. **83**(23): p. 4840.

Chapter 4 Surface Enhanced Fluorescence [*]

4.1 Introduction

Metallic interfaces play a complex role in the basic interactions of an electromagnetic field with optically active materials. For example, smooth metallic surfaces reduce the radiation from nearby organic dyes through non-radiative energy transfer [1], while molecules adsorbed onto rough metallic electrodes [2] show orders of magnitude increase in surface-enhanced Raman signals. Colloidal semiconductor nanocrystal quantum dots (NCs) can be considered as unique testing materials for electromagnetic-radiating dipole interaction models because of their nature as "customizable" chromophores that can be tailored to absorb or emit light anywhere in the visible spectrum, and beyond [3]. Yet, there is little known about chromophore-metal surface interactions for colloidal semiconductor NCs. Recent advances in single molecule detection offer an opportunity to probe and understand the details of optical quenching or enhancement, details that are hidden in ensemble experiments by sample inhomogeneity [4,5]. Furthermore, there is continued interest in increasing the maximum rate of photons emitted as well as in understanding the sensitivity of NC chromophore properties to their immediate environment. Such advances would help to better implement NCs in biological and solid-state device applications. We combine a study of NC-metal surface interactions with single molecule detection methods to show that novel photophysics emerges from having a NC next to a rough metal surface. We find that radiative and non-radiative relaxation rates are strongly affected, and that the usually dominant Auger non-radiative relaxation channel is no longer competitive. We focus on

[*] Much of this work will appear in print (K. T. Shimizu *et al.* Accepted in Phys Rev Lett 2002.)

single CdSe(ZnS) NC investigations that reveal surface-enhanced exciton fluorescence via an electromagnetic interaction with the gold surface plasmon. This intensity enhancement can reach five-fold and is accompanied by dramatic changes in the dynamical optical behavior (blinking [6-9] and spectral diffusion [10]), the emission polarization, and the fluorescence lifetime. Surface-enhanced fluorescence experiments at cryogenic temperatures on single NCs show that (i) blinking effects are dramatically diminished and (ii) emission energy jumps now follow the same statistical behavior as the blinking behavior of NCs on non-metallic substrates. These results suggest that the ionization mechanism usually responsible for blinking remains, but emission from both charged and neutral excitons in individual nanocrystals is now observed.

4.2 Experimental

We used far-field photoluminescence microscopy to investigate the surface enhancement properties of the fluorescence in single CdSe(ZnS) NCs on rough gold surfaces. The substrates were fabricated by thermal evaporation of titanium/gold (20nm/120nm) on silicon wafers followed by electrochemical etching. Atomic force microscopy studies, shown in figure 4.1, confirmed the formation of rough valleys and peaks with 10~50 nm size features. CdSe(ZnS) core-shell nanocrystals were synthesized following the methods in Ref.[11-13]. Single NCs were dispersed by spin-coating dilute samples directly onto the gold substrates. We used the 514 nm line of an Ar ion CW laser for sample excitation. Further instrumental details are described elsewhere [10].

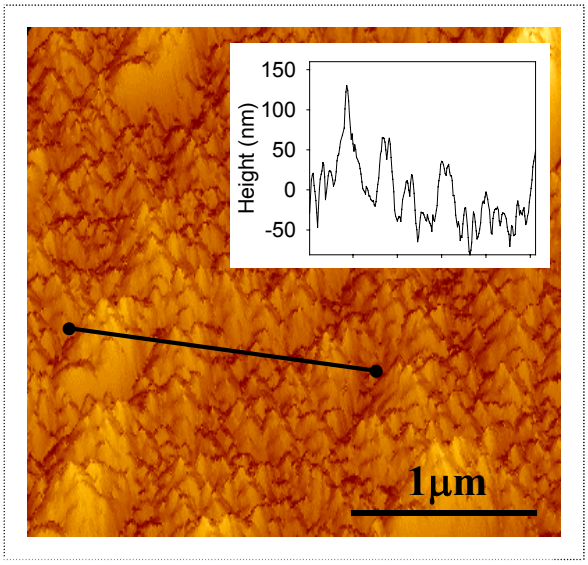

Figure 4.1: A 3µm x 3µm AFM image of a sample gold substrate after the electrochemical-etching procedure outlined in the text. The cross-sectional view (inset) shows various hills and valleys in the 75nm size range.

4.3 Results

Initial experiments of CdSe(ZnS) NCs on *smooth* gold substrates showed an immediate quenching of the luminescence, a behavior that has been well documented with various organic dye molecules. We observed an increase in the number of emitting individual NCs as we increased the surface roughness while keeping the (dilute) concentration of NCs constant. Of the detectable NCs, we typically measured a three to five-fold increase in the fluorescence intensity (figure 4.2a.), as compared to the same NCs placed on crystalline quartz substrates under identical conditions. Furthermore, the duration of "*on*" times increases to a point where the frequency of blinking events appreciably diminishes. A large distribution of NC/gold coupling strengths exists as some NCs show as much as five-fold increase in fluorescence intensity, while other NCs show diminished fluorescence.

4.3.1 Power-Law Spectral Jumps

Figure 4.2 (b) shows the dynamic behavior observed for single CdSe(ZnS) NCs at 10 K on quartz substrates [14]. The optical fluctuations include the *on-off* blinking of the emission intensity as well as large and small continuous spectral shifts. In Figure 4.2(c), the low temperature emission from a single NC interacting with the rough gold surface is shown. The spectral shifts occur more frequently as discrete shifts and there is no "*off*" behavior during the entire scan. We can identify two categories of spectral shifts that are present: the first type is *binary* with energies ranging from 10~22 meV and the second type is a more continuous, small shift that appears random in direction and magnitude. This behavior was observed over many (>50) NCs on many similarly

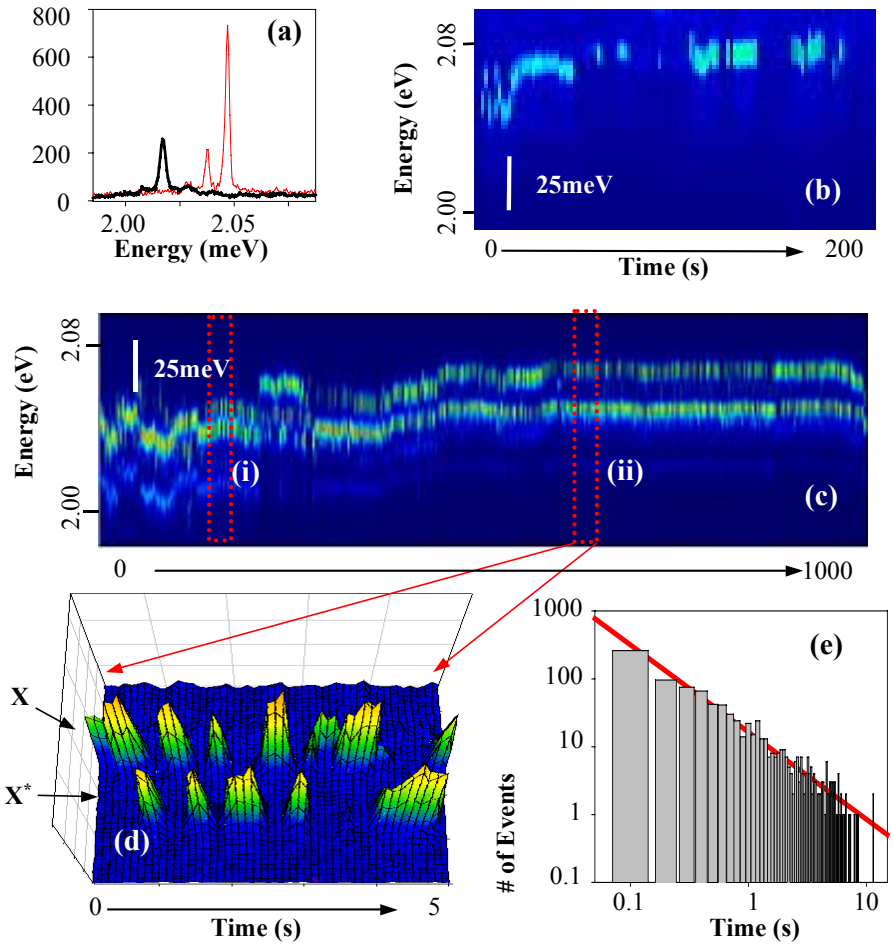

Figure 4.2: (a) shows the relative intensity difference of the emission peaks between normal (black line) and enhanced (red line) NCs. A spectral diffusion trajectory of a single CdSe/ZnS nanocrystal (b) in poly(methyl-methacrylate) polymer on quartz substrate and (c) on a roughened gold surface with no polymer matrix. (a),(b), and (c) taken with 100 ms integration time and 514 nm CW laser excitation (200 W/cm^2). Magnified spectrum in (d) shows the clear binary shifts from (c) with the proposed charged and neutral exciton peaks labeled. (e) Statistical distribution of the time intervals in between discrete spectral shifts plotted on a log-log scale. The straight line is a best-fit curve to a power-law ($P = t^{\alpha}$) where $\alpha = -1.4$.

prepared substrates.

Previous work analyzing the statistics of the fluorescence intermittency (blinking) showed that the *on* and *off*-times follow a universal power-law distribution: every single CdSe(ZnS) NC blinks *on* and *off* and follows a power-law distribution in the histogram of *on* and *off*-time durations [15, 16]. This power-law was attributed to the statistics of the tunneling kinetics of an extra charge between localized and delocalized states of the NC. Similarly, we measure the time intervals between spectral jumps for the NCs coupled to the gold substrates. We plot a histogram of these "wait" times in figure 4.2(e). Apparent in the log-log plot, we see that the distribution of wait times also shows a power-law distribution. Moreover, the exponent of the power is –1.4, similar to the results seen in previous blinking studies (–1.5 exponent).

4.3.2 Emission Polarization

To verify the NC/surface interaction, we also probed the emission polarization. The symmetry of the CdSe NC shape and crystal structure gives rise to a doubly degenerate emitting state with a 2-dimensional emission polarization [17]. Figure 4.3(a) and (b) show RT NC images and 10 K NC spectra, respectively, as the polarization analyzer is rotated. The surface interaction results in a conversion of the NC emission from a degenerate to a non-degenerate linear dipole. All of the NCs show emission polarization consistent with a linear dipole at 10 K and at room temperature; the emission polarization is easily measured even at room temperature due to the decrease in blinking that would normally result in large intensity fluctuations [18]. The polarization change is not an artifact of the experimental setup as the phase of the polarization from individual

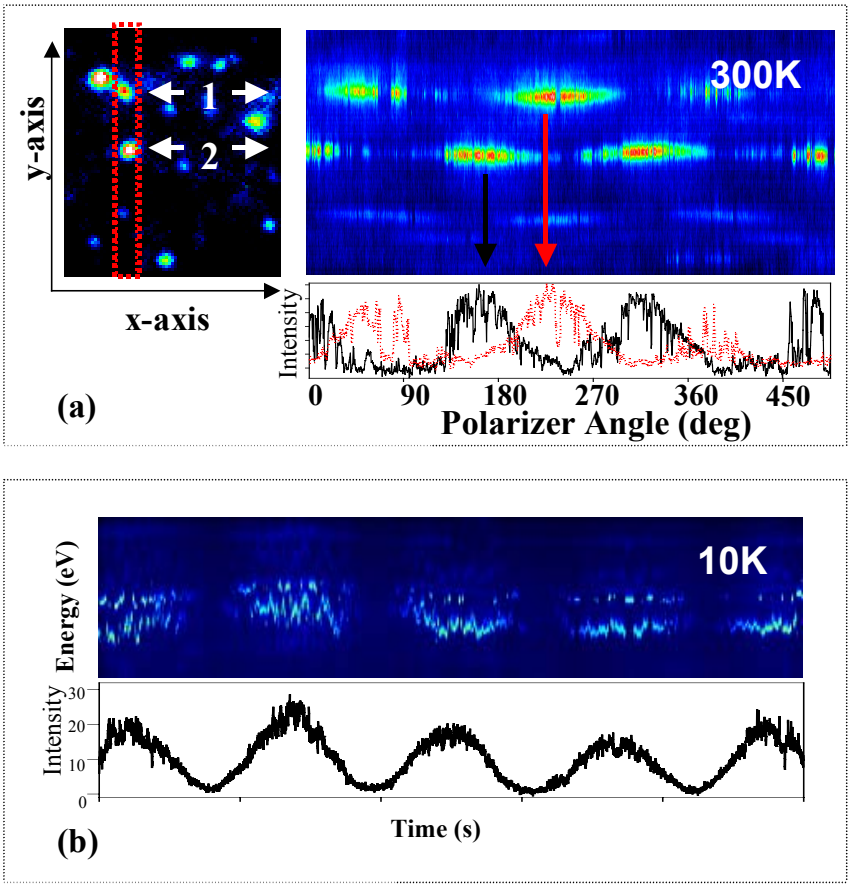

Figure 4.3: (a) RT images monitoring the emission polarization of single NC coupled to gold substrates. (left) Single NC image averaged over 10 frames. (right) Emission polarization of single NCs while the linear analyzer is rotated continuously during the scan. Data taken with 100 ms integration time and 150 W/cm^2 laser excitation.
(b) 10 K spectra showing that the spectral emission peaks (jumping back and forth) are both linearly polarized and in phase.

NCs differs from that of the laser and from that of nearby NCs.

4.3.3 Excited State Lifetimes

Finally, we measured the exciton lifetime for NCs interacting with the gold surface. Figure 4.4(a) and (b) show the instrumentation used and the corresponding image of single NCs captured on the LaVision CCD camera, respectively. Figure 4.4(c) shows 40 single CdSe(ZnS) NC exciton lifetimes at 10 K simultaneously. These individual NCs were easily imaged and fluorescence lifetimes as fast as 130 ps were measured. The red trace in figure 4.4(d) is a plot of one of the NCs in figure 4.4(c). The black trace shows the lifetime of an ensemble CdSe(ZnS) NC film at 10 K; although multi-exponential, the lifetime is roughly on the order 200 ns. NC ensemble fluorescence lifetimes have previously also been reported as ~20 ns at room temperature [19] and ~150 ns at 10 K [20].

4.3.4 Hot Band Emission

During a few spectral trajectory scans, we observed a blue shifted emission (roughly 125 meV away from the band edge emission in figure 4.5a). Since an ensemble of NCs includes a distribution of sizes, this may be emission from a nearby smaller NC. However, when we inspect the emission trajectory of the band-edge and blue shifted peaks, we find an exact correlation to every spectral diffusion shift, shown in figure 4.5(b). This would seem highly unlikely from two NCs even adjacent to each other. Polarization measurements have shown that they also have the same phase in the linear polarized emission. The assignment of these features to hot-band emission is tentative

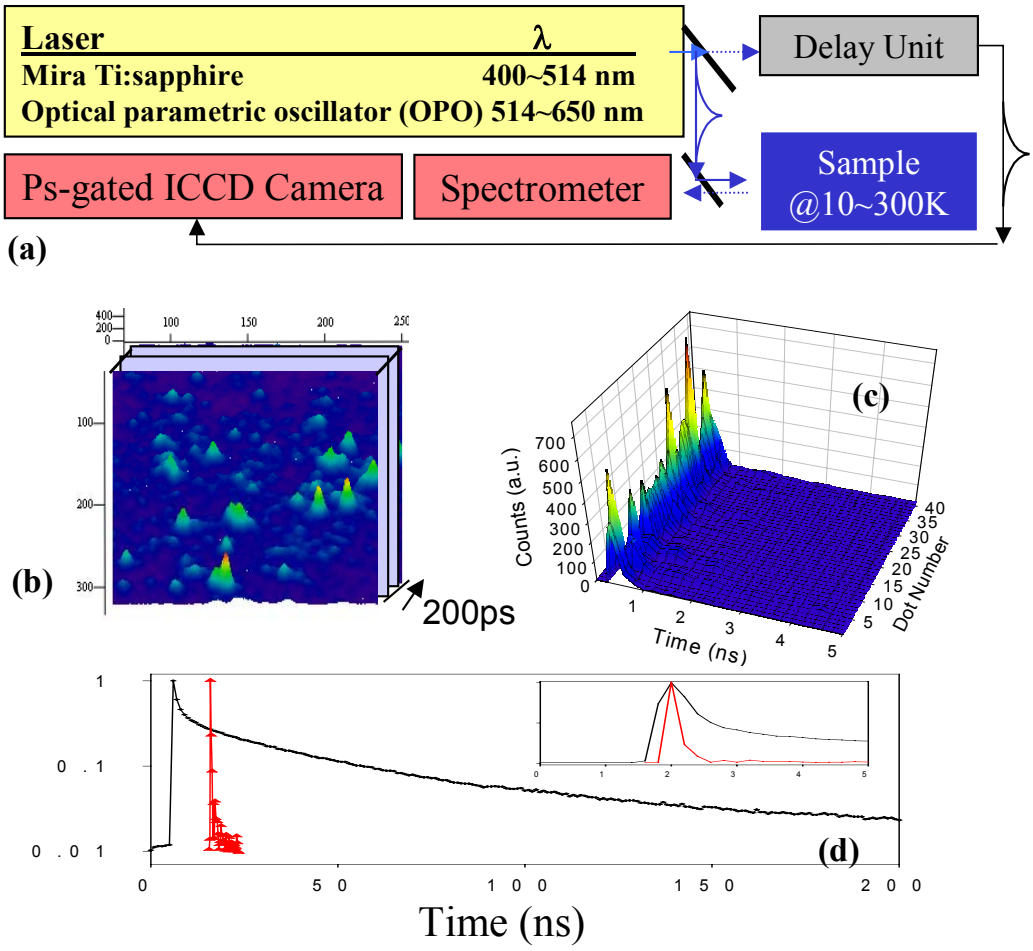

Figure 4.4: (a) Layout of the fs/ps ultra-fast laser and detector system. (b) Image of single NCs on the gated, intensified CCD camera (LaVision Picostar). Photodecay scan taken with 533 nm, ps-pulsed excitation, 300W/cm^2 (Coherent Mira/OPO) at 10 K. (c) 3-D plot showing the decay of 40 individual NCs taken simultaneously.
(d) Comparison of time scales between lifetime of an ensemble film (black) and a single CdSe/ZnS NC interacting with the gold substrate (red); the two decays are offset in time for ease in comparison. Inset shows the same curves in a linear plot for the first 5 ns, now superimposed in time.

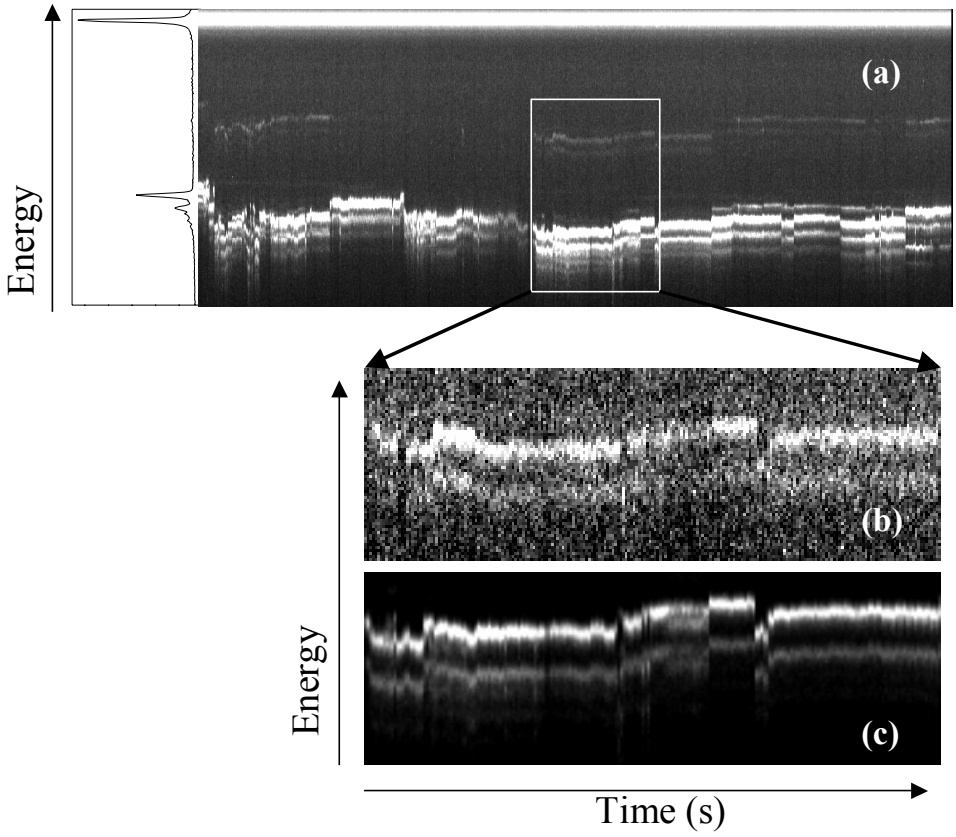

Figure 4.5: (a) CdSe/ZnS NC on roughened gold surface at 10 K. Emission spectra shows blue shifted peaks at certain times. Both peaks have phonon-progression indicative of semiconductor NC emission. Zooming into the center area of (a), we can see that (c) and (d) have identical spectral diffusion traces but at different wavelengths. At this point, we speculate that this may be evidence for hot-band emission from single NCs. The increase in lifetimes may indeed allow for observing hot-band emission.

since we do not have a consistent spacing between the band-edge and blue-shifted emission.

4.4 Discussion

4.4.1 Charged Exciton Emission

The blinking model suggests that fast Auger relaxation rates [6,21] are responsible for quenching the emission from charged exciton in CdSe NCs. Theoretical predictions indicate that if the emission were observable, the charged NC should emit 25 meV to the red of the neutral exciton emission [22]. In the context of our results, we propose that the observed binary emission shifts are caused by neutral (X) and charged (X*) exciton emission from a single NC for the following reasons: First, the binary shifts in the emission energy fluctuate between two positions with a spacing of 15~25 meV. Second, these shifts are not optical phonon progressions since the two emissions seldom emit together within our integration bin time. This also excludes the possibility of biexciton emission. If a biexciton were created, we would observe both lines simultaneously within our integration time as the biexciton relaxes to the exciton radiatively, followed by exciton emission [23]. A charged exciton, on the other hand, would relax to a charged NC, which can persist for many seconds or longer. Third, and possibly most significant, the statistics of the dynamics between the two emissive states follows a power-law distribution matching that of the kinetics observed in previous blinking studies.

When we examine the magnitudes of the binary shifts ($X \rightarrow X^*$), we observe that there is a correlation between the spectral position of the high-energy peak (labeled X in

Figure 4.2d) and the size of the energy jump (ΔE) from X to X^*. In Figure 4.2(c), the region marked (i) has ΔE ≈ 10 meV with the spectral position of X at 2.04 eV whereas the region marked (ii) has ΔE ≈ 22 meV with the spectral position of X at 2.065 eV. A change in the local electric field and the appearance of mirror charges in the metal will cause a Stark shift [24] of both X and X^*, but these shifts need not be identical, hence the varying ΔEs.

4.4.2 The Electromagnetic Model

The source of the fluorescence intensity enhancement can be explained through previous studies on surface-enhanced fluorescence and Raman scattering. Although many models persist in the literature, a leading contributor to the surface enhanced behavior is the electromagnetic model [25]. Simply, the rough corrugation of the surface is approximated by ellipsoids that scatter the incident electromagnetic field. A dipole near the surface of this ellipsoid interacts with both the incident and the scattered field; however, the coupling of the scattered field to the dipole can become much larger than the incident field when the dipole frequency is near resonance with the metal surface plasmon. Other factors such as the shape of the rough features lead to further enhancement, i.e. the lightning rod effect [26]. In the case of radiative dipoles (i.e. organic dye molecules or semiconductor nanocrystals), two competing factors determine the overall enhancement of the luminescence intensity [27]: increased absorption and emission due to the coupling of the radiative mode of the transition dipole with the metal plasmon, and non-radiative energy transfer from the excited dipole to the metal. We examine our observed enhancement factor in the context of this model. We define the

quantum yields for NCs coupled (Y) and uncoupled (Y_{free}) to the metal surface as follows:

$$Y = \frac{k_r}{k_r + k_{nr}} \quad (1a)$$

$$Y_{free} = \frac{k_{r\ free}}{k_{r\,free} + k_{nr\,free}} \quad (1b)$$

where k_r is the radiative rate and k_{nr} is the nonradiative rate for the nanocrystal. The excited state lifetime of the NC is $\tau = (k_r + k_{nr})^{-1}$. To take into account the increase in absorption, we relate the change in the intensities by an enhanced intensity factor γ,

$$\gamma = \frac{Y\sigma}{Y_{free}\sigma_{free}} \quad (2)$$

where σ is the effective absorption cross-section of the NC/metal system (σ_{free} is for the uncoupled NC). Finally, we make an order of magnitude approximation following Ref. [26] that assumes similar enhancements in cross-sections for both absorption and emission; $\frac{\sigma}{\sigma_{free}} = g(\omega_{ex}) \approx g(\omega_{fl})) = \frac{k_r}{k_{r\,free}}$ where $g(\omega)$ is the rate enhancement function, and ω_{ex} and ω_{fl} are the excitation and emission frequencies, respectively. By rearranging terms,

$$\frac{k_r}{k_{r\,free}} = \sqrt{\gamma \frac{\tau_{free}}{\tau}} \quad (3)$$

and

$$\frac{k_{nr}}{k_{nr\,free}} = \frac{\frac{\tau_{free}}{\tau} - Y_{free}\sqrt{\gamma\frac{\tau_{free}}{\tau}}}{1 - Y_{free}} \quad (4)$$

By applying the measured values $\gamma = 5$, $\tau_{free} = 150$ ns [20], $\tau = 130$ ps, and $Y_{free} = 0.3$, we obtain radiative rate and absorption cross-section enhancements of ~70 and a non-

radiative rate enhancement of ~1400. While the apparent quantum yield of the NC is lower in the surface enhanced system, the enhancement factors are large enough that we still see an overall increase in intensity. The linear polarization in the emission is also consistent with a surface coupled electromagnetic model that breaks the degeneracy in the symmetry of the free NCs. The linear polarization results primarily from the electric dipole polarization of the metal that couples to the NC radiation.

4.4.3 Beating the Auger Rate

Why do we observe emission from charged nanocrystals? The blinking of single NCs is due to an Auger relaxation process that competitively inhibits radiative relaxation when the NC is charged [28]. However, by increasing the non-radiative decay rate, the Auger rate (~147 ps for 2.8 nm radius at RT) [29] is no longer the rate-determining step in the excited state relaxation process. Despite the ~1400 fold increase in the non-radiative rate, the neutral and charged NCs both show emission due to the combination of an increased radiative and absorption rate; the only distinction for the charged emission is the shifting of the emission energy by the binding energy of the extra charge. According to calculations in ref. [22], the binary, discrete red shift in emission observed here is predicted to be similar whether it is an electron or hole that is involved in the charging process.

The observation of some room temperature blinking in NCs coupled to the gold substrate may be an indication of mobile NCs. That is, if the NC can move on the surface of the substrate, the distance and orientation of the NC on the metal substrate can change

in time, leading to significant changes in the decay rates. We have previously observed mobile NCs in trioctylphosphine-rich films that diffuse a few microns within one second.

4.5 Conclusion

Our results strongly suggest that we have observed emission from *charged* single CdSe(ZnS) NCs. The same mechanism for giant enhancements observed in surface enhanced Raman and surface enhanced fluorescence effects for molecular species are presented here in the context of single NC optical dynamics. By dramatically decreasing the NC lifetimes, the charged exciton relaxation has crossed over from non-emissive to emissive and allowed the identification of the charged exciton spectrum in single NCs.

4.6 Acknowledgements

The authors thank E. Barkai and D.J. Norris for insightful discussions.

4.7 References

1. R.R. Chance, A. Prock, and R.J. Silbey, Adv. Chem. Phys., 1978. **37**: p. 1.
2. M. Fleischmann, P.J. Hendra, and A.J. McQuillan, Chem. Phys. Lett., 1974. **26**: p. 163.
3. C.B. Murray, C.R. Kagan, and M.G. Bawendi, Ann. Rev. of Mat. Sci., 2000. **30**: p. 545.
4. K. Kneipp, Y. Wang, H. Kneipp, L.T. Perelman, I. Itzkan, R. Dasari, and M.S. Feld, Phys. Rev. Lett., 1997. **78**(9): p. 1667.
5. A.M. Michaels, M. Nirmal, and L.E. Brus, J. Am. Chem. Soc., 1999. **121**(43): p. 9932.
6. M. Nirmal, B.O. Dabbousi, M.G. Bawendi, J.J. Macklin, J.K. Trautman, T.D. Harris, and L.E. Brus, Nature, 1996. **383**(6603): p. 802.
7. A.L. Efros and M. Rosen, Phys. Rev. Lett., 1997. **78**(6): p. 1110.
8. M.D. Mason, G.M. Credo, K.D. Weston, and S.K. Buratto, Phys. Rev. Lett., 1998. **80**(24): p. 5405.
9. M. Sugisaki, H.W. Ren, K. Nishi, and Y. Masumoto, Phys. Rev. Lett., 2001. **86**(21): p. 4883.

10. S.A. Empedocles, D.J. Norris, and M.G. Bawendi, Phys. Rev. Lett., 1996. **77**(18): p. 3873.
11. C.B. Murray, D.J. Norris, and M.G. Bawendi, J. Am. Chem. Soc., 1993. **115**(19): p. 8706.
12. M.A. Hines and P. Guyot-Sionnest, J. Phys. Chem., 1996. **100**(2): p. 468.
13. B.O. Dabbousi, J. RodriguezViejo, F.V. Mikulec, J.R. Heine, H. Mattoussi, R. Ober, K.F. Jensen, and M.G. Bawendi, J. Phys. Chem. B, 1997. **101**(46): p. 9463.
14. R.G. Neuhauser, K.T. Shimizu, W. Woo, S.A. Empedocles, and M.G. Bawendi, Phys. Rev. Lett., 2000. **85**(15): p. 3301.
15. M. Kuno, D.P. Fromm, H.F. Hamann, A. Gallagher, and D.J. Nesbitt, J. Chem. Phys., 2000. **112**(7): p. 3117.
16. K.T. Shimizu, R.G. Neuhauser, C.A. Leatherdale, S.A. Empedocles, W.K. Woo, and M.G. Bawendi, Phys. Rev. B, 2001. **6320**(20): p. 5316.
17. A.L. Efros, Phys. Rev. B-Condensed Matter, 1992. **46**(12): p. 7448.
18. J.T. Hu, L.S. Li, W.D. Yang, L. Manna, L.W. Wang, and A.P. Alivisatos, Science, 2001. **292**(5524): p. 2060.
19. B. Lounis, H.A. Bechtel, D. Gerion, P. Alivisatos, and W.E. Moerner, Chem. Phys. Lett., 2000. **329**(5-6): p. 399.
20. M.G. Bawendi, P.J. Carroll, W.L. Wilson, and L.E. Brus, J. Chem. Phys., 1992. **96**(2): p. 946.
21. D.I. Chepic, A.L. Efros, A.I. Ekimov, M.G. Vanov, V.A. Kharchenko, I.A. Kudriavtsev, and T.V. Yazeva, J. Lumin., 1990. **47**(3): p. 113.
22. A. Franceschetti and A. Zunger, Phys. Rev. B, 2000. **62**(24): p. R16287.
23. Taking into account the increase in absorption cross-section, the NCs are being excited at a rate of ~8×10^7 excitations/second, with >10 ns between excitations on average. This is slow compared to the observed fluorescence decay time of ~130ps, excluding biexciton formation, which requires absorption of two photons before relaxation.
24. S.A. Empedocles and M.G. Bawendi, Science, 1997. **278**(5346): p. 2114.
25. M. Moskovits, Reviews of Modern Physics, 1985. **57**(3): p. 783.
26. J. Gersten and A. Nitzan, J. Chem. Phys., 1980. **73**(7): p. 3023.
27. A.M. Glass, P.F. Liao, J.G. Bergman, and D.H. Olson, Opt. Lett., 1980. **5**(9): p. 368.
28. It was initially speculated that the ionization process leading to a charged NC was itself the result of an Auger process requiring the creation of two electron-hole pairs (Ref. 6). It has since been argued, based on further experimental data, that such an Auger process is unlikely to be responsible for the initial ionization event (Ref. 16). The ionization process appears to be due to a tunneling event of charge back and forth between a delocalized state inside the NC and localized trap states outside the NC. This process does not require the creation of two electron-hole pairs or an Auger process. This allows the observation of charging even when the Auger rate is no longer competitive with other relaxation processes.
29. V.I. Klimov, A.A. Mikhailovsky, D.W. McBranch, C.A. Leatherdale, and M.G. Bawendi, Science, 2000. **287**(5455): p. 1011.

Chapter 5: Charging Nanocrystals

5.1 Introduction

Throughout the previous chapters, we continually suggest that a charged nanocrystal (NC) is the cause of fluorescence quenching resulting in blinking on the single NC level. Furthermore, drastic changes in the infrared and visible absorption as well as electrical properties are predicted for charged NCs[1]. Considering how widely applied transistors and field effect devices are in present-day computer chips[2], we approach charge injection of the NC core in a similarly device oriented manner. Recent results [3] observed charged NCs in solution phase by using an electrochemical approach. Although these electrochemical-charging experiments allowed for interesting intraband transition measurements, the solid-state, metal-insulator-semiconductor device has the advantage of easy miniaturization, scaled-up production, and sample robustness. In self-assembled quantum dots (QD), the addition and removal of electrons into the quantum-confined energy levels have opened up a realm of new electronic properties[4, 5]. However, these structures are in the weak quantum confinement regime compared to NCs and so the addition of extra charges has less impact on the quantum mechanical nature of these materials. Consequently, Auger processes in self-assembled QDs do not quench the fluorescence; rather, the spectra changes to reveal the charged and uncharged status of the QD.

In this chapter, we investigate electron (and hole) addition effects in close-packed films of colloidal NCs that exhibit strong quantum confinement properties, with organic ligands that facilitate NC film formation but also complicate charge mobility. To reduce this complication, the sample thickness was kept between 2~4 monolayers to provide

both a sacrificial first layer directly beside the metal electrode and to minimize the poor conductivity properties between adjacent NCs.

5.2 Experimental

Our device consists of an insulating polymer or a polycrystalline semiconductor layer and a thin, spin-coated NC layer sandwiched between two conducting electrodes shown in figure 5.1. In the first set of devices, we use a layer-by-layer deposition technique[6] to cast the polyelectrolytes poly(allylamine hydrochloride) (PAH) and poly(acrylic acid) (PAA) sequentially onto an indium-tin oxide (ITO) electrode. The resistivity of these PAH/PAA thin films (10^{12} Ω·cm)[7] is comparable to those of inorganic films. The PAH/PAA films are baked in a vacuum oven to create an amide cross-link between the NH_3^+ groups of PAH and the COO^- groups of PAA. This was significant to enhancing the film stability[8] and to reducing pin-hole currents through the insulator film. In the second set of devices, we employ a vapor-phase deposition technique called atomic layer deposition (ALD)[9]. In the ALD process, two gas-phase precursors (hydrogen sulfide and diethyl zinc) are flowed sequentially and exclusively through the reaction chamber and the sequence repeated for the number of layers required. The reactants interact only after the first layer has adsorbed onto the substrate and the reaction then occurs on an atomic layer basis. Because of the physical dipping process in the PAH/PAA films, the films cannot be deposited after the NCs are spin-cast. With the ZnS films, however, this limitation does not hold and we can deposit the insulating layer next to the metal, next to the ITO, or next to both and sandwich the NCs film in between two insulating ZnS layers. We tested bare CdSe and "core-shell" CdSe/ZnS

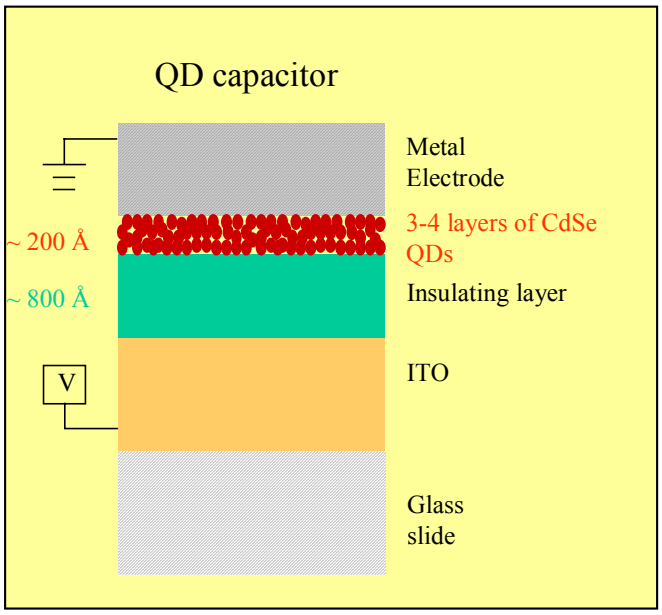

Figure 5.1: Device structure design. The insulating layer consists of 15.5 bilayers of PAH/PAA with the PAH layer on top or 200nm of a ZnS polycrystalline thin film. The ITO serves as a transparent electrode for photoluminescence measurements through an optical microscope. The excitation source consists of a CW Ar ion laser (514 nm, 50 W/cm^2) and the photoluminescence (PL) is detected by a CCD camera. Typical working pixel area is 6 mm^2 with eight pixels per device. The CdSe NCs were spin cast from toluene solution with absorbance of ~1 after 100X dilution at the first absorption peak.

NCs for a comparison in their charging behavior. Finally, a gold or aluminum electrode is deposited.

In all of our experiments, the metal electrode is grounded and the ITO electrode is connected to the applied voltage. By applying a sufficient electric field, the Fermi energy level of the aluminum/gold electrode aligns with the energy levels of the NCs and the charge carriers are injected into or extracted out of the NCs. The magnitude and direction of the applied field dictate the nature of the carriers (electrons or holes) and the charging process (injection or extraction).

5.3 Results and Discussion

5.3.1 Fluorescence Quenching

In figure 5.2, the relationship between the CdSe NC fluorescence and different applied voltages are shown. The field strengths used in the top and the bottom experiments are 3 x 10^5 V/cm and 4 x 10^5 V/cm, respectively. In our model, individual NCs arbitrarily turn *on* and *off*. However, for an ensemble that comprises of 100,000 NCs, an equilibrium between the *on* and *off* states exists and the ensemble fluorescence remains constant. Immediately after applying a positive voltage, we observe a fast drop in the fluorescence within the first 100 ms for both applied voltages. This initial darkening effect is most likely caused by field-assisted photoionization of carriers out of the NCs. These events not only impede the radiative recombination of the electron-hole pairs, but also leave NCs charged (dark). At low applied fields, the fluorescence either recovers for the polymer insulator device or remains constant for the ZnS insulator device. In order to inject electrons from the electrode into the NCs, the applied field (positive

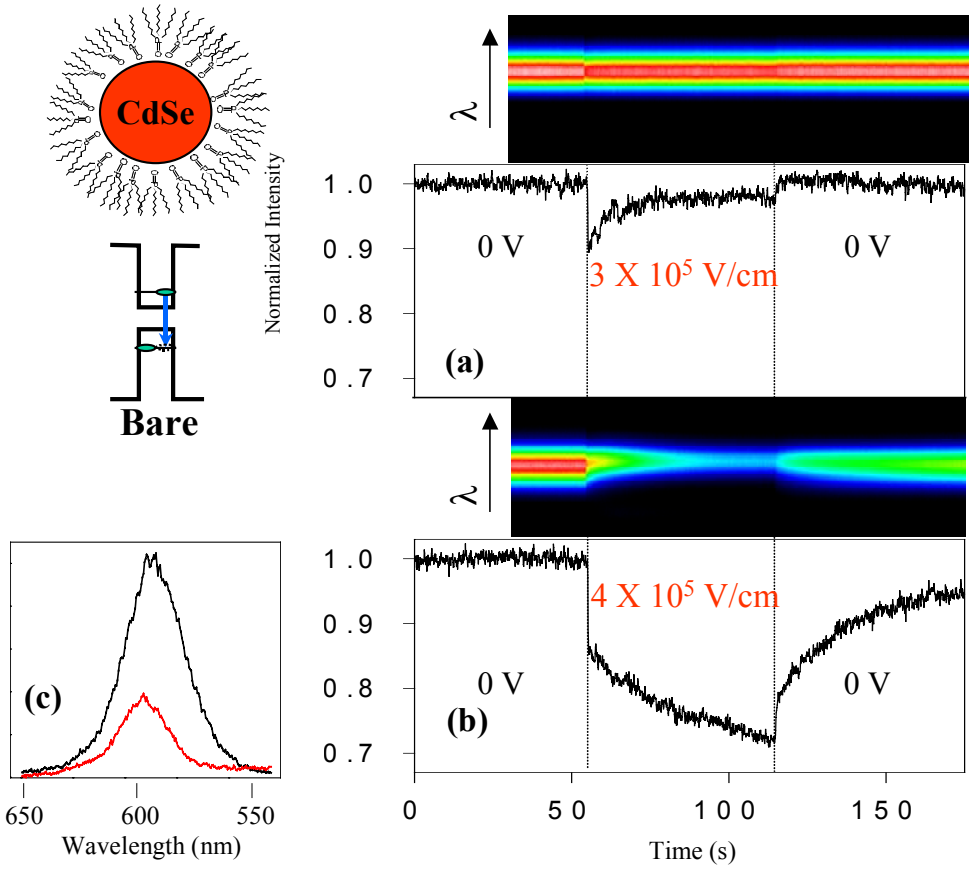

Figure 5.2: The charging time-traces for bare, 2.2 nm radius, CdSe NCs with an applied field of (a) 3 x 10^5 V/cm and (b) 4 x 10^5 V/cm. The corresponding spectral behavior is attached above. This shows that there is a slight spectral shifting to lower energy that accompanies the fluorescence quenching. (c) shows the extent of the spectral shifting which is much less than predicted for a purely Stark effect.

voltage) must raise the Fermi level of the metal above the lowest unoccupied energy level of the NCs. That is, we expect a critical voltage below which no injection is likely. Field strength of 3 x 10^5 V/cm is not sufficient to inject electrons from the electrode into the NCs, and the fluorescence quenching stops after the initial drop due to photoionization (figure 5.2). Although the fluorescence remains constant or recovers slowly in the presence of the applied voltage, the fluorescence fully recovers once the applied voltage is turned off.

5.3.2 Charge Injection

When the field strength exceeds 4 x 10^5 V/cm, injection of electrons occurs and the fluorescence is further quenched after the initial fast drop (figure 5.2b). As electrons migrate by a slow hopping[10] from charged NCs to uncharged ones, a slow decay in fluorescence results. After the voltage is turned off, the fluorescence shows an initial, fast recovery step and then gradually recovers completely. Clearly, there are differences between the charging and the discharging process. First, the magnitude of the initial recovery is considerably smaller than the magnitude of the initial fast drop induced by applying the voltage. Second, a complete discharging process (fluorescence fully recovered) usually takes more time than the charging process. One possible reason is that the surface states of the NCs are also being filled with electrons while the NCs are being charged. The number of vacant states for transporting electrons between the NCs and the electrode during the discharging process may be smaller than during the charging process. The discharging recovery time is usually on the order of seconds to a few minutes longer

than the charging time when the NCs are under continuous light excitation with no applied voltage (figure 5.2a) (the time depends on the degree of quenching).

5.3.3 ZnS Overcoated NCs

The effect of a ZnS overcoat on CdSe NCs at a given applied voltage can be observed when comparing figure 5.3 with figure 5.2. As the NCs are coated by a ZnS shell of ~1 nm thickness which forms a tunnel barrier for injection of electrons and holes into the CdSe core, the probability of injecting charges into the NC is significantly reduced. Our attempts to charge ZnS overcoated NCs and "bare" NCs using the same applied field clearly illustrate this. Although slightly diminished due to the overcoating, the applied field still assists the tunneling of photoexcited carriers from the NC cores to the core/shell interfaces and causes the initial drop in the fluorescence. However, the subsequent injection of electrons from the aluminum into the overcoated NCs fails unless an even higher field is applied. The critical field for the injection of electrons into the overcoated NCs is about 1.2 - 1.3 x 10^6 V/cm. The fluorescence of the overcoated NCs can be reversibly quenched to only 45% even when the applied field strength is as high as 2.2 x 10^6 V/cm (figure 5.3b). A relatively fast saturation is also observed. All these indicate an inefficient charging process and a dynamic competition between charge injection through the ZnS layer and photo-assisted discharging of core carriers into interface trap states.

5.3.4 Positive Bias

Figure 5.4 shows that holes can also be injected into the NCs at a sufficiently

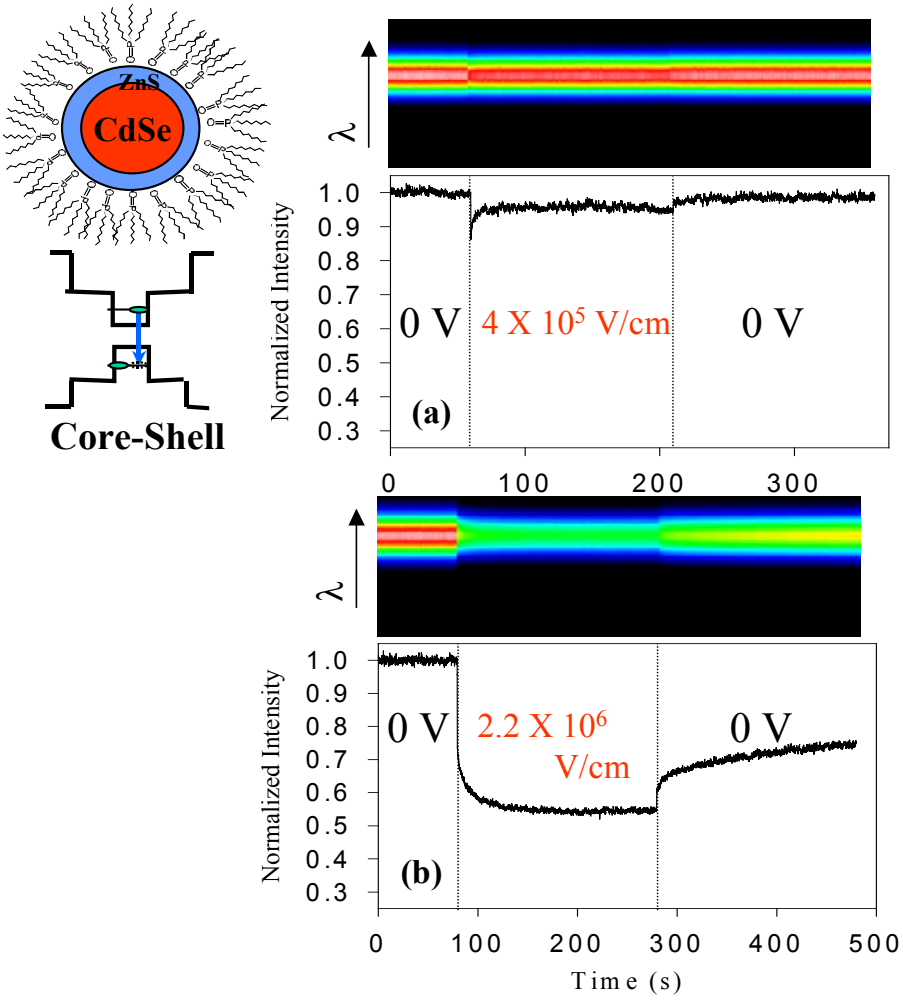

Figure 5.3: For ZnS overcoated NCs, the threshold for charge injection is higher than for the bare samples. The previous threshold of (a) 4 x 10^5 V/cm is insufficient to charge the overcoated NCs; charge injection is observed at (b) 2.2 x 10^6 V/cm. Furthermore, even at this elevated injection voltage, only 50% quenching is reached

large applied negative voltage. The separation between the highest occupied energy level of the NC and the Fermi level of aluminum is expected to be larger than the separation between the Fermi level and the lowest unoccupied energy level[11]. Thus, a larger field strength (1.3×10^6 V/cm) is necessary to initiate the hole injection process. The fluorescence in figure 5.2(b) and 5.4 does not fully recover between the voltage pulses as the recovery time is insufficient. In this device, the fluorescence recovers fully after approximately one minute following the end of the voltage cycling. This strongly indicates that hole-rich NCs are unchanged even after an "oxidation" process. As both electron-rich and hole-rich NCs can be readily prepared with the same device, we can also cycle the NCs between these two "oxidation" states.

5.3.5 Device Stability

For potential applications of these nanocrystal capacitor structures as optical modulators or in displays, the stability and the response times of the charging structure are important issues that are addressed in figure 5.5(a) and 5.5(b). As the device is cycled between zero and positive bias, the recovering fluorescence suggests that the charging/discharging process does not cause degradation to the NCs. Although the time frame in figure 5.5(a) is in the tens of seconds, the device can be operated at room temperature for tens of hours and similar stability has been demonstrated. In figure 5.5(b), a device operating below the critical voltage is shown. The fluorescence responds approximately as a step function with modulation of ~25% and both charging and

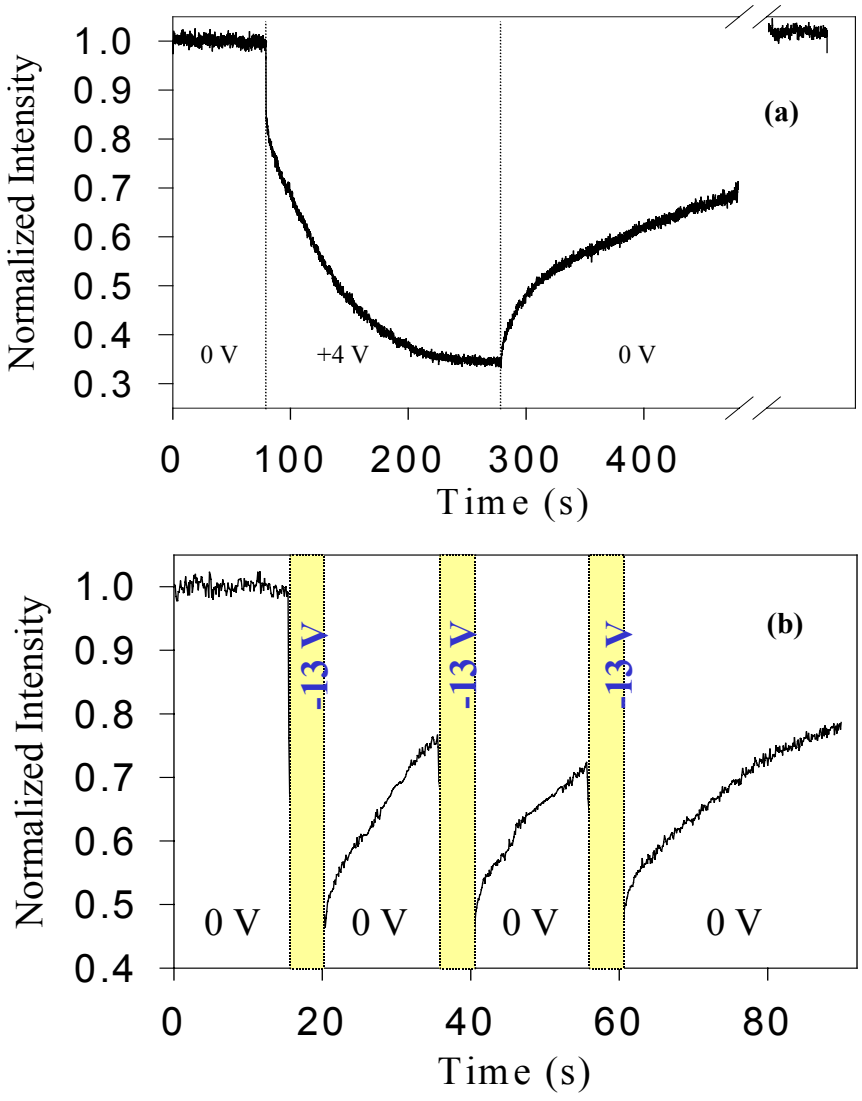

Figure 5.4(a): By sufficient charge injection, the PL is quenched by ~70% after 200 s. The PL recovery is complete after 400s at zero field. (b): Applying the appropriate negative voltage, hole injection also quenches the PL. Hole injection into the NC does not change the stability of the NCs or the device. The PL recovers completely after ~60 s.

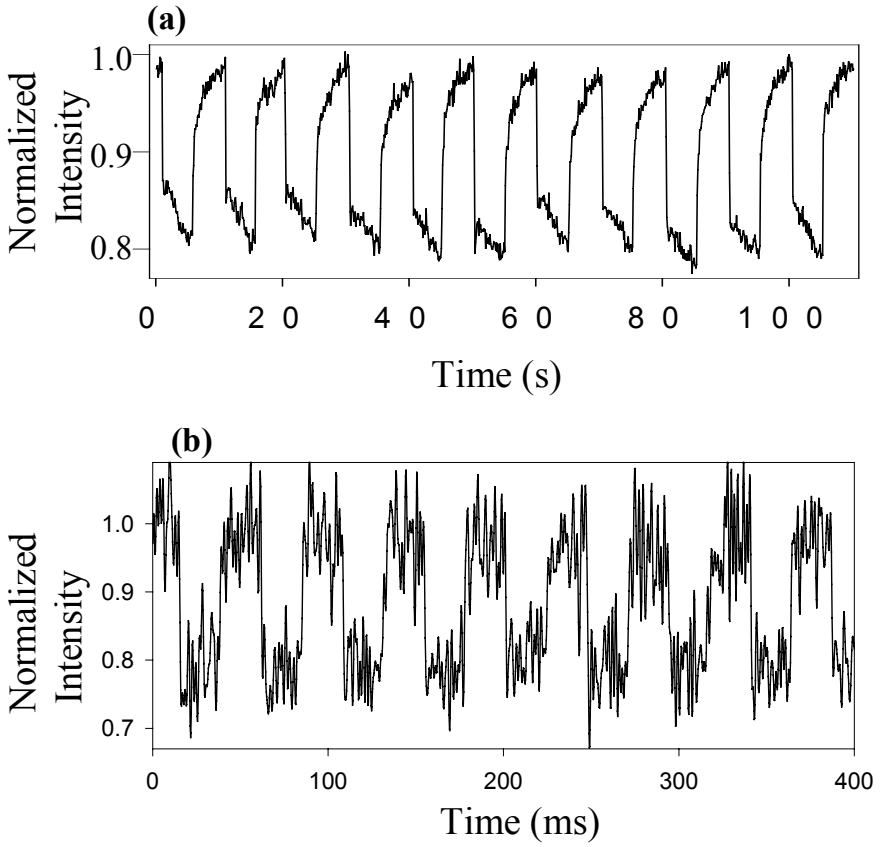

Figure 5.5(a): Photostability of the device is evidenced by the recovery of the photoluminescence intensity after the charge/discharge cycling of the voltage sequence. (b): Fast charging and discharging times of a CdSe(ZnS) NC charging device operating under the critical voltage.

discharging times are on the order of 100 μs.

The charging device can reversibly quench the fluorescence of the CdSe NCs up to ~65-75% (figure 5.2a). The possible reasons for the saturation are (1) a number of NCs are continuously discharged by Auger ionization of excitons generated by the excitation light, and (2) as more NCs are charged, this screens the remaining uncharged NCs and effectively makes the charging process more difficult. Consequently, a dynamic equilibrium is reached and the quenching saturates.

5.3.6 Polymer vs. ZnS insulating layer

The different insulating layers also showed interesting behaviors when combined with the NC charging film. For the polymer device below the threshold voltage, the fluorescence begins to slowly recover during the charging period as charge carriers migrate to screen the external field and the excitation light discharges the NCs through Auger processes. For the ZnS film device, however, the fluorescence does not recover but remains constant. Recent experiments have shown that the polymer may have electrostatic effects that can trap and release charged species. This results in other interesting photophysical differences. For example, a memory effect was present for the polymer PAH/PAA but not for the ZnS polycrystalline film: When the NC film in the polymer device was illuminated during the charging cycle, the zero-field intensity would differ depending on the bias (positive or negative) of the previous field applied. Both device structures still showed the slow quenching once the threshold voltage was reached.

Finally, the geometry of the device was changed to incorporate the NC adjacent to the ITO or with the insulating ZnS film on both sides of the NC film. The goal of these

modifications was to explore any effect dependent on the injecting electrode or to nullify the possibility to inject any charges from the electrodes altogether. For NCs placed next to the ITO electrode as compared to the aluminum electrode, the behavior was very similar. Unfortunately, for the case where insulator material was placed between the films, the data observed was inconclusive to whether the charge injection was primarily through the electrode or from NC ionization. When we increase the electric field to the injection threshold, the applied electric field had crossed beyond the breakdown potential of the insulator material itself. The increase in distance between electrodes due to the extra insulator material required a higher electric field to reach the same injection field. Upon surpassing the breakdown field, we observed similar slow fluorescence quenching.

5.3.7 Absorption Changes

The device also allows us to reversibly bleach the absorption of the CdSe NCs. Since the injected electrons should reside in the $1S_e$ state of the NCs, the probability of absorbing into this state from underlying hole states is reduced by half (figure 5.6a). If every NC has one excess electron, all transitions involving the $1S_e$ state should be bleached by 50%. The difference absorption spectra taken between the uncharged and charged state ($-\Delta OD$) is shown in figure 5.6(b). We can clearly see that all transitions involving the $1S_e$ state, shown in the solution absorption spectrum of the same NC sample, are bleached. Figure 5.6(c) shows the percentage-bleaching time trace of the $1S_{3/2}1S_e$ transition; the reversible bleaching is as much as 40%. The results also illustrate the absence of a Stark effect, as a red-shifted induced absorption peak does not exist[12, 13].

Ideally, fluorescence and absorption ($1S_e$ state) of a charged NC should be 100%

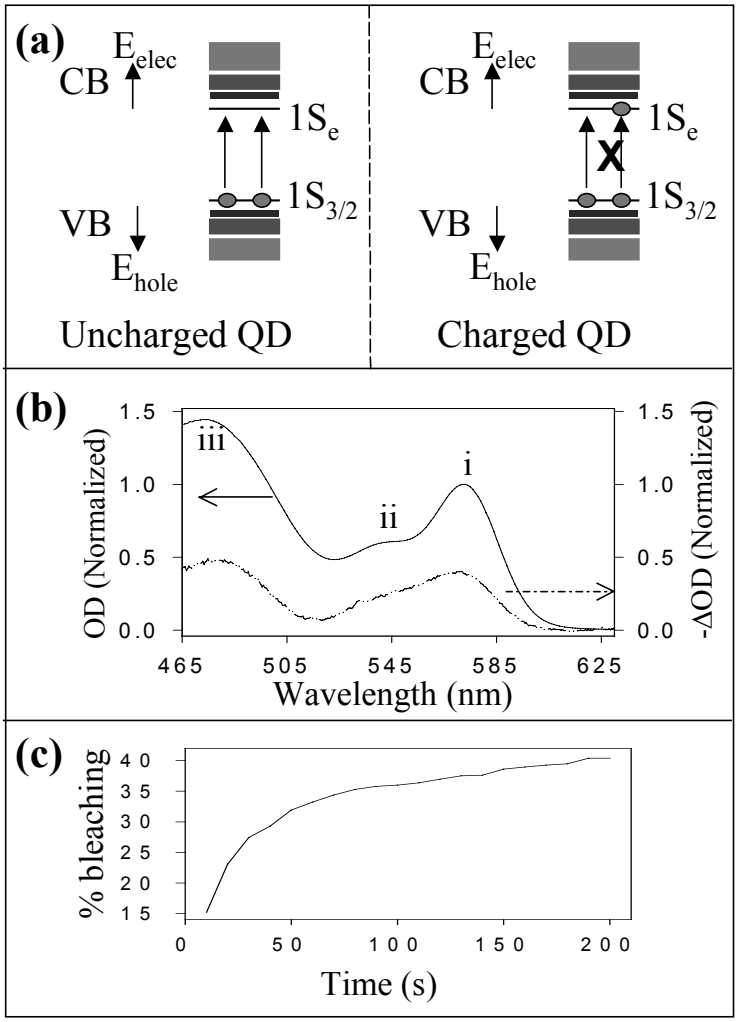

Figure 5.6: Absorption bleaching in charged NCs. (a): The electronic energy model predicts a ~50% decrease in the probability to absorb a photon for a charged NC since the lowest electron energy level follows the Pauli exclusion principle. (b): The upper spectrum (solid line) shows the absorption spectrum from a solution of the NCs making up the film. The lower spectrum (dashed line) is the difference spectrum for absorption [-ΔOD = OD(neutral) - OD(charged)] taken from the NC charging device. Specific electronic transitions to the ground state (i) $1S_{3/2}1S_e$, (ii) $2S_{3/2}1S_e$, (iii) $2S_{1/2}1S_e$ are labeled accordingly. (c): The time dependent change in the percentage bleaching of the $1S_{3/2}1S_e$ state is shown to saturate near a maximum of 40%.

quenched and 50% bleached, respectively. However, the experimental results (fluorescence quenching followed by absorption bleaching measurements or vice versa on the same sample) show that the magnitude of the fluorescence quenching generally falls short (within 20%) of the expected value compared to the bleach of the absorption. This may be attributed to our experimental conditions, where the higher excitation intensities and shorter wavelengths enhance the discharging rate during fluorescence quenching experiments, with the result that the number of charged NCs in our fluorescence quenching experiments may be slightly smaller than in the absorption bleaching studies.

5.4 Future Studies

In the immediate future, low temperature and NC size dependent measurements may provide further details and more accurate measure of the energy scales in the charge and field-induced mechanisms. However, the ultimate goal is to reach the single NC limit. By reaching this limit, we can determine whether the photoluminescence from a population of single NCs is quenched or if every NC has diminished in fluorescence by a given percentage. Our initial attempts have been hampered by device limitations: First, any NCs placed < 5 nm away from the metal electrode will quench due to image dipole energy transfer. Second, the glass substrate of our device contains too many impurities to observe single NC emission. The most likely solution is to use thin cover slide substrates with ITO sputtered on top. To alleviate the problem with the metal electrode, we can incorporate NCs of one size as dopants into a film of smaller size (higher band gap) NCs.

In this manner, single NC photophysics can be monitored keeping the general device design unchanged.

5.5 Conclusion

In summary, we have fabricated simple, stable, solid-state devices that can reversibly charge multiple layers of NCs at room temperature. The drastic changes in the optical properties lead to the possibility of using NCs in optical modulators and in tunable fluorescent or photochromic displays. Further improvements, such as decreasing the NC layer thickness, the device size, and improving conduction through the nanocrystals by engineering the organic ligands, should shorten both charging and discharging times. Additionally these structures should also allow systematic studies of the photophysics of charged NCs.

5.6 References:

1. A. Franceschetti and A. Zunger, Physical Review B, 2000. **62**(24): p. R16287.
2. D. GoldhaberGordon, M.S. Montemerlo, J.C. Love, G.J. Opiteck, and J.C. Ellenbogen, Proceedings of the Ieee, 1997. **85**(4): p. 521.
3. C.J. Wang, M. Shim, and P. Guyot-Sionnest, Science, 2001. **291**(5512): p. 2390.
4. M. Bayer, G. Ortner, O. Stern, A. Kuther, A.A. Gorbunov, A. Forchel, P. Hawrylak, S. Fafard, K. Hinzer, T.L. Reinecke, S.N. Walck, J.P. Reithmaier, F. Klopf, and F. Schafer, Physical Review B, 2002. **65**(19): p. art. no.195315.
5. K.H. Schmidt, G. Medeiros-Ribeiro, and P.M. Petroff, Physical Review B, 1998. **58**(7): p. 3597.
6. G. Decher, Science, 1997. **277**(5330): p. 1232.
7. M.F. Durstock, Thesis, Massachusetts Institute of Technlogy, 1999.
8. J.J. Harris, P.M. DeRose, and M.L. Bruening, Journal of the American Chemical Society, 1999. **121**(9): p. 1978.
9. G. Stuyven, P. De Visschere, A. Hikavyy, and K. Neyts, Journal of Crystal Growth, 2002. **234**(4): p. 690.
10. C.A. Leatherdale, C.R. Kagan, M.A. Kastner, and M.G. Bawendi, Abstracts of Papers of the American Chemical Society, 1997. **213**: p. 319.

11. H. Mattoussi, L.H. Radzilowski, B.O. Dabbousi, E.L. Thomas, M.G. Bawendi, and M.F. Rubner, Journal of Applied Physics, 1998. **83**(12): p. 7965.
12. V.L. Colvin, K.L. Cunningham, and A.P. Alivisatos, Journal of Chemical Physics, 1994. **101**(8): p. 7122.
13. A. Sacra, D.J. Norris, C.B. Murray, and M.G. Bawendi, Journal of Chemical Physics, 1995. **103**(13): p. 5236.

Chapter 6: Single Nanocrystal Zeeman Spectroscopy

6.1 Introduction

Magnetic perturbations of semiconductor materials have emerging prospects in areas such as "spintronics"[1], where the motion of electrons depends on the spin angular momentum of the electron. The possibilities for controlling the electronic behavior in semiconductors through magnetic interactions are still in their early development. However, the use of quantum-confined structures enables a more thorough investigation of the properties of the spin degree of freedom by changing the density of electronic states and phonon coupled relaxation of the electronic states, the latter leading to decoherence of the electron spin polarization. In addition to answering fundamental physics questions, the manipulation of spin states has potential for technological impact in areas of memory storage as well as computation by using spin-valve transistors that modulate electrical current based on spin[2].

Although investigations of the intrinsic electron spin properties of low dimensional structures have been previously performed in self-assembled quantum dots[3-5], the same behavior in nanocrystals (NC) or colloidal quantum dots derived from wet chemical synthesis procedures have yet to be as conclusive[6, 7]. Some early reports have shown great potential for exploring fundamental spin physics in semiconductor NCs[8, 9]. However, the primary impediment lies in the intrinsic particle size inhomogeniety and the random orientation of the NCs' crystalline axes in densely packed films. In our attempt to overcome this barrier, we report magnetic field dependent optical polarization and spectral behavior of single CdSe(ZnS) nanocrystals. The emission polarization anisotropy and the spectral data demonstrate the lifting of the electron spin

degeneracy when a magnetic field is applied parallel to the crystalline axis orientation. Surprisingly, we also observe an unexpected spin splitting in a small number of NCs with no external magnetic field.

6.2 Experimental

We incorporated a far-field photoluminescence microscope into the bore of a superconducting magnet (Janis Research) in the Faraday geometry (optical axis parallel to the applied magnetic field, see figure 6.1a). A 40X UV-grade fused silica air objective (Partec GmbH N.A.=0.7) was immersed with the sample manipulator into the liquid helium flow-through magneto-cryostat. Images focus was maintained down to 3.3K, however, most experiments were performed between 6 K and 15 K. The 514 nm line of the Ar ion CW laser supplied laser illumination to the sample. Sample excitation and emission collection was conducted through quartz and fused silica windows at the base of the magnet and a suitable dichroic or 90% reflective mirror guided the light into the spectrometer. A schematic of the optical layout is shown in figure 6.1(b). In step (i) and (ii), the 45^{o} linear polarization rotator and the polarization beam splitter are used to decipher the NC 3-D orientation. In step (iii), a suitable quarter waveplate and the polarization beam splitter help to elucidate the circular polarization dependence to measure the splitting of the spin-degenerate energy levels. As shown in figure 1(a), the orientation of the NC sample can be described by the angle, θ, between the c-axis and optical axis. The spectral data were acquired using a 550 mm single monochrometer and a thermo-electrically cooled CCD camera (Roper Scientific MicroMax). This spectrometer achieved spectral resolution on the order of ~70 μeV with the 1800 gr/mm

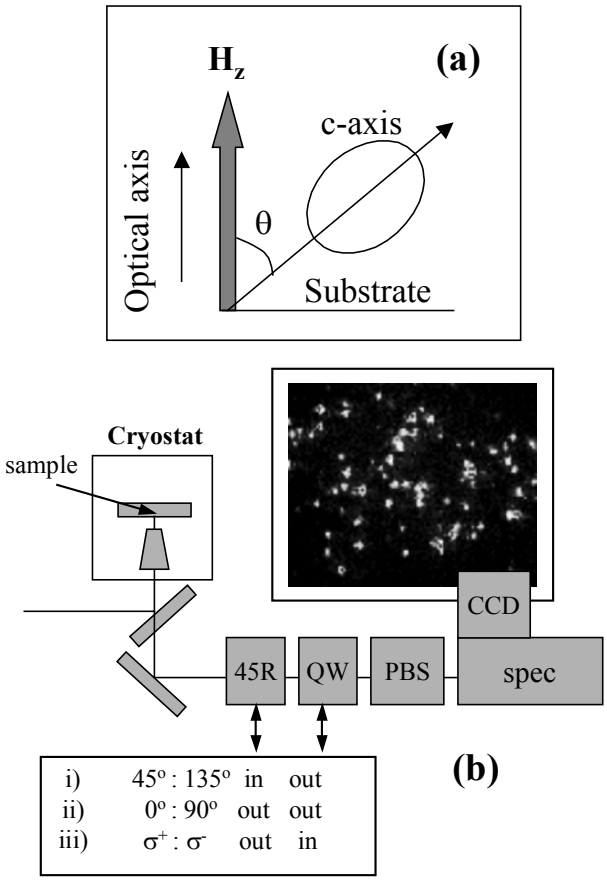

Figure 6.1(a): Orientation of the NC c-axis is described by the out of plane angle, θ, relative to the magnetic field, H_z, and optical axis. (b): Schematic of the optical layout for magneto-optic microscopy. Both the sample and microscope objective are placed in the cryostat assembly. The combination of the linear polarization rotator (45R) and the polarization beam splitter (PBS) aid in determining the NC 3-D orientation and the quarter waveplate (QW) and the PBS combination allow for characterization of the circular polarized nature of the NC emission. Inset shows a typical image acquired onto the CCD camera with 2 sec integration time. Laser excitation intensity was limited to <10mW entering the base of the cryostat.

grating. The single CdSe/ZnS nanocrystals were spin-cast onto a crystalline quartz substrate in a polymer matrix of polymethyl-methacrylate (PMMA). Translational drifts in the sample position usually accompanied data sets taken during a magnetic field ramp from 0 to 10 T. In order to follow the same individual NCs, software correction was used to track these drifts. The core-shell CdSe/ZnS nanocrystals were synthesized following previously published methods[10-12].

6.3 Results

The inset of figure 6.1(b) shows fluorescence images from single NCs inside the magnet cryostat. Each spot represents emission from an individual NC with each spaced 2~3 μm apart. Although optical detection of single chromophores has been performed previously[13], the incorporation of the primary focusing lens inside a cryostat required changes from our past microscope design. In particular, we use a non-magnetic, air-spaced objective to adequately collect light independent of the cryostat temperature (3 K ~ 300 K). Earlier attempts using conventional microscope objectives with aspheric doublet lenses resulted in background fluorescence from the adhesive material binding the optical elements and light collection efficiency loss at low temperatures. Ubiquitous to single NC spectroscopy, we still observe blinking and spectral diffusion behaviors that have been well documented in single NC optical measurements[13, 14]. Inevitably, this complicates the experimental results because extraneous peaks may appear and disappear due to the spectral/intensity fluctuations during a single acquisition scan. When interpreting the data, these dynamic artifacts were distinguished from the true spin-

dependent behaviors. Moreover, we minimized the influence of these extrinsic effects by reducing both the laser intensity and integration time.

In figure 6.2(a), we show typical single NC polarization data where the NC emission is separated into two according to its circular (or linear) polarization and imaged onto the CCD detector. The double headed arrows point to corresponding images that originated from the same NC. In figure 6.2(b), we plot the distribution of polarization anisotropy values, $P_{A,\sigma,}$

$$P_{A,\sigma} = \frac{I_{\sigma}^{-} - I_{\sigma}^{+}}{I_{\sigma}^{-} + I_{\sigma}^{+}} \quad (1)$$

where I_{σ}^{+} and I_{σ}^{-} are the intensities of right and left circularly polarized light, respectively, for a set of 50 single NCs as the magnetic field is increased from 0 to 10 T. These NCs were spin-cast in a polymer matrix and are assumed to be randomly oriented relative to the applied field. In figure 6.2(c), we track the mean value in the distribution of polarization anisotropies as a function of applied magnetic field. We observe a linear relationship between the magnetic field and the change in the anisotropy with a slope of 3% per Tesla. This linear dependence and the maximum 30% change is consistent with previous reports on ensemble CdSe NCs[7]. However, unlike the ensemble experiments, we observe a distribution of behaviors and some anisotropy values reach 50%[15]. To investigate further into the single NC Zeeman effects, figure 6.3(a) displays a single NC intensity time trace for right and left circularly polarized light as a function of magnetic field. While the magnetic field ramped from 0 to 10 T over a 15-minute span, we acquired an intensity trace of 180 frames, as shown in figure 6.3(b), to observe the Zeeman splitting behavior on an individual NC basis. Blinking effects on the single NC

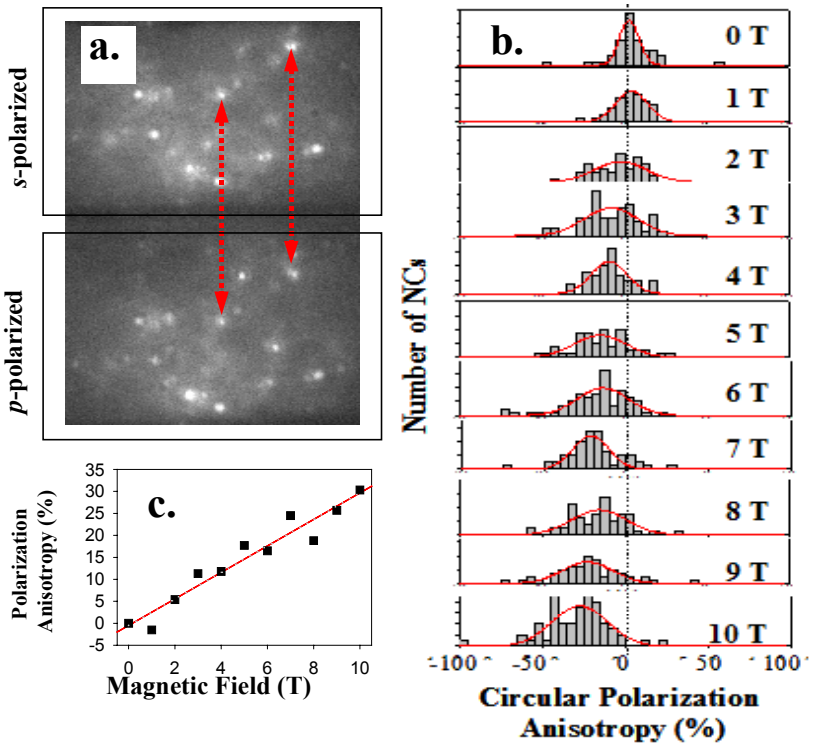

Figure 6.2(a): Typical images of the polarization-resolved NCs. The arrows help to identify the same NCs in the *s*- (σ^+) polarized and *p*- (σ^-) polarized sections. 5 s integration time with 5 mW excitation intensity into the microscope objective. (b) Histogram of single NC circular polarization anisotropy values at 10 K as the field is increased from 0 to 10 T. (c) Mean position of the Gaussian fitting of the plots in (b).

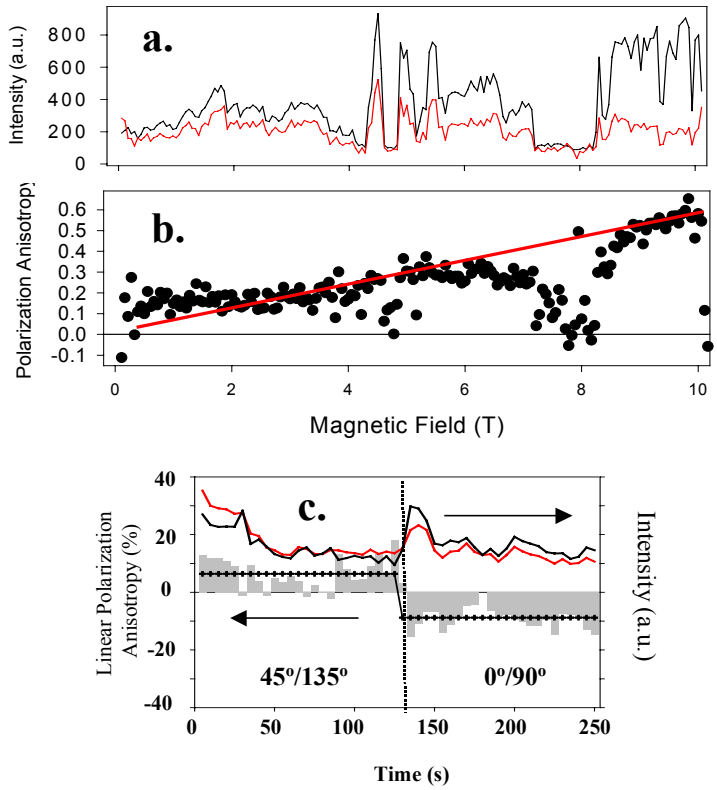

Figure 6.3(a): Intensity time trace of the σ^+ polarized (red line) and σ^- polarized (black line) emission as the magnetic field is increased. (b) The circular polarization anisotropy time trace for the same NC. (c) The linear polarization intensity and corresponding linear polarization anisotropy time trace for the same NC just prior to magnetic field measurements. The first 130 s measure the 45° and 135° linear polarization intensity and the next 130 s measure the 0° and 90° linear polarization intensity values.

level can reduce the overall signal and lead to sudden jumps in the $P_{A,\sigma}$ values, but the overall trend is easily captured by the polarization intensity-time trace. Just before the magnetic field is applied, we also attained information regarding its 3-D orientation through linear polarization measurements at 0^o, 45^o, 90^o, and 135^o angles (figure 6.3(c)). The ratios of these linear anisotropy values (0^o:90^o and 45^o:135^o**)** can be extrapolated to give the longitudinal and latitudinal orientation of the c-axis[16]. In figure 6.4, we take data from 70 NCs to illustrate the relationship between 3-D crystal orientation and magnetic field perturbation effects. While the change in $P_{A,\sigma}$ shows no dependence on the in-plane angle, there is a clear trend for the out-of-plane angle. Specifically, we see that the NCs with smaller out-of-plane angles (i.e. more parallel to the magnetic field) correspond to NCs with higher circular polarization changes indicative of larger Zeeman splitting of the emitting states. The red (blue) line drawn in figure 6.4(b) and (c) follows the theoretical fit for the population of the spin states following a Boltzmann distribution and angular-dependent Zeeman splitting[7]. The predicted polarized intensities follow:

$$I_{\sigma\pm}(\theta) = \frac{\left[(1 \mp \cos(\theta))^2 e^{\Delta\beta/2} + (1 \pm \cos(\theta))^2 e^{-\Delta\beta/2}\right]}{\left[e^{\Delta\beta/2} + e^{-\Delta\beta/2}\right]} \qquad (2)$$

where $\Delta = g_{ex}\mu_B H\cos(\theta)$ and $\beta = (k_B T)^{-1}$. We use values of g_{ex} = 3.6 (red) and 1.3 (blue) from our spectral results and ref[7], respectively, for T = 6 K. The higher density of data points near 0^o and 180^o in figure 6.4(b) results from the uncertainty in extrapolating orientation angles from anisotropy values. The 90% reflective mirror used may have also introduced a slight preferential polarization along the vertical (0^o) direction leading to data points skewed towards 0^o and 180^o.

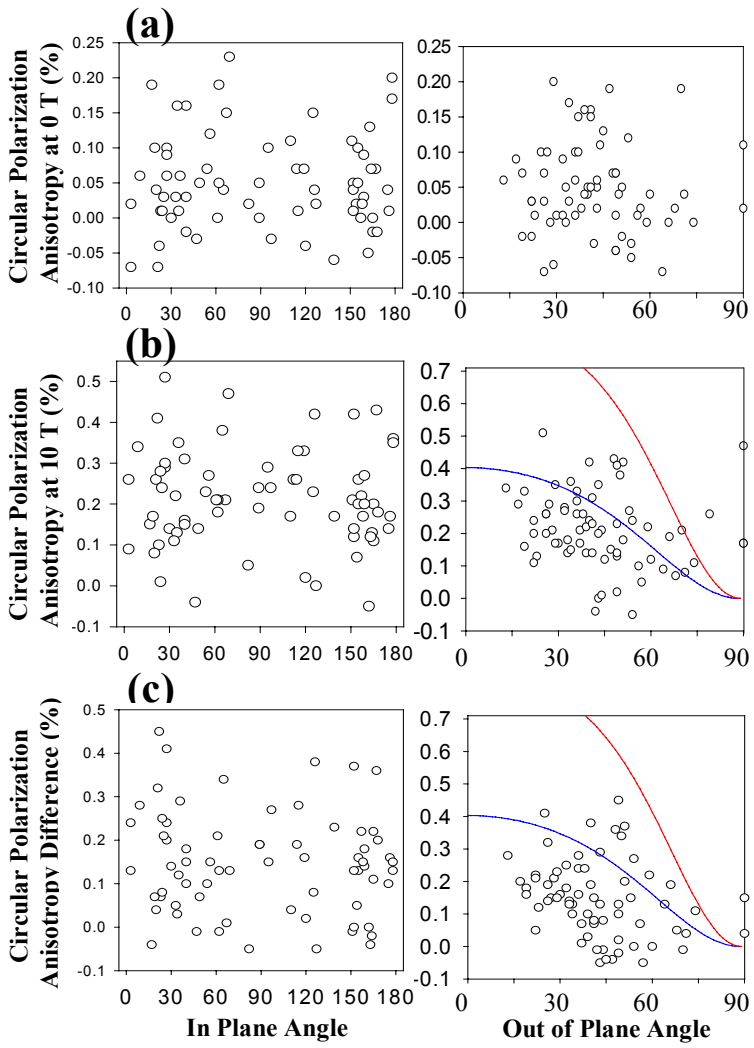

Figure 6.4: Circular polarization anisotropy values plotted against the NC in-plane and out-of-plane orientations for 70 NCs at 6 K with (a) no magnetic field applied and (b) 10 T applied. (c) The change in the circular polarization anisotropy from 0 to 10 T is plotted against the NC orientation. The NCs data was acquired as outlined in figure 3. The red (blue) curve is a theoretical behavior following a Boltzmann distribution for g_{ex} = 3.6 (1.3)

In Figure 6.5(a) and 6.5(b), we show the Zeeman-split spectra from two different single CdSe nanocrystal at 10 T. The splitting observed over several NCs are constant with time and the magnitude of the separation ranged from 1.1 meV to as high as 2.2 meV. The spectra are followed for 10 frames with 25 s integration times and typical spectral linewidths of the NC emission did not allow for identification of Zeeman splitting less than ~1 meV apart. Although the data show the expected spectral diffusion, the magnitude of the peak separation remains constant. Spectral diffusion effects can produce false positive results if a single peak were to jump during one acquisition scan to create an artificial doublet. However, when we observe the spectral doublet shift together throughout multiple acquisitions, this supports the view that the doublet is due to an interaction with the applied magnetic field.

In Figure 6.6(a), we observe a very surprising result. In the absence of any external magnetic field, a single NC spectrum is collected and isolated based on the direction of the circular polarization emission. When the σ^- and σ^+ polarization spectra are overlaid, the data shows clear splitting for a single CdSe NC; the two peaks emitting with opposite circular polarization. The observed zero field splitting in this example is ~1.1 meV. The frequency of this observation was less than 15%; however, an accurate statistical analysis is made difficult by the spectral and blinking dynamics. These dynamics blur spectra and diminish the true number of NCs with zero field spin splitting. Also, since the random distribution of NC orientations limits the number of NCs that emit circularly polarized light in the direction of optical collection, we cannot verify whether two emission peaks originate from oppositely polarized spin-states. In figure 6.6(b), we turn on the magnetic field and monitor the polarization-resolved spectra as a function of

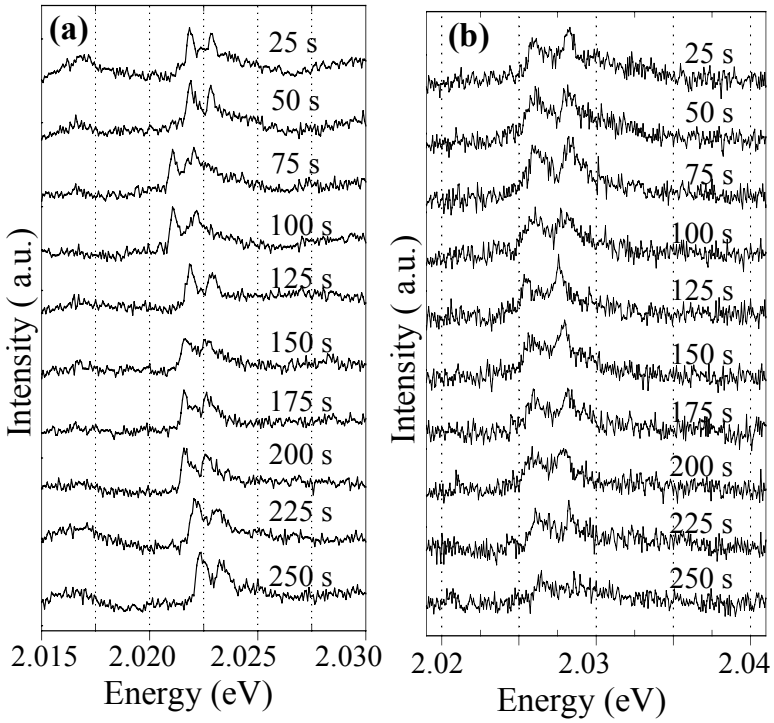

Figure 6.5: Single NC spectra for two different NCs: (a) NC # 1 and (b) NC # 2 taken with 25 sec integration times at 13 K. The offset peaks represent 10 consecutive frames at 10 T. Small spectral diffusion shifts show that the mean position of the peaks moves, but the separation between the peaks remain constant.

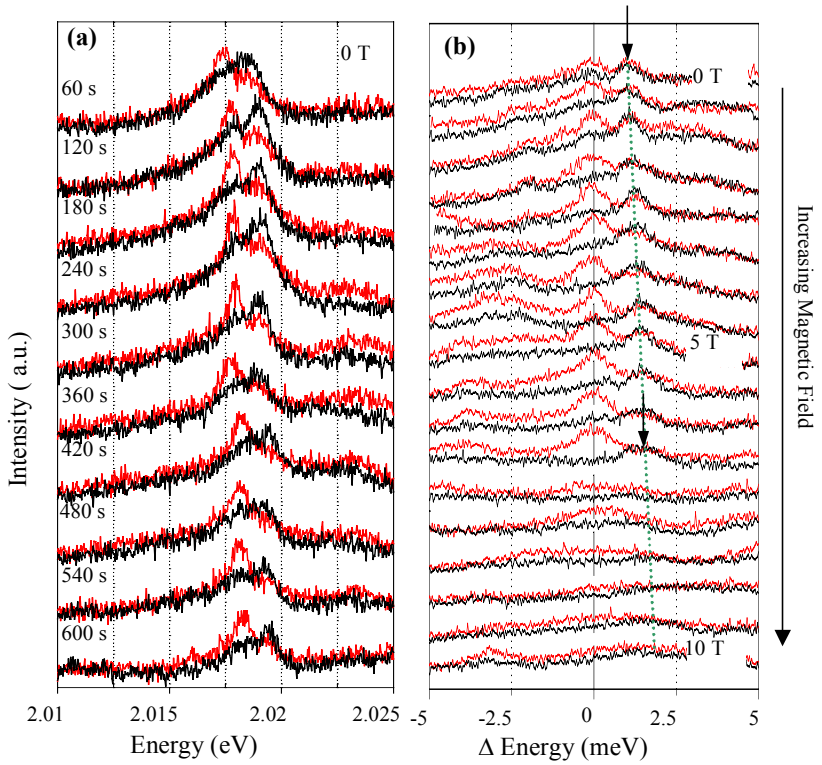

Figure 6.6(a): Polarization-resolved single NC spectra taken at 0 T and 11 K. The spectra were separated based on the right (black plot) and left (red plot) circular polarization. Clear polarization dependence to the zero-field splitting is present. (b) Polarization-resolved single NC spectra where the magnetic field is increased from 0 to 10 T. In this series, the peak position of the black plot was centered to show the increasing peak separation of the red plot as the field is increased. Note that this NC also shows zero-field splitting and that the split peaks are susceptible to magnetic fields. Near 7 T, the NC has either spectrally shifted outside of our detector range or simply turned off.

time. At frame 1, there is no field applied, and we already observe polarized, spectral splitting. As the magnetic field increases, the magnitude of the splitting also increases. At frame 13, the NC has blinked off, and the spectra can no longer be followed.

6.4 Discussion

Single molecule measurements, as presented here, have clearly shown that the ensemble averaging over different sizes and different orientations is no longer a barrier that hinders the inspection of NC magneto-optical properties; however, we still contend with optical dynamic effects and a distribution of NC orientations.

6.4.1 The Exciton Fine Structure

Figure 6.7 is a schematic of the electron-hole energy level diagram and the transitions that dictate the band-edge emission taking into consideration the nanocrystal shape anisotropy, unit cell hexagonal crystalline structure, and the electron-hole exchange interaction[17]. The fine structure of the band edge consists of five energy levels that are labeled by their total angular momentum, F. In the exciton total angular momentum basis set, the lowest energy states, $F = \pm 2^L$, are optically forbidden and the lowest optically active states are $F = \pm 1^L$. Evidence from previous experiments has shown that emission from the $\pm 2^L$ states is possible and explains the fluorescence Stokes shift and μs scale excited state lifetimes. The symmetry for the transition from the $F = \pm 2^L$ (if spin-flip assisted) and $\pm 1^L$ states to the ground state allows for circular polarized light emission and for the sign of the polarization to determine the emitting state. Regardless of the total angular momentum number, the splitting of these |+> and |–> lowest excited states should

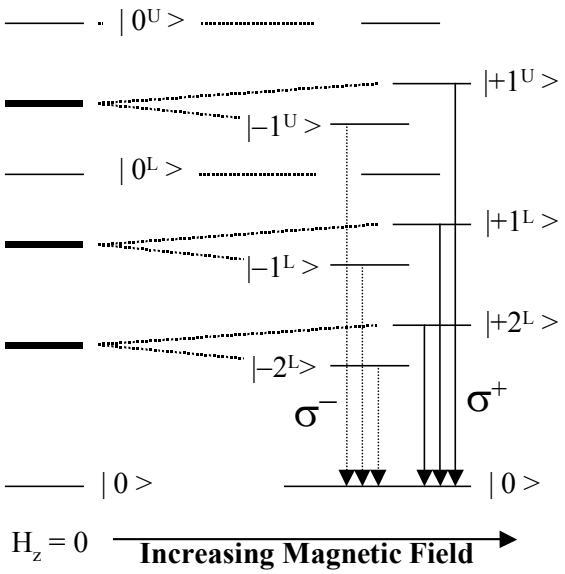

Figure 6.7: An energy level diagram of the $1S_e1S_{3/2}$ fine structure states and the predicted perturbations for an external magnetic field applied parallel to the hexagonal crystal axis.

result in spectrally observable doublet peaks and a change in the detected emission polarization from non-polarized to circularly polarized.

6.4.2 Molecular Zeeman Effect

Previous experiments to measure the g-factor were based on magnetic circular dichroism measurements on the absorption into the entire $1S_e1S_{3/2}$ state and ensemble emission polarization measurements that relied purely on polarization intensity values. Both cases involved averaging over the sample orientation and size distribution. The molecular Zeeman effect is described by

$$H_H = \frac{1}{2} g_e \mu_B \, \sigma \, \mathrm{H} - g_h \, \mu_B \, \kappa \, \mathrm{H} \qquad (3)$$

where g_e (g_h) are the electron (hole) g factors, H is the magnetic field, σ is the Pauli Spin matrix, κ is the hole angular momentum operator, and μ_B is the Bohr magneton. The analysis of the Zeeman splitting neglects higher order terms in H (i.e. diamagnetic effects) because the NC is smaller than the magnetic characteristic length of ~ 110 Å at 10 T. Following the work in ref [17], the energy splitting for an applied magnetic field parallel to the NC c-axis is:

$$\Delta \mathrm{E}_{(F=-2\rightarrow+2)} = \mu_B \, H_z (g_e - 3g_h) \cos(\theta) \qquad (4a)$$

$$\Delta \mathrm{E}_{(F=-1\rightarrow+1)} = \mu_B \, H_z \left[g_e \left(\frac{\pm f}{\sqrt{f^2 + d}} \right) - g_h \left(\frac{2\sqrt{f^2 + d} \mp f}{\sqrt{f^2 + d}} \right) \right] \cos(\theta) \qquad (4b)$$

where f and d are functions related to the electron-hole exchange interaction and asymmetry of the nanocrystal (see Eq. (21) in ref. [17]) and θ is the angle between the magnetic field direction and the c-axis of the NC unit cell. Consistent with a variety of

NC orientations, we observe a distribution of the doublet peak separations. We could not directly correlate the magnitude of the Zeeman splitting to the NC orientation relative to the applied field. The long integration times (60 s) for polarization-resolved spectra acquisition combined with spectral and intensity fluctuations make these assignments very difficult. Comparing the theoretical predictions to the experimental data, we can apply the calculated g_e and g_h values of 0.68 and –1.09, respectively to equation 2 and 3. This corresponds to Zeeman splitting of 2.29 meV and 1.50 meV for the $\pm 2^L$ and $\pm 1^L$ states, respectively, at 10 T. The magnitude of the largest observed peak splitting was 2.1 meV and this corresponds better to the $\pm 2^L$ state for a NC with hexagonal crystal axis nearly parallel to the applied field. Indeed, we would expect the emission to occur primarily from the $\pm 2^L$ state at these low temperatures.

6.4.3 Correlation Between NC Orientation and Magnetic Field

The symmetry of the CdSe NC shape and crystal structure gives rise to a doubly degenerate emitting state with a disk-shaped emission polarization [18]. This has allowed us to probe the orientation of single NCs with respect to the laboratory frame of reference [19]. These 2-D emission dipole signatures include the statistical variation in the degree of polarization (0 to 100%) for a randomly oriented sample. That is, single dipole emitters such as single dye molecules have linear dipoles that can be completely filtered by a linear polarizer rotated orthogonal to the incoming polarization. On the other hand, depending on the 3-D orientation, a circular emitter such as CdSe NCs may have both emitting dipoles in the plane such that the light cannot be completely filtered, regardless of the linear polarizer angle. For example, the detection of linearly polarized

light corresponds to a NC with its c-axis perpendicular to the optical axis and applied field. In these particles, we expect no splitting of the degenerate spin states and hence, no change in the emission circular polarization when an external magnetic field is applied. However, for particles with the c-axis parallel to the optical axis, we expect an increase in the spin splitting and in the +2 and –2 state populations ($k_BT \approx 0.52$ meV at 6 K) with increasing applied magnetic field. This should cause emission of preferentially left circularly polarized light. The data in figure 6.4 indeed shows the out of plane dependence and the in plane angle independence consistent with the picture above. Although the trend is visible, the fit to the theoretical curve is rather poor when we use the theoretical g_{ex} value. Polarized background fluorescence or laser light may be one reason. There may be another more interesting explanation. The authors in ref [7] reported temperature dependent g values for the exciton. This type of behavior observed in dilute magnetic semiconductors is not included in the theoretical model. If we were to apply the temperature adjusted g-factor of 0.97 then the theoretical curve fits much better with our experimental results. The spectra were taken at >10 K in part because the appearance Zeeman split spectra were more frequently observed at these temperatures. This may also be explained by a temperature dependent g-factor. As the g-factor decreases faster than the inhomogeneous emission linewidth (due to spectral diffusion) changes for lower temperatures, this would reduce the chances of observing spin-split emission spectra. A careful temperature analysis is required to determine the exact temperature dependence of the g-factor on individual NCs. Qualitatively, we validate the theoretical models that (i) describe the correlation between the NC 3-D orientation based on the crystal symmetry and (ii) angular-dependent Zeeman splitting.

6.4.4 Zero Field Splitting

During our investigation of external magneto-optical effects, we observed zero field effects where the degeneracy in the spin states is lifted as shown in figure 6.4. Although this was a surprise, previous magnetic field experiments have also reported data suggesting NC interactions with paramagnetic centers or uncompensated spins on the NC surface. These behaviors include non-single exponential excited state decay kinetics[20] and temperature dependence of the g-factor[7]. The effects of an intrinsic magnetic impurity here are quite convincing. First, the Zeeman split spectra have doublet peaks that remain regardless of spectral diffusing peak positions. Second, the circular polarization is consistent with emission from spin states. Finally, the peak separation is still affected by an externally applied magnetic field. A closer examination of polarization data in figure 6.3 also shows the presence of a non-zero polarization anisotropy at zero field.

We now speculate on the possible explanation for observing this zero-field Zeeman splitting in CdSe/ZnS core-shell NCs. Although zero field splitting (ZFS) is commonly observed in quantum well heterostructures, the origin of the ZFS in CdSe/ZnS NCs is not the Rashba effect. First, an interfacial electric field is necessary to produce a spin splitting term in the Hamiltonian and second, this should occur for all NCs. Another possible source of the zero-field splitting is the presence of unpaired electrons in the NC. We have observed a variety of single NC optical dynamics that originate from a charged or charge decorated NC. These charges may also cause a paramagnetic interaction that splits the NC electronic level degeneracy. Determining whether the zero-field splitting is

dynamic and correlating the changes to the blinking-charging behavior can further corroborate this model.

6.5 Conclusion and Future Studies

We have observed the molecular Zeeman effect in single CdSe/ZnS NCs, with g-factor values consistent with theory and previous ensemble averaged experiments. The advantages of single molecule spectroscopy offer direct analysis of the Zeeman effect in correlation to the NC 3-D orientation and have revealed an intrinsic magnetic interaction leading to Zeeman splitting in the absence of an external magnetic field. In future work, the nature of this intrinsic magnetic interaction needs further investigation possibly assisted with ultra-fast measurements of the excited state lifetime. The areas of diluted magnetic semiconductors may be of keen interest for single NC study to understand effects of spin coherence. The pursuit to understand the dynamic nature of the magnetic interaction is severely limited by the light collection efficiency of the magneto-cryostat. One possible scenario is to couple the surface-enhanced fluorescence system into the magnet system. Although polarization information will be lost due to the strong gold-NC coupling, the five-fold increase in light output may help to attain faster time resolution and greater signal-to-noise in the spectral analysis.

6.6 References

1. S.A. Wolf, D.D. Awschalom, R.A. Buhrman, J.M. Daughton, S. von Molnar, M.L. Roukes, A.Y. Chtchelkanova, and D.M. Treger, Science, 2001. **294**(5546): p. 1488.
2. A.L. Efros, E.I. Rashba, and M. Rosen, Physical Review Letters, 2001. **8720**(20): p. art. no.

3. S.W. Brown, T.A. Kennedy, D. Gammon, and E.S. Snow, Physical Review B, 1996. **54**(24): p. 17339.
4. A. Zrenner, M. Markmann, A. Paassen, A.L. Efros, M. Bichler, W. Wegscheider, G. Bohm, and G. Abstreiter, Physica B, 1998. **258**: p. 300.
5. D. Gammon, A.L. Efros, T.A. Kennedy, M. Rosen, D.S. Katzer, D. Park, S.W. Brown, V.L. Korenev, and I.A. Merkulov, Physical Review Letters, 2001. **86**(22): p. 5176.
6. M. Kuno, M. Nirmal, G. Bawendi, A. Efros, and M. Rosen, Journal of Chemical Physics, 1998. **108**(10): p. 4242.
7. E. Johnston-Halperin, D.D. Awschalom, S.A. Crooker, A.L. Efros, M. Rosen, X. Peng, and A.P. Alivisatos, Physical Review B, 2001. **6320**(20): p. art. no.
8. J.A. Gupta, D.D. Awschalom, X. Peng, and A.P. Alivisatos, Physical Review B-Condensed Matter, 1999. **59**(16): p. R10421.
9. D.J. Norris, N. Yao, F.T. Charnock, and T.A. Kennedy, Nano Letters, 2001. **1**(1): p. 3.
10. C.B. Murray, D.J. Norris, and M.G. Bawendi, Journal of the American Chemical Society, 1993. **115**(19): p. 8706.
11. M.A. Hines and P. Guyot-Sionnest, Journal of Physical Chemistry, 1996. **100**(2): p. 468.
12. B.O. Dabbousi, J. RodriguezViejo, F.V. Mikulec, J.R. Heine, H. Mattoussi, R. Ober, K.F. Jensen, and M.G. Bawendi, Journal of Physical Chemistry B, 1997. **101**(46): p. 9463.
13. S.A. Empedocles, D.J. Norris, and M.G. Bawendi, Physical Review Letters, 1996. **77**(18): p. 3873.
14. M. Nirmal, B.O. Dabbousi, M.G. Bawendi, J.J. Macklin, J.K. Trautman, T.D. Harris, and L.E. Brus, Nature, 1996. **383**(6603): p. 802.
15. The error in the anisotropy values can be rather large because of the strong dependence on background subtraction. The anisotropy value presented here should be gauged on the Gaussian fitting for the 50 NCs.
16. I. Chung, K.T. Shimizu, and M.G. Bawendi, Submitted, 2002.
17. A.L. Efros, M. Rosen, M. Kuno, M. Nirmal, D.J. Norris, and M. Bawendi, Physical Review B-Condensed Matter, 1996. **54**(7): p. 4843.
18. A.L. Efros, Physical Review B-Condensed Matter, 1992. **46**(12): p. 7448.
19. S.A. Empedocles, R. Neuhauser, and M.G. Bawendi, Nature, 1999. **399**(6732): p. 126.
20. M. Nirmal, Thesis, Massachusetts Institute of Technlogy, 1996.

List of Publications

1. K. T. Shimizu, M. K. Kuno, and M. G. Bawendi, "Zeeman Spectroscopy of Single CdSe Nanocrystal Quantum Dots", (in preparation).

2. K. T. Shimizu, WK Woo, B. R. Fisher, H.J. Eisler, and M.G. Bawendi, "Surface-Enhanced Emission from Single Semiconductor Nanocrystals", Physical Review Letters (in press, 2002).

3. I. Chung, K. T. Shimizu, and M. G. Bawendi, "Room Temperature Measurements of the 3-D Orientation of Single CdSe Quantum Dots using Polarization Microscopy", (submitted, 2002).

4. WK Woo, K. T. Shimizu, R. G. Neuhauser, M. Jarosz, C. A. Leatherdale, and M.G. Bawendi, "Reversible Charging of CdSe Nanocrystals in a Simple Solid-State Device", Advanced Materials (in press, 2002).

5. K. T. Shimizu, R. G. Neuhauser, C. A. Leatherdale, S. A. Empedocles, WK Woo, and M. G. Bawendi, "Blinking Statistics in Single Semiconductor Nanocrystal Quantum Dots", Physical Review B, 6320 (20): 5316, 2001.

6. R. G. Neuhauser, K. T. Shimizu, WK Woo, S. A. Empedocles, and M. G. Bawendi, "Correlation between Fluorescence Intermittency and Spectral Diffusion in Single Semiconductor Quantum Dots", Physical Review Letters, 85 (15): 3301, 2000.

7. S. A. Empedocles, R. G. Neuhauser, K. T. Shimizu, and M. G. Bawendi, "Photoluminescence from single semiconductor nanostructures", Advanced Materials, 11 (15): 1243, 1999.

8. K. T. Shimizu, S. A. Empedocles, R. G. Neuhauser, and M. G. Bawendi, "Stark Spectroscopy Investigation of Spectral Diffusion in Single CdSe Quantum Dots", Proceedings of the 194th meeting of the Electrochemical Society (in press).

9. K. Shimizu, B. J. Flinn, P.C. Wong, and K. A. R. Mitchell, "SIMS studies of the effect of H at interfaces formed by oxidized zirconium" Canadian Journal Of Chemistry 76 (12): 1796, 1998.

Acknowledgements

The work in thesis required the assistance of many resources from MIT: the Microfabrication laboratory, the wet synthesis laboratory, the Harrison Spectroscopy laser laboratory (and Bawendi laser lab annex), and MIT e-journals to name a few. However, the most important resources are the people who helped shape and complete this thesis over the last few years.

First and foremost, I would like to thank my thesis advisor, Moungi Bawendi, for providing the encouragement, guidance, and flexibility to pursue my scientific and sometimes non-scientific endeavors. Although we had irregular meeting schedules, I remember that you always conveyed ingenious ideas and insightful explanations in the clearest and most useful manner. For all your patience and advice I am grateful.

I have been fortunate to interact and learn from a number of devoted scientists and devoted friends. Ken, Fred, Steve, and Catherine, you were the foundations for this work with your deity-like knowledge in answering the endless questions and solving laboratory problems with ease. In particular, I owe Kuno-san a large debt for helping me revive the magnet from its slumber. Robert, you simply made work more fun than playing in the sun. Dmitry, you were pivotal in adding color to the laboratory every morning with your unique insights into life. Wing, I cannot thank you enough for spending all those hours joking and keeping me on the steady path. Vikram, the other brother in the Eliem fraternity, I thank you for your wit and sarcasm not only in critiquing my work, but also in supporting my goals. To Hans, Sungjee, Nathan, Inhee, Mirna, Brent, Joe, Dirk, Jean-Michel, Yinthai, John S., Brian, and John Z., I feel privileged to have had the opportunity to work with all of you.

Inhee, Mirna, Brent, and Jean-Michel, it was always fun and adventurous to walk into the laser lab and see the myriad of experiments that we were trying to do all on the same day! I thank you for bearing with me and helping me on many occasions. From my experience with you thus far, I know all of you will have exceptional success in the laser (and wet) lab and beyond.

Joe, I enjoyed our afternoon and post-midnight conversations about science and life as scientists. Dirk, I am indebted to you for helping me with my publication and thesis preparations.

To the MIT Zoo tenants of 1997: Chris, Aimee, Michelle, Vik, and Younjoon, I thank you guys for a great start to the Ph. D. experience. The stories of our bonding and breakdowns will be cherished for many years to come.

There was one very important person that set my course to MIT back in 1995. I am forever indebted to my undergraduate advisor, Dr. Phillip Kash, for opening my eyes to life's possibilities and to the means for achieving those goals.

Finally, I would like to thank my family and friends back in Vancouver. I am grateful to my parents, who have given me all the love and support to do whatever I wanted and to my brother and sister for the encouragement and brotherly/sisterly love from thousands of miles away. My friends, Rey, Stephanie, and Henry, know that they are also part of my success. Without their friendship and constant support I know that this journey would have been nearly impossible.